

**AFRL-AFOSR-UK-TR-2011-0036**



## **Broadband Epsilon-Near-Zero (ENZ) and Mu-Near-Zero (MNZ) Active Metamaterial**

**Silvio Hrabar  
Igor Krois  
Ivan Bonic  
Aleksandar Kiricenko  
Eduardo Ugarte Munoz**

**University of Zagreb  
Faculty of Electrical Engineering and Computing  
Department of Wireless Communications  
Unska 3  
Zagreb, Croatia HR 10 000**

**EOARD GRANT 10-3030**

**August 2011**

**Final Report for 24 August 2010 to 24 August 2011**

**Distribution Statement A: Approved for public release distribution is unlimited.**

**Air Force Research Laboratory  
Air Force Office of Scientific Research  
European Office of Aerospace Research and Development  
Unit 4515 Box 14, APO AE 09421**

<b>REPORT DOCUMENTATION PAGE</b>				Form Approved OMB No. 0704-0188	
<small>Public reporting burden for this collection of information is estimated to average 1 hour per response, including the time for reviewing instructions, searching existing data sources, gathering and maintaining the data needed, and completing and reviewing the collection of information. Send comments regarding this burden estimate or any other aspect of this collection of information, including suggestions for reducing the burden, to Department of Defense, Washington Headquarters Services, Directorate for Information Operations and Reports (0704-0188), 1215 Jefferson Davis Highway, Suite 1204, Arlington, VA 22202-4302. Respondents should be aware that notwithstanding any other provision of law, no person shall be subject to any penalty for failing to comply with a collection of information if it does not display a currently valid OMB control number.</small> <b>PLEASE DO NOT RETURN YOUR FORM TO THE ABOVE ADDRESS.</b>					
<b>1. REPORT DATE (DD-MM-YYYY)</b> 26-08-2011		<b>2. REPORT TYPE</b> Final Report		<b>3. DATES COVERED (From – To)</b> 24 August 2010 – 24 August 2011	
<b>4. TITLE AND SUBTITLE</b>  <b>Broadband Epsilon-Near-Zero (ENZ) and Mu-Near-Zero (MNZ) Active Metamaterial</b>				<b>5a. CONTRACT NUMBER</b> FA8655-10-1-3030	
				<b>5b. GRANT NUMBER</b> Grant 10-3030	
				<b>5c. PROGRAM ELEMENT NUMBER</b>	
<b>6. AUTHOR(S)</b>  Silvio Hrabar Igor Krois Ivan Bonic Aleksandar Kiricenko Eduardo Ugarte Munoz				<b>5d. PROJECT NUMBER</b>	
				<b>5d. TASK NUMBER</b>	
				<b>5e. WORK UNIT NUMBER</b>	
<b>7. PERFORMING ORGANIZATION NAME(S) AND ADDRESS(ES)</b> University of Zagreb Faculty of Electrical Engineering and Computing Department of Wireless Communications Unska 3 Zagreb, Croatia HR 10 000				<b>8. PERFORMING ORGANIZATION REPORT NUMBER</b>  N/A	
<b>9. SPONSORING/MONITORING AGENCY NAME(S) AND ADDRESS(ES)</b>  EOARD Unit 4515 BOX 14 APO AE 09421				<b>10. SPONSOR/MONITOR'S ACRONYM(S)</b> AFRL/AFOSR/RSW (EOARD)	
				<b>11. SPONSOR/MONITOR'S REPORT NUMBER(S)</b>  <b>AFRL-AFOSR-UK-TR-2011-0036</b>	
<b>12. DISTRIBUTION/AVAILABILITY STATEMENT</b>  Approved for public release; distribution is unlimited. (approval given by local Public Affairs Office)					
<b>13. SUPPLEMENTARY NOTES</b>					
<b>14. ABSTRACT</b> This study reports 12-month research effort undertaken to understand, and eventually overcome, one of the most serious drawbacks of all passive metamaterials: <i>the inherent narrowband operation</i> . We found that this narrowband operation is limited by basic physics (by the energy-dispersion constraints) and not by imperfections of available technology. However, we also found possible to go around this drawback by the incorporation of <i>active non-Foster elements</i> in the metamaterial structure. It is known that, under some circumstances, all active elements (including the non-Foster elements) may cause stability problems. We thoroughly analyzed this issue and found that commonly used frequency-domain methods of stability prediction are not applicable in the case of non-Foster elements. Therefore, we developed a simple circuit-theory approach of accessing stability of non-Foster elements in time domain. Using developed method, we have proved that is indeed possible to build stable ENZ and MNZ metamaterials with multi-octave bandwidth and almost flat dispersion curve. This theoretical and numerical investigation has been complemented with the development of experimental proof-of-concept prototypes, in RF (up to 100 MHz) and lower microwave range (up to 2 GHz). Developed prototypes comprise: the negative capacitors, the unit cells of active 2D ENZ metamaterials, and the active ENZ transmission line. All the prototypes were 'hand-crafted' using standard FET and OPAMP SMD components. The measurements revealed multi-octave bandwidth, which is significantly better than the bandwidth of all passive metamaterials reported so far. All achieved results clearly show that the novel proposed concept of non-Fosterelement-based active metamaterial is correct. Finally, we have shown that this can enable ultra-broadband operation of the previously reported narrowband plasmonic and transformation-electromagnetic cloaks.					
<b>15. SUBJECT TERMS</b>  EOARD, metamaterials					
<b>16. SECURITY CLASSIFICATION OF:</b>			<b>17. LIMITATION OF ABSTRACT</b>  SAR	<b>18. NUMBER OF PAGES</b>  121	<b>19a. NAME OF RESPONSIBLE PERSON</b> SCOTT DUDLEY, Lt Col, USAF
<b>a. REPORT</b> UNCLAS	<b>b. ABSTRACT</b> UNCLAS	<b>c. THIS PAGE</b> UNCLAS			<b>19b. TELEPHONE NUMBER</b> (Include area code) +44 (0)1895 616162

FINAL REPORT FOR CONTRACT **FA8655-10-1-3030**

# **Broadband Epsilon-Near-Zero (ENZ) and Mu-Near-Zero (MNZ) Active Metamaterial**

by

**Silvio Hrabar  
Igor Krois  
Ivan Bonic  
Aleksandar Kirichenko  
Eduardo Ugarte Muñoz**

SUBMITTED BY: Prof. Silvio Hrabar  
Faculty of Electrical Engineering and Computing  
University of Zagreb  
Unska 3  
Zagreb, HR-10000, Croatia

23 August 2011

<b>Grant/Cooperative Agreement Award</b>				
1. AWARD NO. FA8655-10-1-3030		2. EFFECTIVE DATE 24 AUG 2010		3. PURCHASE REQUEST NO. See Block 16
4. CFDA NO. 12.800		PAGE OF 1 3		
5. ISSUE BY EOARD EUROPEAN OFFICE OF AEROSPACE RESEARCH AND DEVELOPMENT UNIT 4515 BOX 14 APO AE 09421 USA WENDY HARRISON +44(0)18956161 wendy.harrison@london.af.mil		6. AWARDED TO CAGE CODE A01MB UNIVERSITY OF ZAGREB FACULTY OF ELECTRICAL ENGINEERING UNSKA 3 ZAGREB HR-10000 CROATIA		7. AUTHORITY 10 U.S.C. 2358
8. PERIOD OF PERFORMANCE 24 AUG 10 TO 23 AUG 11				
9. SCOPE / AGREEMENT TERMS Assistance is for Research entitled, "Broadband Epsilon-Near-Zero (ENZ) and Mu-Near-Zero (MNZ) Active Metamaterial." The "Air Force Research Laboratory Grants Terms and Conditions Sep 2009 - Awards to International Educational Institutions and Non-Profit Organizations" and the Recipient's Technical Proposal are incorporated by reference. Awardee signature is not required on this agreement; however, the recipient agrees to the conditions specified in this award unless notice of disagreement is furnished to the awarding officer within 15 days after the signature date. In case of disagreement, the recipient shall not incur any costs until the disagreement is resolved.				
10. RECIPIENT PRINCIPAL INVESTIGATOR Dr. Silvio Hrabar		11. OTHER SPONSORING AGENCY(S) AFRL/RYHF		
12. ADMINISTRATIVE OFFICE CODE FA8655 EUROPEAN OFFICE OF AEROSPACE RESEARCH AND DEVELOPMENT 86 BLENHEIM CRESCENT RUISLIP, MIDDLESEX HA4 7HB UNITED KINGDOM		13. PAYING OFFICE CODE: F78900 DFAS-LI 27 ARKANSAS ROAD LIMESTONE MAINE 04751-6216 USA		14. STAFF JUDGE ADVOCATE OFFICE AFOSR/JA (703) 696-9500 875 NORTH RANDOLPH STREET SUITE 325, ROOM 3112 ARLINGTON, VIRGINIA 22203 USA
15. GOVT PROGRAM MANAGER (Name, Org, Tel, Email) Scott Dudley, Lt Col, USAF, +44 (0) 189 561 6162, Scott.Dudley@london.af.mil				
16. ALLOCATED FUNDING: The following funds with associated Accounting Classification reference number(s) (ACRNs) are allotted to this agreement:				
<u>ACRN</u>	<u>FUND CITATION(s)</u>	<u>AMOUNT</u>		
SEE CONTINUATION				
SPECIAL INSTRUCTIONS: PAYMENT WILL BE MADE BY ELECTRONIC FUNDS TRANSFER.				
PAYING OFFICE INSTRUCTIONS: USE EARLIEST CITED FUNDS FIRST.				
PAYMENT SCHEDULE (if applicable): SEE FOLLOWING PAGE(S) FOR REPORT AND PAYMENT SCHEDULE AND INSTRUCTIONS				
17. TOTAL FUNDS OBLIGATED		Government Share		Recipient Share
		\$30,000.00		\$0.00
19. AMOUNT OF AWARD		Government Share		Total
		\$30,000.00		\$30,000.00
20. OPTIONS N/A		Government Share		Total
21. PERIOD				
22. SIGNATURE		23. SIGNATURE		
		Wendy Harrison		
24. NAME AND TITLE		25. DATE SIGNED		26. NAME AND TITLE
				WENDY HARRISON
				27. DATE SIGNED
				24 Aug 10
		GRANTS OFFICER		

Figure 1-1 A concept of volumetric metamaterial .....	8
Figure 1-2 Classification of passive metamaterials .....	9
Figure 1-3 Dispersion behavior of different metamaterials, Upper Behavior of fictitious lossless and dispersionless metamaterial, Solid –ENZ or MNZ metamaterial, Dashed - ENG or MNG metamaterial, Middle- Behavior of realistic metamaterial with Lorentz dispersion, Lower-Behavior of realistic metamaterial with Drude dispersion Solid – real part, Dashed –imaginary part.....	10
Figure 3-1 EM wave propagation inside the cloak .....	17
Figure 3-2 Calculated phase shift of materials with different dispersion .....	18
Figure 3-3 Resonant process in continuous material (the graphs have been taken from <a href="http://www.walter-fendt.de/ph14e/resonance.htm">http://www.walter-fendt.de/ph14e/resonance.htm</a> ) .....	21
Figure 3-4 LC circuit model of an inclusion in passive metamaterial, Left - an electric inclusion, Middle - an electric inclusion with energy redistribution from electric into the magnetic field, Right – an equivalent circuit.....	22
Figure 3-5 Schematic explanation of resonant energy redistribution in passive metamaterial	24
Figure 3-6 Reactance (susceptance) of idealized lossless NZ (NG) inclusions, Left - series LC circuit, Right - parallel LC circuit .....	25
Figure 3-7 Reactance (susceptance) of coupled lossless LC inclusions , Left - series inductive coupling, Right - series capacitive coupling.....	26
Figure 3-8 Impedance of a simple parallel LC circuit with loss (a simple ENZ or ENG inclusion).Solid line – imaginary part, Dashed line – real part. ....	27
Figure 3-9 Transmission-line equivalent circuit of passive metamaterial .....	28
Figure 3-10 Wire medium, Left - physical construction, Middle - Dispersion characteristic, Right - Transmission-line equivalent circuit .....	29
Figure 3-11 Measured effective permittivity of wire medium [2] .....	30
Figure 3-12 Metamaterials based on resonant inclusions, Upper - inductively loaded dipole (loop-wire, CSRR), Lower - Capacitively loaded loop (SRR).....	31
Figure 3-13 Polarizability of a small electric inclusion, Upper – loading element is an inductor, Lower - loading element is a capacitor .....	33
Figure 3-14 Transmission line equivalent circuit of metamaterial with array of inductively loaded short dipoles .....	33
Figure 3-15 Induced magnetic moment of a small magnetic inclusion, Upper – loading element is a capacitor, Lower - loading element is an inductor, .....	35
Figure 3-16 Transmission-line equivalent circuit of MNG (MNZ) metamaterial based on an array of capacitively loaded loops.....	36
Figure 3-17 Extracted effective relative permeability of the metamaterial based on SRR inclusions [2], Solid – real part, Dashed – imaginary part .....	36
Figure 3-18 DNG Transmission-line-based metamaterial .....	37
Figure 3-19 Equivalent circuits of different passive 1D TL-based metamaterials, Left – MNG (or MNZ), Middle - ENG (or ENZ), Right- DNG (or MENZ) .....	38
Figure 4-1 Left - Transmission-line model of 1D passive ENG (or ENZ) metamaterial, Right Proposed active ENZ metamaterial .....	43
Figure 4-2 Reactance of positive (solid line) and negative (dashed line) reactive elements ...	44
Figure 4-3 An example of operating principle of negative non-Foster impedance .....	45
Figure 4-4 Comparison between LC circuit and $CC_n$ circuit .....	45
Figure 4-5 Left - Transmission-line model of 1D passive MNZ metamaterial, Right - Proposed active MNZ metamaterial .....	48
Figure 4-6 Broadband active non-Foster MENZ metamaterial .....	50
Figure 4-7 Examples of proposed 2D anisotropic active metamaterials, Upper - ENZ, Middle –MNZ, Lower - MENZ .....	51

Figure 4-9 Charging of positive/negative capacitor. Left: $C>0$ , Right: $C<0$ .....	53
Figure 4-8 Charging of positive/negative capacitor.....	53
Figure 4-10 Discharging of positive/negative capacitor. Upper: $C>0$ , Lower: $C<0$ .....	54
Figure 4-11 Generalized LC tank circuit .....	55
Figure 4-12 Signal waveforms in a stable LC tank circuit, blue – voltage, red - current .....	56
Figure 4-13 Instantaneous power on the elements of a stable LC tank circuit, Blue - power on the inductor, Red - power on the capacitor.....	57
Figure 4-14 Instantaneous stored energy on the elements of a stable LC tank circuit, Blue – energy on the inductor, Red – energy on the capacitor .....	57
Figure 4-15 Positive/negative LC tank circuit driven by a voltage source .....	58
Figure 4-16 Loci of the poles of the driven positive/negative LC circuit for $L>0$ , $R>0$ .....	59
Figure 4-17 Loci of the poles of the driven positive/negative LC circuit for $L<0$ , $R<0$ .....	60
Figure 4-18 Loci of the poles of the driven positive/negative LC circuit for $L<0$ , $R<0$ .....	60
Figure 4-19 Parallel $CC_n$ circuit.....	61
Figure 4-20 Voltages and Energy in a $C$ - $C_n$ circuit .....	63
Figure 4-21 Stability regions for the $CC_n$ circuit with no driving source .....	64
Figure 4-22 Parallel $CC_n$ circuit driven by an external source .....	64
Figure 4-23 Loci of the poles of the driven $CC_n$ circuit for $C_1>0$ , $R>0$ .....	65
Figure 4-24 Voltage, currents, power and energy in the $CC_n$ circuit with $C_2>0$ .....	66
Figure 4-25 Voltage, currents, instantaneous power and energy in $CC_n$ circuit with $C_2<0$ ....	67
Figure 4-26 Series/parallel $RC_n/C$ circuit.....	68
Figure 4-27 Voltages in series/parallel $RC_n/C$ circuit with $C_2>0$ .....	69
Figure 4-28 Voltages in series/parallel $RC_n/C$ circuit with $C_2>0$ .....	70
Figure 4-29 Instantaneous power in series/parallel $RC_n/C$ circuit with $C_2>0$ .....	70
Figure 4-30 Instantaneous energy in series/parallel $RC_n/C$ circuit with $C_2>0$ .....	71
Figure 4-31 Voltages in series/parallel $RC_n/C$ circuit with $C_2<0$ and $C_2< C_1 $ .....	71
Figure 4-32 Currents in series/parallel $RC_n/C$ circuit with $C_2<0$ and $C_2< C_1 $ .....	72
Figure 4-33 Instantaneous power in series/parallel $RC_n/C$ circuit with $C_2<0$ and $C_2< C_1 $ ....	72
Figure 4-34 Instantaneous energy in series/parallel $RC_n/C$ circuit with $C_2<0$ and $C_2< C_1 $ ..	73
Figure 4-35 Voltages in series/parallel $RC_n/C$ circuit with $C_2<0$ and $C_2> C_1 $ .....	73
Figure 4-36 Stability regions for series/parallel $RC_n/C$ circuit with no driving source .....	74
Figure 4-37 Parallel $RCC_n$ circuit with no driving source .....	75
Figure 4-38 Voltages and currents in parallel $RCC_n$ circuit with no driving source .....	77
Figure 5-1 Basic definition of NIC as a two-port network .....	80
Figure 5-2 General NIC modeled with h-parameters.....	80
Figure 5-3 h-parameter model of an ideal INIC.....	81
Figure 5-4 h-parameter model of an ideal VNIC .....	82
Figure 5-5 Transformation of basic INIC into with single current source.....	82
Figure 5-6 Transformation of basic VNIC into VNIC with single voltage source .....	83
Figure 5-7 Two possible equivalent circuits of VNIC with single voltage source .....	83
Figure 5-8 Different designs of NIC circuits with two BJTs (taken from [41]) .....	85
Figure 5-9 Operation of Linvill (left) and Yanagisawa (right) NIC circuits .....	86
Figure 5-10 Meunier's NIC.....	88
Figure 5-11 Floating NIC with two FET's.....	89
Figure 5-12 OPAMP-based NIC, type A .....	90
Figure 5-13 OPAMP-based NIC, type B .....	91
Figure 5-14 Negative capacitor circuit based on A1 type of NIC.....	92
Figure 5-15 Negative capacitor circuit based on A2 type of NIC.....	93
Figure 5-16 Negative capacitor circuit based on B1 type of NIC.....	93
Figure 5-17 Negative capacitor circuit based on B2 type of NIC.....	93

Figure 5-18 Input resistance of negative capacitor OPAMP-based NICs, $R_1$ (green) -type A1, $R_2$ (red)-type A2, $R_3$ (blue)-type B1, $R_4$ (black)-type B2,.....	94
Figure 5-19 Input capacitance of negative capacitor OPAMP-based NICs, $C_1$ (black)-type A1, $C_2$ (blue)-type A2, $C_3$ (red) -type B1, $C_4$ (green) -type B2, .....	94
Figure 5-20 Experimental negative capacitors, Upper - basic circuit, Middle – the prototype I, Lower – the prototype II.....	97
Figure 5-21 Photos of experimental negative capacitors, Left – the prototype I, Right – the prototype II .....	98
Figure 5-22 Measured input impedance of experimental negative capacitors (solid - the prototype I, dashed- the prototype II).....	99
Figure 5-23 2D unit cell of an active ENZ metamaterial, Left – equivalent circuit, Right - A sketch of realized unit cell.....	99
Figure 5-24 Measured relative permittivity of unit cells (solid –real part, dashed – imaginary part).....	100
Figure 5-25 A sketch of ADS <sup>TM</sup> model of active cloak .....	100
Figure 5-26 Computed normalized voltage distributions of all unit cell nodes in the ADS <sup>TM</sup> model of a bare target (left) and a target with an active cover (right).....	101
Figure 5-27 Calculated blockage coefficient of a bare dielectric target (circles, red), passive cloak (triangles, blue) and an active cloak (squares, magenta) .....	102
Figure 5-28 Schematic diagram of developed OP-amp based negative capacitor.....	103
Figure 5-29 Photo of developed OPAMP-based negative capacitor .....	103
Figure 5-30 Comparison between simulated and measured input resistance ( $\Omega$ ), Red – simulations, Blue - measurements .....	104
Figure 5-31 Comparison between simulated and measured input capacitance (F) , Red – simulations, Blue - measurements .....	105
Figure 5-32 Experimental active RF 1D ENZ metamaterial, Upper –A sketch of transmission line loaded with three negative capacitors the, Lower –practical realization ( $l=1m$ , $d=33$ cm, $h=3$ mm, $w=25$ mm) .....	106
Figure 5-33 Measured argument of transmission coefficient $S_{2,1}$ (degrees). Solid (blue) – TL with NICs, Dashed (red) – TL without NICs, Dotted (green) –the light line.....	106
Figure 5-34 Extracted effective permittivity of active 1D ENZ metamaterial, Solid–real part, Dashed – imaginary part.....	108
Figure 5-35 Extracted velocities of active 1D ENZ MTM , Dashed - phase velocity Solid – group velocity.....	108
Figure 5-36 Results of time-domain measurements of superluminal effects in active broadband 1D ENZ transmission line .....	109
Table 3-1 Comparison of passive metamaterials .....	39
Table 4-1 Stability criteria for generalized positive/negative LC tank circuit.....	56
Table 4-2 Stability criteria for driven positive/negative LC tank circuit.....	61
Table 4-3 Stability criteria for CC <sub>n</sub> circuit with no driving source .....	64
Table 4-4 Stability criteria for CC <sub>n</sub> circuit driven by an external source .....	67
Table 4-5 Stability criteria for series/parallel RC <sub>n</sub> /C circuit with no driving source.....	74
Table 4-6 Stability criteria for parallel RCC <sub>n</sub> circuit with no driving source .....	78
Table 5-1 Comparison of different designs of NIC with two BJT.....	86
Table 5-2 Comparison of analyzed technologies of NIC fabrication .....	95

# TABLE OF CONTENTS

<b>CHAPTER 1 INTRODUCTION .....</b>	<b>7</b>
<b>CHAPTER 2 PROJECT OBJECTIVE AND REALIZED OUTCOMES.....</b>	<b>13</b>
<b>CHAPTER 3 BANDWIDTH LIMITATIONS OF PASSIVE MATERIALS (OR METAMATERIALS). 16</b>	
3.1. IMPORTANCE OF THE DISPERSION ISSUE IN METAMATERIALS .....	17
3.2. ENERGY-DISPERSION CONSTRAINTS .....	19
3.2.1 <i>Basic issue of resonant energy redistribution</i> .....	19
3.2.2 <i>Mechanical oscillator model of resonant energy redistribution in continuous ENZ or ENG material</i> .....	20
3.2.3 <i>LC circuit model of resonant energy redistribution in ENZ or ENG metamaterial</i> .....	21
3.3. CIRCUIT-THEORY PROPERTIES OF PASSIVE METAMATERIALS .....	24
3.3.1 <i>Foster reactance theorem</i> .....	24
3.3.2 <i>Reactance (susceptance) curves of typical metamaterial inclusions</i> .....	25
3.3.3 <i>Influence of finite losses</i> .....	26
3.4. DISPERSION AND BANDWIDTH OF TYPICAL PASSIVE METAMATERIALS .....	28
3.4.1 <i>Wire medium</i> .....	28
3.4.2 <i>Metamaterials based on resonant inclusions (loop-wire, SRR, CSRR)</i> .....	30
3.4.3 <i>Transmission-line-based metamaterials</i> .....	36
3.5. SUMMARY .....	39
<b>CHAPTER 4 ACTIVE NON-FOSTER METAMATERIAL - THEORETICAL INVESTIGATION .....</b>	<b>40</b>
4.1 PREVIOUS WORK .....	41
4.2 A NOVEL CONCEPT OF ULTRA-BROADBAND ENZ OR MNZ ACTIVE METAMATERIAL .....	42
4.2.1 <i>Inclusion of <math>CC_{neg}</math> circuit into transmission line – Broadband active 1D ENZ metamaterial</i> .....	43
4.2.2 <i>Inclusion of <math>LL_{neg}</math> circuit into transmission line – Broadband active 1D MNZ metamaterial</i> .....	48
4.2.3 <i>Extension to Broadband active 2D metamaterial</i> .....	50
4.3 STABILITY ANALYSIS OF NON-FOSTER NEGATIVE REACTANCE ELEMENTS .....	52
4.3.1 <i>Introduction</i> .....	52
4.3.2 <i>Charging/discharging of a positive/negative capacitor and occurrence of the instabilities</i> .....	52
4.3.3 <i>Positive/negative parallel LC tanks – natural response</i> .....	54
4.3.4 <i>Positive/negative parallel LC tank circuit driven by an external source</i> .....	58
4.3.5 <i>Parallel <math>CC_n</math> circuit – natural response</i> .....	61
4.3.6 <i>Parallel <math>CC_n</math> circuit driven by an external source</i> .....	64
4.3.7 <i>Series/parallel <math>RC_n/C</math> circuit – natural response</i> .....	67
4.3.8 <i>Parallel <math>RCC_n</math> circuit – natural response</i> .....	74
4.4. SUMMARY .....	78
<b>CHAPTER 5 TECHNOLOGICAL ISSUES AND EXPERIMENTAL INVESTIGATION.....</b>	<b>79</b>
5.1. NEGATIVE IMPEDANCE CONVERTER (NIC).....	80
5.1.1 <i>Current inverter (INIC)</i> .....	80
5.1.2 <i>Voltage inverter (VNIC)</i> .....	81
5.1.3 <i>Reducing number of dependent sources in NIC circuits</i> .....	82
5.1.4 <i>Stability of NIC circuit</i> .....	83
5.2. REVIEW OF SOME COMMON NIC DESIGNS .....	84
5.2.1 <i>BJT-based circuits</i> .....	84
5.2.2 <i>FET-based circuits</i> .....	87
5.2.3 <i>OPAMP-based circuits</i> .....	90
5.2.4 <i>Comparison of analyzed technologies of NIC fabrication</i> .....	95
5.3. EXPERIMENTAL RF (50-100 MHz, 1-2 GHz) 2D UNIT CELLS OF ACTIVE ENZ MTM.....	95
5.3.1 <i>Development and testing of FET-based negative capacitors</i> .....	96
5.3.2 <i>Development and testing of 2D unit cell of ENZ metamaterial</i> .....	99
5.3.3 <i>Demonstration of possible application in broadband plasmonic cloaking</i> .....	100
5.4. EXPERIMENTAL RF (2MHz-40MHz) SUPERLUMINAL 1D ACTIVE ENZ MTM .....	102
5.4.1 <i>Development and testing of OPAMP-based negative capacitors</i> .....	102
5.4.2 <i>Development and testing of ultra-broadband ENZ RF transmission line (1D MTM)</i> .....	105
5.4.3 <i>Demonstration of broadband superluminal effects</i> .....	108
5.5. SUMMARY .....	110
<b>CHAPTER 6 CONCLUSIONS AND FUTURE WORK.....</b>	<b>111</b>
<b>CHAPTER 7 BIBLIOGRAPHY.....</b>	<b>114</b>



Chapter 1 INTRODUCTION

## Introduction

Metamaterials (MTM) [1-4] are artificial structures, engineered to provide unusual electromagnetic properties not found in naturally occurring materials. A basic design (Figure 1-1) comprises an array of electrically small electromagnetic scatterers (the inclusions) embedded into a dielectric host material. The inclusions are located at mutual distance that is a small fraction of the wavelength.

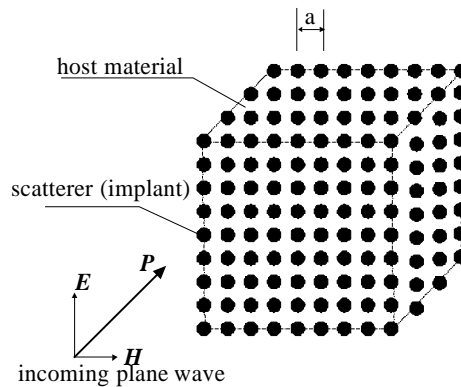


**Figure 1-1** A concept of volumetric metamaterial

If electromagnetic wave impinges on this structure, all the local fields scattered from particular inclusions will be summed up to the incident field resulting the net field distribution. Thus, the original field distribution will be changed due to ‘reacting’ field caused by local scattering from the inclusions. This process is, in principle, very similar to mechanism of electric or magnetic polarization in ordinary continuous materials.

Since the phase shift across volume occupied by a single particle (a unit cell) is small, the diffraction effects are negligible. Thus, the structure behaves as it would behave *some hypothetical continuous material*. This material would have new (homogenized) values of constitutive parameters (permittivity  $\epsilon$  and permeability  $\mu$ ), *generally deferent* from the parameters of the host material and the inclusions. The equivalent permittivity and permeability are primarily dependent on the geometrical properties of an inclusion shape and mutual distance between the inclusions (lattice constant). Thus, it is possible to tailor the electromagnetic response of the inclusions almost arbitrarily (by appropriate design) and, therefore to achieve exotic values of equivalent permittivity and permeability that cannot be found in nature [1-4].

Apart from familiar **Double-Positive** materials (**DPS**), there are also materials with **Single-Negative** (**SNG**) and **Single-Near-Zero** (**SNZ**) behavior (Figure 1-2). This class

comprises **Epsilon-NeGative (ENG)** and **Mu-NeGative (MNG)** materials. Finally, there are also classes of **Double-Negative (DNG)** and **Double-Near-Zero (DNZ)** metamaterials [1-4].

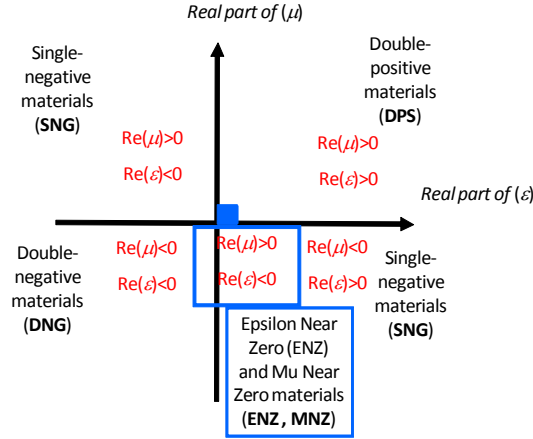


**Figure 1-2** Classification of passive metamaterials

Metamaterials with all these unusual values of constitutive parameters (**SNG**, **DNG**, **SNZ**, **DNZ**) offer many unexpected and counter-intuitive physical phenomena such as backward-wave propagation, negative refraction, and ‘amplification’ of evanescent waves [1-4]. During the past decade, huge research efforts worldwide have been put into possible application of these phenomena for novel devices such as miniaturized antennas and waveguides [5-9], the resolution-free lenses [10,11], and invisibility cloaks [12-14]. Although basic principles have been successfully demonstrated, very few real-world implementations have been reported so far [15].

Actually, there are two main problems that prevent wide use of metamaterials in practical engineering systems: a significant loss (comparing to ordinary dielectrics) and a narrow operating bandwidth (again comparing to ordinary dielectrics) [2,4,4]. It is important to stress that these two drawbacks *are not mutually independent*. They are the consequences of inherent change of the permittivity or permeability with frequency (i.e. *dispersion*). Although this is a very basic issue, it is widely misunderstood and often overlooked in metamaterial community.

Ordinary dielectrics are usually considered as being frequency independent (dispersionless) across the entire RF spectrum starting from DC up to more than 40 GHz. It would be very convenient to have similar behavior in the case of metamaterials (Upper part of Figure 1-3). Unfortunately, the values of constitutive parameters of all SNG, SNZ, DNZ or DNG metamaterials *do change significantly with frequency*. This change is, in general, described by Lorentz dispersion model (Lower part of Figure 1-3).

It is intuitively clear that the Lorentz dispersion curve in lower part of Figure 1-3 should describe some kind of a resonant process that occurs in every **SNG**, **SNZ**, **DNZ** or **DNG** metamaterial. Due to this resonant process, the losses and the operating bandwidth are *inevitably mutually dependent*. This can also be seen from the mathematical description of the Lorentz model:

$$\mu_{eff} (\epsilon_{eff}) = 1 - \frac{\omega_{ser}^2 - \omega_{par}^2}{\omega^2 - \omega_{par}^2 + j\gamma \frac{\omega}{2\pi}}. \quad (1.1)$$

Here,  $\omega$  is the angular frequency of the signal,  $\omega_{ser}$  denotes the angular frequency of the ‘series resonance’, at which, in lossless case  $\mu_{eff} = 0$  (or  $\epsilon_{eff} = 0$ ) (‘plasma frequency’). Symbol  $\omega_{par}$  stands for angular frequency of the ‘parallel resonance’, at which  $\mu_{eff}$  (or  $\epsilon_{eff}$ )

diverges, and  $\gamma$  represents losses. This is a general dispersion model, while some metamaterials obey simplified Lorentz model, in which  $\omega_{par}=0$  (Drude model):

$$\mu_{eff}(\varepsilon_{eff}) = 1 - \frac{\omega_{ser}^2}{\omega^2 + j\gamma \frac{\omega}{2\pi}}. \quad (1.2)$$

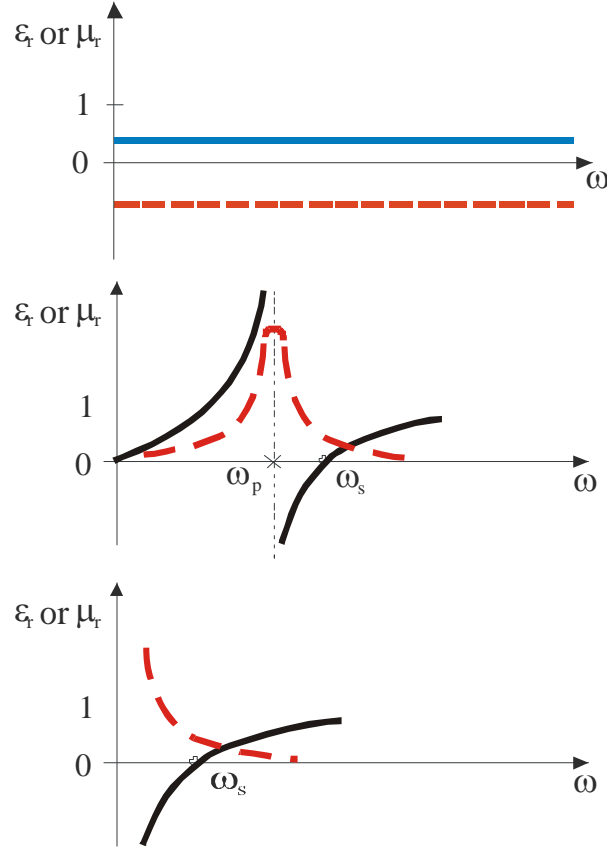


**Figure 1-3** Dispersion behavior of different metamaterials, **Upper** Behavior of fictitious lossless and dispersionless metamaterial, **Solid** –ENZ or MNZ metamaterial, **Dashed** - ENG or MNG metamaterial, **Middle-** Behavior of realistic metamaterial with Lorentz dispersion, **Lower-**Behavior of realistic metamaterial with Drude dispersion **Solid** – real part, **Dashed** –imaginary part

The most successful metamaterial designs nowadays offer maximal losses (at the resonant frequency) smaller than 0.2 dB per unit cell (or per unit layer in the case of stacked metamaterials) [2,3,4]. These losses, although significantly higher than the losses in ordinary materials, are acceptable for many applications.

Unfortunately, the direct comparison of the bandwidths of different metamaterials is not so straightforward. In metamaterial community, the term bandwidth is often used for the frequency band in which *some of the constitutive parameters has required sign* (for instance the bandwidth of negative permittivity or negative permeability). This (loosely constructed and certainly imprecise) definition led to commonly accepted opinion that the transmission-line-based metamaterials are inherently broadband. Indeed, the fractional bandwidth, in which the constitutive parameters are negative (i.e. the backward-wave propagation band) can be as wide as 50 % in the case of the transmission-line-based metamaterials [2,3,4]. On the

contrary, the Split-Ring-Resonator (SRR) or Complementary-Split-Ring-Resonator (CSRR) types of metamaterials have fractional bandwidth of only few percent [2,3,4]. However, one should be aware that a wide band with required negative (or near-zero) parameters *does not guarantee a wideband operation for every application*.

If particular application requires *some fixed values* of the constitutive parameters, one should use a more correct definition that deals with the change of equivalent permittivity or permeability within the required band (*thus, that deals with 'flatness' of the dispersion curve*). In this study, we use a term 'dispersion bandwidth' (DBW). Since all the types of passive metamaterials are highly dispersive comparing to the conventional dielectrics, all of them are inherently narrowband (the middle and lower parts of Figure 1-3). It is interesting that, although pretty obvious, this important issue *is widely overlooked*.

For instance, one may (completely arbitrarily) define the dispersion bandwidth by accepting the change of the constitutive parameters of 15%. In such a case, the bandwidth of typical SRR-based MNG metamaterial would be less than 1% [2].

How much the inherent dispersion actually affects the operational bandwidth of the metamaterial-based device depends on a particular application. A typical application, which clearly points out the metamaterial dispersion as a main obstacle for broadband operation, is electromagnetic cloaking [12-14]. Two generic strategies include cloaking based on plasmonic resonance of the shell that encloses an object [12] and the cloaking based on control of the propagation paths of electromagnetic waves within anisotropic cloak with prescribed spatial variation of constitutive parameters [13]. Both these approaches have already been demonstrated theoretically and experimentally. However, the achieved operational bandwidth (the bandwidth in which the scattered cross-section of the cloaked target is lower than the scattering cross-section of a bare target) is up to 10% for plasmonic cloaking [12] and only 0.24 % for anisotropic cloaking [14]. Clearly, these bandwidths are too narrow for practical applications. The inherent narrowband operation caused by *metamaterial dispersion* is definitely *the most serious problem* for possible future applications of cloaking technology.

Pronounced dispersion of every passive material, relative constitutive parameters of which are either smaller than one ('Near-Zero'(NZ) or 'NeGative' (NG)) is a very basic issue associated with causality-dispersion constraints, i.e. with Foster theorem [16,17]. Use of active materials, for which the basic dispersion constraints do not apply, may overcome this problem.

A new idea of an active metamaterial based on non-Foster reactive elements (a negative capacitor and a negative inductor) was proposed theoretically a few years back [25]. In [25] it was shown that an ensemble of elemental radiators (short dipoles or small loops) loaded with negative capacitors or negative inductors should yield broadband Epsilon-Negative (ENG) or Mu-Negative (MNG) metamaterials with almost flat dispersion curve. This should lead to ultra-broadband operation limited only by availability of non-Foster elements. However, the experimental demonstration of this idea *has not been published yet*. A lack of the experimental results is probably associated with serious stability problems of used non-Foster reactive elements, as it was shown theoretically in [26]. One should also be aware that the stability problems were predicted only for ENG or MNG metamaterials [26]. On the other side, cloaking devices require broadband dispersion-less metamaterials with superluminal phase velocities (thus, the ENZ or MNZ metamaterials). Unfortunately, possible designs and stability issues of these types of active non-Foster metamaterials have not been investigated so far.

Within a different context, in antenna technology, there have been many attempts to use non-Foster elements for broad-band matching of short dipole antennas [31-36]. Although

these studies also pointed stability as a main problem, recent remarkable experimental demonstration [29] showed that this issue can be solved with careful design.

From above discussion it is clear that the narrowband operation is the inherent drawback of all passive metamaterials. Recently, the idea of possible overcoming of this problem by incorporation of active non-Foster elements into metamaterials has been proposed theoretically. However, this approach is in its infant phase and there is a lack of both solid theoretical framework as well as the experimental results. Specifically, the most important open questions are:

1. What is the physical background of inherent resonant behavior of all passive SNG, SNZ, DNZ and DNG metamaterials?
2. What is the physical background of (theoretically predicted) wideband operation of proposed SNG, SNZ, DNZ and DNG active metamaterials based on non-Foster elements?
3. What are the restrictions on proposed wideband operation?
4. What is the cause of inherent instability of active metamaterials based on non-Foster elements and is it possible to build the theoretical framework for stability analysis?
5. What are the possible designs and available technologies of non-Foster circuits that might be used in proposed active metamaterials?
6. Is it possible to develop a practical experimental model (a demonstrator) of active 1D or 2D wideband SNZ (ENZ or MNZ) metamaterial in RF or microwave range at the present state of the art?

The purpose of the project is, therefore, to provide further insight in above issues by analytical, numerical and experimental investigation. Specifically, the project should develop the strategy of active ENZ or MNZ metamaterials design. This design might allow ultra-broadband operation of the previously proposed narrowband devices such as invisibility cloaks [12-14] and reconfigurable antennas [45].

Chapter 2 PROJECT OBJECTIVE AND REALIZED OUTCOMES

## Project objective and realized outcomes

It is known that all passive metamaterials that involve either ‘negative’ (ENG, MNG, DNG) or ‘near-zero’ (ENZ, MNZ, DNZ) constitutive parameters are highly dispersive and, therefore, they suffer from the inherent narrow operating bandwidth. This serious drawback is a consequence of the basic physics (the energy-dispersion constraints) and not a consequence of some technological limitations. On the other side, it has been predicted that the incorporation of active negative capacitors or negative inductors (so called non-Foster elements) into the metamaterial structure could enable broad-band operation.

Therefore, the purpose of this 12-month research effort is to understand the counter-intuitive basic physics of proposed non-Foster-element-based active broadband metamaterials. This clear physical insight should lead to the design strategy of real-world broadband active ‘near-zero’ metamaterials for cloaking applications as well as for the delay compensation in communication systems. In addition, one may expect that the incorporation of active elements into the metamaterial structure may cause instabilities. It is not clear whether it is possible to use some of known methods for instability prediction or some entirely new approach needs to be developed. In addition, it is necessary to analyze the feasibility of manufacturing of broadband non-Foster-elements-based active metamaterials in RF and microwave range, at the present state of the art. Eventually, it could be possible to develop a simple RF demonstrator of a broadband active ENZ metamaterial as a proof-of-concept of proposed theoretical approach.

The work in the project has been divided in the following tasks:

1. Re-examination of fundamental energy-dispersion constraints for ‘negative’ (**NG**) and ‘near-zero’ (**NZ**) metamaterials, which cause inherent narrowband operation. In the case of ordinary continuous material, these constraints are well-funded and they have been known for many years. In spite of that, their applications in either volumetric inclusion-based or the transmission-line-based metamaterials is not clear and, unfortunately, widely misinterpreted or even overlooked.
2. Analysis of counter-intuitive physics of broadband operation of proposed non-Foster-elements-based metamaterials. Analysis of the stability issue and development of self-consistent theoretical approach for predicting stability in arbitrary structure.
3. Development of novel design of broadband 1D and 2D active ENZ metamaterial for cloaking applications. Feasibility study of manufacturing of negative capacitors and negative inductors in RF and microwave range, at the present state of the art.



4. Manufacturing of a prototype (a demonstrator) of a broadband dispersionless 1D RF active ENZ metamaterial. Measurement of the basic properties of the prototyped metamaterial in order to verify the correctness of proposed novel approach.

The main realized outcomes of the project are:

- We have analyzed the basic energy-dispersion constraints in the case of passive metamaterials. We have found that these fundamental constraints inevitably lead to resonant behavior in the case of all passive metamaterials regardless of their technological realization (SRR-based, wire-based, transmission-line-based e.t.c.). This is in contrast to usually accepted opinion that the transmission-line metamaterials are of non-resonant nature. We have found that the operating bandwidth of the transmission-line-based metamaterials is wider than the bandwidth of volumetric inclusion-based metamaterials (e.g. SRR-based) only due to different kind of dispersion (Drude model instead of Lorentz model). However, the fundamental resonant behavior that limits the operating bandwidth is always present.
- We have developed a novel topology of transmission-line-based broadband dispersionless ENZ metamaterial that makes use of 1D or 2D transmission line periodically loaded with lumped negative capacitors. Briefly, if absolute value of negative capacitance is chosen to be slightly lower than the distributed capacitance of the transmission line, the net distributed capacitance will be positive assuring stable operation. At the same time, the equivalent relative permittivity will be lower than 1, yielding broadband dispersionless ENZ metamaterial with superluminal phase velocity and almost flat dispersion curve.
- We have made a detailed investigation of the stability properties of the networks that contain negative non-Foster elements in general, and 1D ENZ and MNZ metamaterials in particular. Surprisingly, we have found that commonly used frequency domain approaches for stability analysis (such as Rollet stability factor) give wrong predictions. This happens due to the fact that negative capacitors and negative inductors always have zeroes in RHS of a complex plane or, practically speaking, they always make use of positive feedback. Therefore, one should use the analysis in time domain. We have also found that commonly accepted rule that a sum of the capacitances (or inductances) along a closed mesh should be positive number for stable operation, is not always valid. Actually, we have found that the stability criteria depend not only on the negative elements but also on the topology of the remaining passive part of the network. We have found possible to predict the stability for every network topology and to find the design that assures stable operation of any ENZ or MNZ metamaterial (but not for the case of ENG, MNG or DNG metamaterials).
- We have analyzed known designs of negative capacitors and successfully developed several prototypes using BJT, FET and OPAMP technology. Specifically, we have developed negative capacitors in 2 MHz-40 MHz RF range, in 20-100 MHz RF range and in 1-2 GHz range. We have developed appropriate 1D and 2D ENZ unit cells, extracted effective permittivity and verified broadband operation. Finally, we have developed the entire three-cell 1D active ENZ metamaterial that has fractional operating bandwidth of 200%. Obtained bandwidth is significantly better than a bandwidth of every passive metamaterial available at present. We have also found that this broadband behavior is accompanied with counter-intuitive superluminal phase and group velocities.

Chapter 3 BANDWIDTH LIMITATIONS OF PASSIVE MATERIALS (OR METAMATERIALS)

## Bandwidth limitations of passive materials (or metamaterials)

### 3.1. Importance of the dispersion issue in metamaterials

In the introduction it was highlighted that the inherent dispersion of every SNZ, DNZ, SNG or DNG metamaterial causes narrowband operation of particular metamaterial-based device. A typical example is electromagnetic cloak [12-14]. Commonly used (simplified) explanation of a coordinate transformation 2D cloak [13,14] is sketched in Figure 3-1.

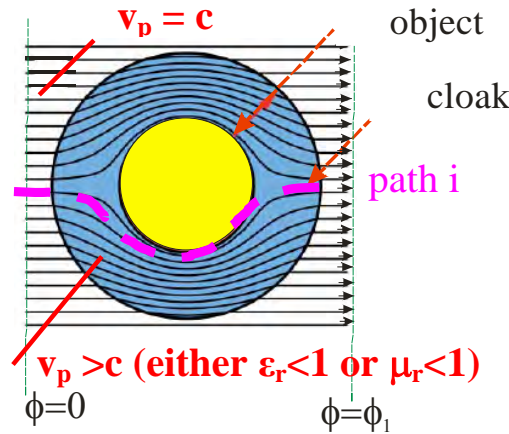


**Figure 3-1** EM wave propagation inside the cloak

It depicts a plane wave impinging on an object covered by an ideal cloak. The ideal cloak is a lossless shell constructed in such a way that it does not allow the existence of scattered field. Therefore, the distribution of the EM fields on an arbitrary plane behind the object (both amplitude and phase) must be equal to the distribution that would exist on the same plane if there were no object. The cloak should actually 'bend' the flow of EM energy around the object, maintaining unchanged the amplitude and phase distributions on the observation plane. Each 'ray' should travel along a path that is obviously longer than the path in free-space, which means that the phase velocity ( $v_p$ ) must be greater than the speed of light ( $c$ ). In other words, this type of cloak must employ anisotropic materials that, within some spatial regions, have either local relative effective permittivity ( $\epsilon_r$ ) or local relative effective permeability ( $\mu_r$ ) greater than zero, but smaller than one (an ENZ material with  $0 < \epsilon_r < 1$  or an MNZ material with  $0 < \mu_r < 1$ ).

On the other hand, an isotropic 'plasmonic cloak' [12] is based on the (imperfect) cancellation of the EM field scattered from the target and the EM field scattered from the

shell. Since the target and the shell are of spherical or cylindrical shape, one can use exact Mie analysis of the scattering process. If both the target and the shell are electrically small, one finds that the dipolar scattered field is much more pronounced than other higher terms. In addition, if the polarizability vector of the shell and the polarizability vector of the dielectric target are antiparallel, the corresponded fields will cancel each other. It can be achieved only if the relative dielectric constant of the cover is *smaller than one* [12]. Thus, although the plasmonic cloak [12] makes use of the different background physics comparing to the anisotropic transformation cloak [13], the design requirement for relative dielectric constant lower than one ( $0 < \epsilon_r < 1$ ) is again an imperative.

A very important parameter of both cloak types is the phase shift  $\Delta\Phi_i$  along some differential segment of an arbitrary path  $i$  (see Figure 3-1):

$$\Delta\phi_i = -d_i \frac{\omega}{c} \sqrt{\epsilon_r(i, \omega) \mu_r(i, \omega)}. \quad (3.1)$$

Here,  $d_i$  is the differential path length and  $\omega$  is the angular frequency. The arguments of the material parameters  $(i, \omega)$  emphasize that the effective permittivity and permeability may depend both on the spatial coordinates (anisotropy) and the frequency (dispersion). If dispersion is present, the change in the material parameters  $(\mu, \epsilon)$  will cause a change in the phase shift for each path depicted in Figure. This change in the phase shift obviously affects the operation of the cloak. Can this influence be neglected? If not, is it possible to construct a dispersionless ENZ (or MNZ) metamaterial that might enable broadband cloaking? In this study, we will try to give answers on these fundamental questions.

In order to get rough estimate of the influence of dispersion on the cloaking, the phase shift per unit width of a slab was calculated using (3.1), and the results are sketched in Figure 3-2.

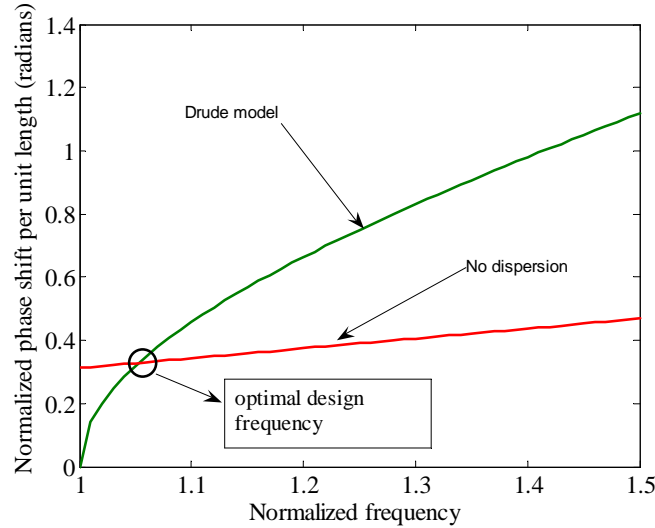


**Figure 3-2** Calculated phase shift of materials with different dispersion

Two types of materials were used in this calculation. The first slab (green solid line) was assumed to be made out of ordinary material that obeys Drude dispersion model (e.g. wire-based metamaterial [5]). The second slab was assumed to be made out of hypothetical dispersionless ‘plasma-like ENZ’ ( $0 < \epsilon_r < 1$ ) material. It is clear that dispersionless passive metamaterial does not exist in reality (later, it will be shown possible to construct it using active non-Foster elements). The optimal permittivity for efficient plasmonic cloaking (taken from the numerical example in [12]) is also marked. It can be seen that the change in

frequency does cause significant deviation of the permittivity from the optimal value. This (unwanted) effect is obviously much more pronounced in the case of ordinary plasmonic slab with Drude dispersion.

The operating bandwidth of an isotropic plasmonic cloak [12] (the bandwidth in which the scattering cross section is lower than the scattering cross section of the target) is about 10%. A recent analytical study [14] revealed that the anisotropic cloak reported in [13] has an operating bandwidth of only 0.24 %. Thus, it appears that the material dispersion is indeed a major limiting factor on the operating bandwidth of the proposed cloaking devices (and all other devices, operation of which depends on the accuracy of equivalent parameters of **NZ** or **NG** metamaterials). Therefore, the dispersion issue in passive metamaterials is analyzed in details in following chapters.

## 3.2. Energy-dispersion constraints

### 3.2.1 Basic issue of resonant energy redistribution

In order to understand the dispersion issue, it is convenient to analyze the reactive energy stored within the differential volume of vacuum:

$$W_0 = W_e + W_m = \frac{1}{2} \epsilon_0 |E|^2 + \frac{1}{2} \mu_0 |H|^2. \quad (3.2)$$

Here,  $W_e$  and  $W_m$  stand for the energy (per unit volume) stored in electric ( $E$ ) and magnetic field ( $H$ ) respectively. The symbol  $\epsilon_0$  is the free-space permittivity while  $\mu_0$  stands for free-space permeability. From (3.2) it is clear than a half of the energy is stored in electric field while the other half is stored in magnetic field.  $W_0$  is energy stored within some space in the vacuum and it is *the lowest possible* amount of net energy stored in any material.

Let us now suppose that some lossless material is placed within the same volume. The electric and magnetic polarizations will take place and the stored energy *is increased* (clearly, some work should be done in order to polarize the material):

$$W = W_e + W_m = \frac{1}{2} \epsilon_0 \epsilon_r |E|^2 + \frac{1}{2} \mu_0 \mu_r |H|^2, \quad \epsilon_r > 1, \mu_r > 1 \Rightarrow W > W_0. \quad (3.3)$$

Here,  $\epsilon_r$  and  $\mu_r$  are relative permittivity and permeability, respectively. The conclusion of the energy increase ( $W > W_0$ ) is valid only if both  $\epsilon_r$  and  $\mu_r$  are positive numbers.

In the case of NG ( $\epsilon_r < 0$  or  $\mu_r < 0$ ), or **NZ** (meta)materials ( $0 < \epsilon_r < 1$  or  $0 < \mu_r < 1$ ), the interpretation becomes problematic. For instance, if there is an ENZ material ( $0 < \epsilon_r < 1$ ) located within analyzed volume of space, the net energy appears to be *decreased*:

$$W = W_e + W_m = \frac{1}{2} \epsilon_0 \epsilon_r |E|^2 + \frac{1}{2} \mu_0 |H|^2, \quad \epsilon_r < 1 \Rightarrow W < W_0. \quad (3.4)$$

This result ( $W < W_0$ ) is obviously incorrect. It is impossible that the net energy in any material ( $W$ ) becomes lower that the net energy stored in vacuum ( $W_0$ ). But, on the other side ,it is well known that there are some materials with ENZ behavior (a simple example is a cold plasma operating slightly above its plasma frequency). The explanation of this contradiction is the fact that (3.1) and (3.2) are not the general equations. Equations (3.1) and (3.2) are valid

only in the case of dispersionless positive (DPS) materials. The most general (macroscopic) equation that is always valid (both in the case of dispersive and non-dispersive materials) [16] reads as:

$$W = \frac{1}{2} \frac{\partial[\omega \cdot \varepsilon(\omega)]}{\partial \omega} |E|^2 + \frac{1}{2} \frac{\partial[\omega \cdot \mu(\omega)]}{\partial \omega} |H|^2, \quad W > 0. \quad (3.5)$$

Equation (3.5) shows that, the overall reactive energy stored in every *passive* lossless material (or metamaterial) is always *greater* than the energy stored in vacuum (irrespective of the internal structure of particular metamaterial). At the same time, the net energy must be positive (mathematically speaking, the energy in every passive structure is *strictly positive quantity*,  $W > 0$ ). This fact, together with the causality requirements, leads to:

$$W > 0 \Rightarrow \frac{\partial[\omega \cdot \varepsilon(\omega)]}{\partial \omega} > \varepsilon_0, \quad \frac{\partial[\omega \cdot \mu(\omega)]}{\partial \omega} > \mu_0. \quad (3.6)$$

Equation (3.6) is a strong form of basic energy-dispersion constraints [16] that apply for *every lossless continuous material*.

One should bear in mind that every passive metamaterial has its parts (the inclusions, transmission lines, lumped elements e.t.c) made out of ordinary materials. If these ‘building’ materials are lossless it is clear that the basic energy-dispersion constraints [16] also apply to *every passive metamaterial*, as well. Equation (3.6) can be rearranged into a simple, more convenient form:

$$W > 0 \Rightarrow \frac{\partial[\varepsilon(\omega)]}{\partial \omega} > 0, \quad \frac{\partial[\mu(\omega)]}{\partial \omega} > 0. \quad (3.7)$$

Let us now analyze the energy in some NG (NZ) material (e.g. in a cold plasma). How is it possible to satisfy the requirement that the net energy is higher than the energy in vacuum ( $W > W_0$ ) and (at the same time) the requirement of positive sign of the derivatives in (3.7) ( $(\partial \varepsilon / \partial \omega) > 0$  and  $(\partial \mu / \partial \omega) > 0$ )? The answer deals with the process of resonant energy redistribution between electric and magnetic field.

Let us suppose that there is some energy redistributed from the electric field ( $W_e$ ) into the magnetic field ( $W_m$ ). Thus, the energy in electric field is *lower* than the energy that would be stored within same volume of space in vacuum ( $W_e < W_0$ ). Due to causality, the energy redistribution cannot occur instantaneously but it is dynamic process that occurs within each period of applied EM field. The amount of redistributed energy is a function of frequency and it reaches its maximum at one specific frequency. Thus, the process of energy redistribution is actually *a resonant process* that occurs in *every passive NZ or NG (meta)material*.

### 3.2.2 Mechanical oscillator model of resonant energy redistribution in continuous ENZ or ENG material

There is a very basic (but, at the same time, very intuitive and clear) explanation of the resonant process in continuous material during polarization. (Figure 3-3). At first, let us suppose that there is no external electric field. In that case, the dielectric is electrically neutral due to symmetric distribution of charges. Application of the external electric field displaces charged particles (in the simplest case of electronic polarization these particles are electrons).

Again, this process cannot occur instantaneously due to finite mass of the particle and binding Coulomb's force that opposes to external field (to the driving force). Each polarized particle can be modeled as a simple mechanical oscillator (right part of Figure 3-3). The oscillator comprises a spring (representing the binding force) driven by the external force (the external field) and a weight (representing the mass of the particle). If the frequency of the external field is lower than the resonant frequency of the oscillator, the movement of the weight will be in the direction of the driving force. From the electromagnetic point of view, this movement signifies positive polarization and, therefore, the increase of permittivity ( $\epsilon_r > 1$ ).

On the contrary, if one wants to achieve either the **NZ** behavior ( $0 > \epsilon_r > -1$ ) or the **NG** behavior ( $\epsilon_r < 0$ ) the polarization *should be negative*. The negative polarization actually means the movement of the weight in a direction opposite to the direction of the driving force (Right lower part of Figure 3-3). From very basic physics of mechanical oscillators it is known that this 'inverse movement' can happen only within a narrow frequency band above the resonant frequency. The bandwidth of this frequency band depends on the losses in a system. Within this band, the potential energy of the weight (an analog to the energy in the electric field  $W_e$ ) is redistributed into the kinetic energy that squeezes the spring (an analog to the energy in the magnetic field  $W_m$ ). Actually, the amplitude and phase of mechanical oscillations can be represented by Lorentz model (Figure 1-3). Thus, the energy redistribution and the resonant behavior in all continuous **NZ** or **NG** materials are *inevitable*.

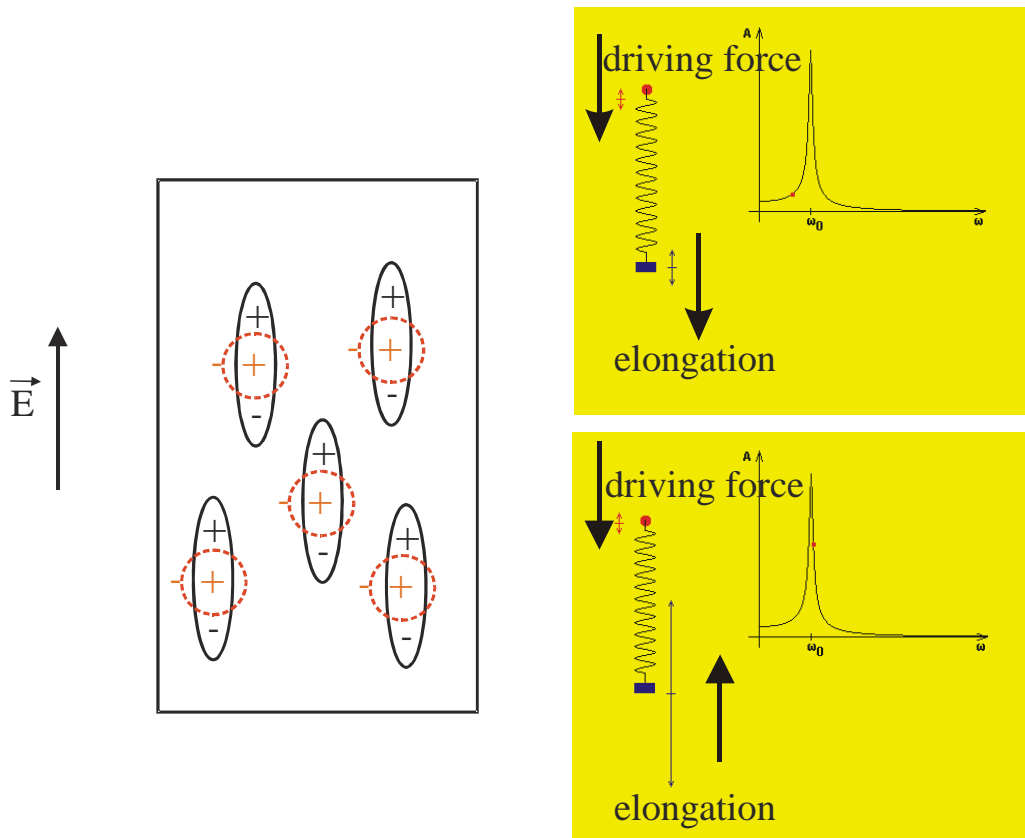


**Figure 3-3** Resonant process in continuous material (the graphs have been taken from <http://www.walter-fendt.de/ph14e/resonance.htm>)

### 3.2.3 LC circuit model of resonant energy redistribution in ENZ or ENG metamaterial

The resonant energy redistribution and dispersion can also be explained using very simple electromagnetic model of an inclusion of a volumetric metamaterial (Figure 3-4). For instance, let us analyze the simplest inclusion that comprises just two parallel PEC plates with the dimensions  $\Delta x$  by  $\Delta x$ , located at the mutual distance  $\Delta x$  (Left part of Figure 3-4).

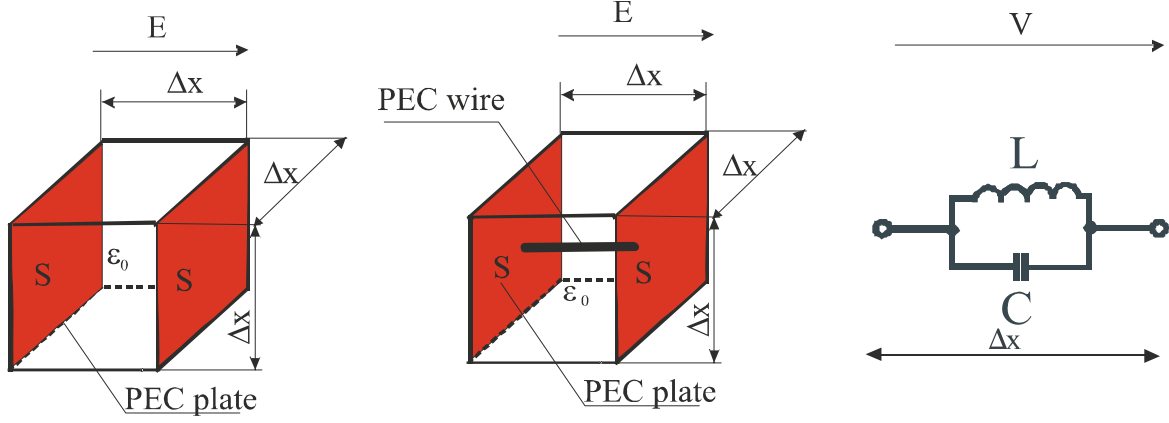


**Figure 3-4** LC circuit model of an inclusion in passive metamaterial, **Left** - an electric inclusion, **Middle** - an electric inclusion with energy redistribution from electric into the magnetic field, **Right** – an equivalent circuit

The inclusion is driven by the electric field  $E$ , a vector of which is perpendicular to the PEC plates. Obviously, this inclusion can be thought of a short dipole or, even simpler, just of a parallel-plate capacitor  $C$ . If one wants to obtain the ENZ or ENG behavior, the energy stored in the capacitor should be lower than the (quasi-electrostatic) energy stored within same volume ( $\Delta x^3$ ) of vacuum. This energy can be calculated easily using very basic equations:

$$W_C = \frac{V^2 C}{2} = \frac{(E\Delta x)^2 \varepsilon_0 \frac{\Delta x^2}{\Delta x}}{2} = \varepsilon_0 \frac{E^2}{2} \Delta x^3 = \frac{W_0}{2}. \quad (3.8)$$

Here,  $V$  stands for the voltage across the capacitor. From (3.8) it can be seen that the minimal stored energy within the inclusion is again limited by the energy stored in vacuum ( $W_0$ ). In addition, (3.8) puts the important limits on the physical construction of an inclusion. From (3.8) one easily finds the value of capacitance:

$$C = \varepsilon_0 \frac{\Delta x^2}{\Delta x} = \varepsilon_0 \Delta x. \quad (3.9)$$

This is a very important result. It shows that the free-space permittivity limits minimal value of the capacitance of any realistic capacitor (a capacitor that occupies a finite volume of space). In other words, every inclusion that stores energy solely within the electric field cannot achieve the ENZ or ENG behavior (or equivalently, the effective permittivity of particular metamaterial cannot be smaller than  $\varepsilon_0$ ). This would be possible if one constructed a capacitor with capacitance  $C < \varepsilon_0 \Delta x$ .

Following the discussion in the previous paragraph, one could suppose that the ENG or ENZ behavior would become possible by incorporation of some element that causes energy redistribution from the electric field into the magnetic field. The simplest way would be just to connect PEC plates with a piece of wire (middle part of Figure 3-4). In that case, there would be the conduction current flowing in the wire that (due to Ampere's law) induces the magnetic field. Thus, there will be an increase of the energy stored in the magnetic field in the vicinity of a wire. Obviously, this wire performs as a lumped inductor  $L$  connected in parallel



to the capacitor  $C$ . Thus, the equivalent circuit is a simple LC resonator (Right part of Figure 3-4). Formally, one can derive the effective capacitance and effective relative permittivity of this circuit (that relates to homogenized relative permittivity of analyzed metamaterial):

$$Y = j\omega C - j\frac{1}{\omega L} = j\omega \left( C - \frac{1}{\omega^2 L} \right) \Rightarrow C_{eff} = C - \frac{1}{\omega^2 L}, \quad (3.10)$$

$$\varepsilon_{reff} = \frac{C_{eff}}{\varepsilon_0 \Delta x} = \frac{C - \frac{1}{\omega^2 L}}{\varepsilon_0 \Delta x} = \frac{\varepsilon_0 \Delta x - \frac{1}{\omega^2 L}}{\varepsilon_0 \Delta x} = 1 - \frac{1}{\omega^2 \varepsilon_0 L \Delta x} = 1 - \frac{\omega_p^2}{\omega^2}, \quad \omega_p = \frac{1}{\sqrt{L \varepsilon_0 \Delta x}}. \quad (3.11)$$

Here,  $Y$  stands for the admittance. It can be seen that both the effective capacitance (3.10) and effective permittivity (3.11) are *function of frequency*, thus, they are *dispersive*. Furthermore, they obey Drude model (lower part of Figure 1-3) with  $\omega_p$  being the plasma frequency. Thus, the effective capacitance and effective permittivity can take arbitrarily low values (including the negative ones). This is a direct consequence of the resonant energy redistribution that occurs within the inclusion (within the resonant LC circuit).

Very similar analysis can be performed for a simple magnetic inclusion (a small loop that acts as an inductor). This analysis shows that the minimal inductance is limited by the free-space inductance:

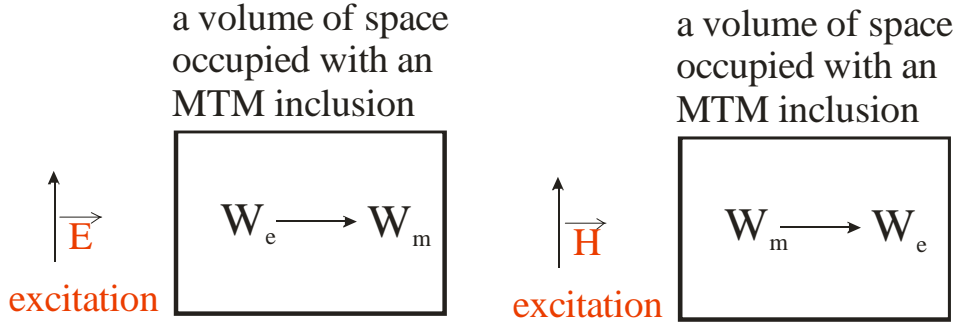
$$L = \mu_0 \Delta x. \quad (3.12)$$

Similarly to the previously analyzed case of an electric inclusion, one can terminate a loop with a lumped capacitor. This modified inclusion can be modeled as series LC resonant circuit (as it will be shown later, this model applies in the case of a SRR inclusion). The effective inductance and effective relative permeability of this circuit are again described by Drude model:

$$Z = j\omega L - j\frac{1}{\omega C} = j\omega \left( L - \frac{1}{\omega^2 C} \right) \Rightarrow L_{eff} = L - \frac{1}{\omega^2 C}, \quad (3.13)$$

$$\mu_{reff} = \frac{L_{eff}}{\mu_0 \Delta x} = \frac{L - \frac{1}{\omega^2 C}}{\mu_0 \Delta x} = \frac{\mu_0 \Delta x - \frac{1}{\omega^2 C}}{\mu_0 \Delta x} = 1 - \frac{\omega_p^2}{\omega^2}, \quad \omega_p = \frac{1}{\sqrt{C \mu_0 \Delta x}}. \quad (3.14)$$

Although above analysis might look trivial, its consequences are far reaching and often overlooked in metamaterial community. They show that *every passive metamaterial* that has either ‘negative’ (**ENG**, **MNG**) or ‘near-zero’ (**ENZ**, **MNZ**) behavior must contain some kind of a resonator. The energy redistribution *always* takes place within the resonator (either from the electric field into magnetic field or vice versa (Figure 3-5)). Thus, the ‘negative’ or ‘near-zero’ behavior will always be narrowband, irrespectively of the internal structure of given metamaterial.

**MTM with  $\epsilon < \epsilon_0$** **MTM with  $\mu < \mu_0$** **Figure 3-5** Schematic explanation of resonant energy redistribution in passive metamaterial**3.3. Circuit-theory properties of passive metamaterials**

In the previous paragraph it was shown that passive (realistic) lumped reactive elements cannot have arbitrary values. Specifically, the minimal capacitance of a capacitor cannot be lower than  $\epsilon_0 \Delta x$  and the minimal inductance of an inductor cannot be lower than  $\mu_0 \Delta x$  (it is assumed that an element occupies volume of  $\Delta x^3$ ). Clearly, passive dispersionless ‘negative capacitors’ or ‘negative inductors’ (or passive dispersionless NZ or NG metamaterials) cannot exist. This is a direct consequence of the energy-dispersion constraints (3.7).

**3.3.1 Foster reactance theorem**

It is known that it is possible to construct passive NZ or NG metamaterials, but they are always dispersive. From circuit-theory point of view, these metamaterials are based on passive, purely reactive networks. Input impedance of such a network behaves as a ‘negative capacitor’ or a ‘negative inductor’, but only within the finite frequency band. In other words, the achieved value of effective capacitance can be lower than  $\epsilon_0 \Delta x$  (or value of effective inductance can be lower than  $\mu_0 \Delta x$ ) within *some finite frequency band*. This frequency dependence (the dispersion) is a consequence of a resonant energy redistribution again imposed by the energy-dispersion constraints (3.7).

The energy distribution is not a unique property of the previously analyzed simple LC circuit. It also occurs (in a more complicated manner that includes more resonant frequencies) within any reactive network that may contain arbitrary number of capacitors and inductors, connected in arbitrary topology. It actually means that the behavior of reactance and susceptance of any *arbitrary passive reactive lossless network* is again constrained by the energy-dispersion constraints (3.7):

$$\frac{\partial[X(\omega)]}{\partial\omega} > 0, \quad \frac{\partial[B(\omega)]}{\partial\omega} > 0. \quad (3.15)$$

The symbols  $X$  and  $B$  stand for the reactance and susceptance, respectively. Equation (3.15) is well-known Foster reactance theorem [17]. Since the reactive networks can have both parallel and series resonances, a reactance  $X(\omega)$  and a susceptance  $B(\omega)$  have both zeroes and poles.

There are some simple properties of  $X(\omega)$  and  $B(\omega)$  of Foster networks:

- Poles and zeros exist only on the real frequency axis
- Poles alternate with zeros
- A pole or zero exists at zero and at infinity

Listed properties actually show that the frequency dependence of either  $X(\omega)$  or  $B(\omega)$  again follows Lorentz (or Drude) dispersion model. These models can be multi-resonant and the number of the resonant frequencies (excluding the resonances at  $\omega=0$  and  $\omega=\infty$ ) is given by  $n-1$ ,  $n$  being the number of reactive elements in the network.

### 3.3.2 Reactance (susceptance) curves of typical metamaterial inclusions

It has been shown that the simplest metamaterial inclusions are the electric and magnetic dipoles. These inclusions are driven by either electric or magnetic field and they can be modeled as parallel and series LC circuits, respectively. Using properties of Foster networks one can easily plot the reactance (or susceptance) of these basic inclusions (Figure 3-6). These plots are very helpful in understanding the basic physics of the ENZ behavior (or the ENG behavior).

For instance, a series LC circuit (a model of capacitively loaded loop) shows capacitive behavior below the resonant frequency and an inductive behavior above it. The entire reactance curve can be interpreted as a dispersive inductance (i.e., the dispersive permeability). Thus, below the resonant frequency, the analyzed metamaterial shows (dispersive) MNG behavior. Furthermore, slightly above the resonant frequency there is (dispersive) MNZ behavior. The dispersion curve follows Drude model, with the angular plasma frequency being equal to the resonant frequency of the series LC circuit. The bandwidth in which one observes the MNG behavior (denoted with BW in Figure 3-6) directly depends on the steepness of the curve (i.e. on the plasma frequency). Of course, the dispersion bandwidth (DBW), depends both on the plasma frequency and on the frequency at which permeability has the required value. This dispersion bandwidth (DBW) is always narrower than usually defined bandwidth (BW). Very similar conclusions (but with the ENG and ENZ behavior) can easily be reached for the case of a parallel LC circuit (Right part of Figure 3-6).).

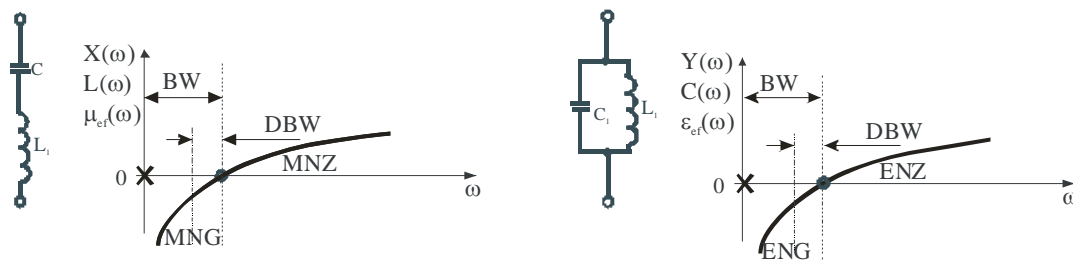


**Figure 3-6** Reactance (susceptance) of idealized lossless NZ (NG) inclusions, **Left** - series LC circuit, **Right** - parallel LC circuit

Above analysis is, of course, very simplified and it neglects the mutual interaction between the neighboring inclusions. In other words, it is assumed that each inclusion is solely driven by the same electric field (or the same magnetic field). From circuit-theory point of

view, it means that each inclusion is driven by an ideal voltage (or current) source and there are no additional coupling elements. In practice, it will be the case only if the inclusions are very tightly coupled to the driving fields (typical example is the transmission line metamaterial [3,4]).

If the coupling between the field (or a host transmission line) and an inclusion is not so strong, the coupling element should be taken into account, as well (Figure 3-7).

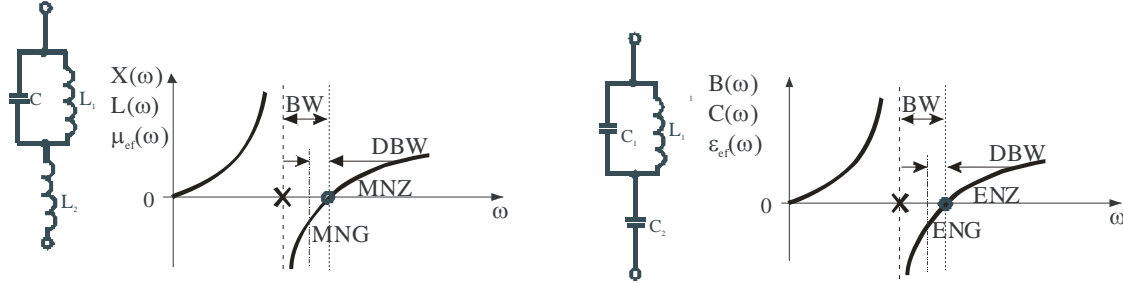


**Figure 3-7** Reactance (susceptance) of coupled lossless  $LC$  inclusions , **Left** - series inductive coupling, **Right** - series capacitive coupling

Since the whole network is still lossless, it again obeys Foster theorem. Immediate consequence is an additional parallel resonant frequency (a pole) and, therefore, the curve now follows Lorentz dispersion model. It can be shown that the reactance (susceptance) function of Lorentz model is always steeper than the associated function of Drude model:

$$\frac{\partial[X(\omega)_{\text{Lorentz}}]}{\partial\omega} > \frac{\partial[X(\omega)_{\text{Drude}}]}{\partial\omega}, \quad (3.16)$$

$$\frac{\partial[B(\omega)_{\text{Lorentz}}]}{\partial\omega} > \frac{\partial[B(\omega)_{\text{Drude}}]}{\partial\omega}. \quad (3.17)$$

So, the metamaterials with Drude dispersion model *are always broader* than the metamaterials with Lorentz model:

$$\begin{aligned} \mathbf{BW}_{\text{Drude}} &> \mathbf{BW}_{\text{Lorentz}}, \\ \mathbf{DBW}_{\text{Drude}} &> \mathbf{DBW}_{\text{Lorentz}}. \end{aligned} \quad (3.18)$$

This is the only reason while the transmission line metamaterials have broader bandwidth than the SRR-based metamaterials (although it is usually incorrectly believed that the transmission-line metamaterials are of non-resonant nature).

### 3.3.3 Influence of finite losses

Strictly speaking, the energy-dispersion constrains (3.7) and Foster reactance theorem (3.15) are valid only in lossless case. However, this restriction is frequently ignored in practice, which sometimes leads to the incorrect conclusions. In introduction chapter it was

explained intuitively that the real and imaginary part of effective permittivity or permeability are always mutually dependent. From circuit-theory point of view, the real and imaginary parts of any impedance are connected via Kramers-Kronig relations [17]. This issue can simply be analyzed by the  $Q$ -factor of the network [17]. A simple example of a lossy ENZ (ENG) inclusion (a parallel  $RLC$  circuit) is shown in Figure 3-8. It is clear than in the case of no losses ( $R=\infty$ ), the impedance does not have a real part and  $Q$  factor (defined here as  $R/(\omega L)$ ) is infinite. The whole impedance curve (in case of no losses this curve is actually identical to the reactance curve) obeys Foster theorem.

Let us suppose that some small losses ( $Q=50$ ) are added to the circuit. Now, the familiar bell-shaped real part of the impedance (and, therefore, the imaginary part of the effective permittivity or permeability) appears. Both the BW and DBW bands are now broader, but, of course, at the cost of the insertion loss. It can be seen that Foster theorem ( $(\partial X/\partial \omega) > 0$ ) is still obeyed in the most parts of the curve. There is only rather narrow band around the resonant frequency, in which ( $(\partial X/\partial \omega) < 0$ ) i.e. the band in which Foster theorem does not apply. This is a circuit-theory version of the well-known phenomenon of anomalous dispersion [16]. Some authors use this part of the curve in order to achieve superluminal behavior with negative group delay in so-called dispersion engineering [18,19]. Unfortunately, this approach is accompanied with huge losses that might be compensated with additional gain, but at the cost of complexity.

Further increase of the loss ( $Q=10$ ,  $Q=5$ ,  $Q=1$ ) further broaden s both the BW and DBW bands with ENG and ENZ behavior as well the bands with anomalous dispersion. The slope of both part of the curves is now lower, i.e. the metamaterial dispersion is *less pronounced*, but again, at the cost of large losses.

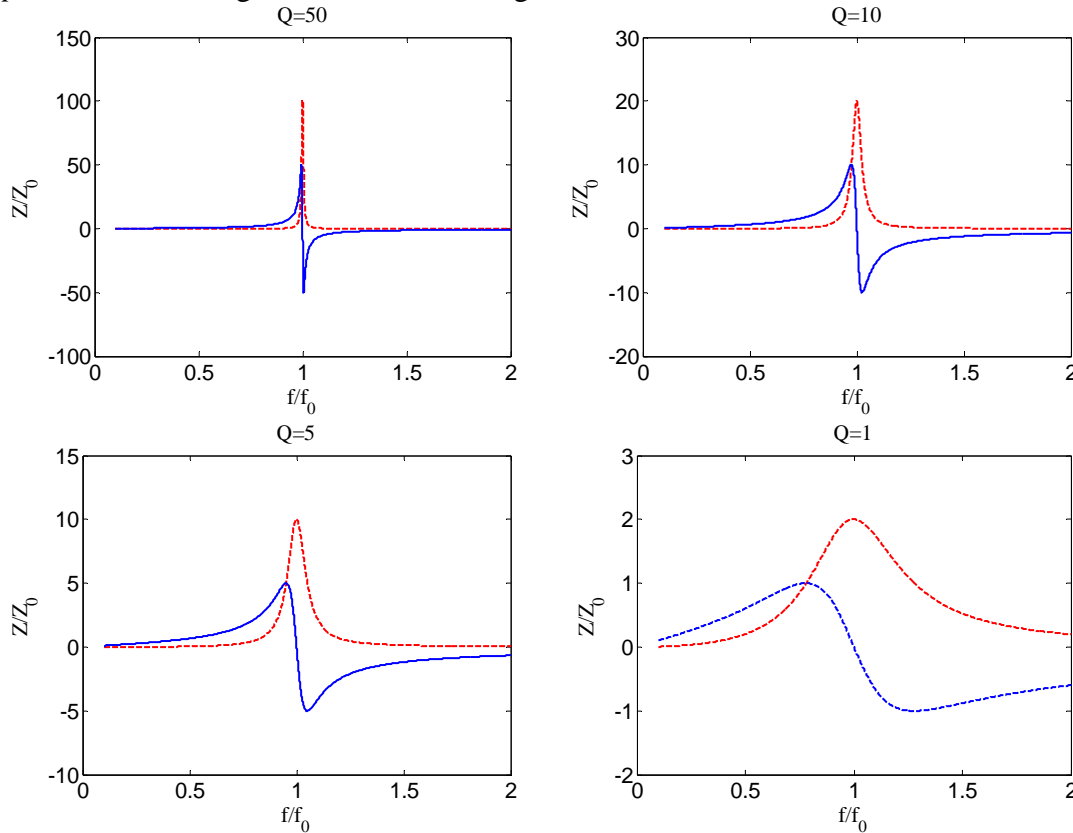


**Figure 3-8** Impedance of a simple parallel LC circuit with loss (a simple ENZ or ENG inclusion). **Solid line** – imaginary part, **Dashed line** – real part.

### 3.4. Dispersion and bandwidth of typical passive metamaterials

In this paragraph, the dispersion and bandwidth of several widely used passive metamaterials are analyzed using a simplified, intuitive approach.

#### 3.4.1. Wire medium

It is well known [1-5, 20] that an array of parallel wires (Figure 3-9), the lattice constant ( $a$ ) of which is *much smaller* than the wavelength ( $d \ll \lambda$ ), can be thought of as a plasma-like material (ENG metamaterial) described by its relative permittivity [2-5]:

$$\varepsilon_{\text{reff}} = \varepsilon'_{\text{reff}} - j\varepsilon''_{\text{reff}} = 1 - \frac{\omega_p^2}{\omega^2 - j\gamma\frac{\omega}{2\pi}}. \quad (3.19)$$

Here,  $\omega$  and  $\omega_p$  represent the (angular) frequency of the signal and the cut-off frequency of the array ('plasma frequency'), respectively, while factor  $\gamma$  represents the losses (see the graph in the middle part of Figure 3-10). The plasma frequency is dependent on the geometrical parameters of the array (lattice constant  $a$  and wire radius) and several different equations for its prediction are available in the literature [1-4].

The operation of wire medium illuminated with a plane wave can be explained in rather intuitive way with the help of the transmission line equivalent circuit (Right part of Figure 3-9). The analogy is based on the formal similarity between Helmholtz wave equation that describes propagation within infinite continuous material (3.20) and the transmission-line wave equation (3.21):

$$\nabla^2 E = -\omega^2 \mu \varepsilon E = (j\omega\mu)(j\omega\varepsilon)E, \quad (3.20)$$

$$\frac{\partial^2 V}{\partial x^2} = -ZYV = (j\omega X_{\text{series}})(j\omega Y_{\text{shunt}})V, \quad (3.21)$$

$$\mu = X_{\text{series}} = \frac{Z}{j\omega}, \quad \varepsilon = Y_{\text{shunt}} = \frac{Y}{j\omega}. \quad (3.22)$$

One immediately recognizes 'one by one' correspondence between  $E$  and  $V$ . There is also a correspondence between  $\varepsilon$  and  $\mu$  and the distributed series reactance  $X_{\text{series}}$  and the shunt admittance  $Y_{\text{shunt}}$  (3.22), (Figure 3-9).

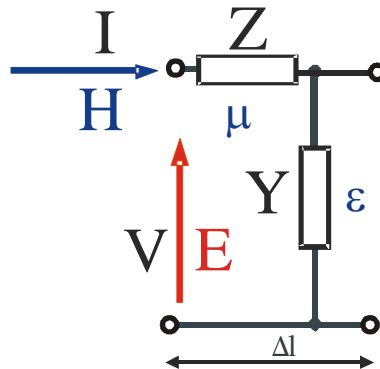


**Figure 3-9** Transmission-line equivalent circuit of passive metamaterial

Therefore, the free space can be thought of a transmission line with a series distributed inductance and a shunt distributed capacitance representing the free-space permeability ( $\mu_0$ ) and permittivity ( $\epsilon_0$ ), respectively (Left part of Figure 3-10). Let us assume a plane wave that impinges the wires at normal incidence. The wires are parallel to the electric field vector, and they can be thought of the distributed inductance ‘connected’ in parallel with free-space permittivity ( $\epsilon_0$ ). These two elements form a parallel LC tank circuit that behaves as a shunt inductance below the resonant frequency ( $\omega_p$ ). Thus, the whole structure behaves as a LL transmission line that can be interpreted as an ENG metamaterial. The ENG behavior comes from the previously explained resonant energy redistribution (there is a lack of the energy in the electric field because some energy is redistributed into the magnetic field, i.e. there is energy exchange from ‘a capacitor’ into ‘an inductance’). It is important to notice that the losses of wire media operating in the ENG region are significantly lower than the losses of widely used Mu-Negative (MNG) media based on Split-Ring Resonators (SRRs). Low losses are associated with the fact that very low current flows through the parallel tank circuit in the vicinity of the resonant frequency ( $\omega_p$ ) (On the contrary, a SRR inclusion behaves as a series tank circuit associated with the high current density and therefore high losses in the vicinity of the resonant frequency). Slightly above the  $\omega_p$ , equivalent relative permittivity of the tank circuit is a small positive number very close to zero (the tank circuit behaves as a shunt capacitance smaller than free-space permittivity). Wire-medium operating in this frequency region behaves as ENZ metamaterial. The background physics is very similar to that in ENG region (resonant energy exchange). If the frequency is increased further, the equivalent permittivity approaches unity.

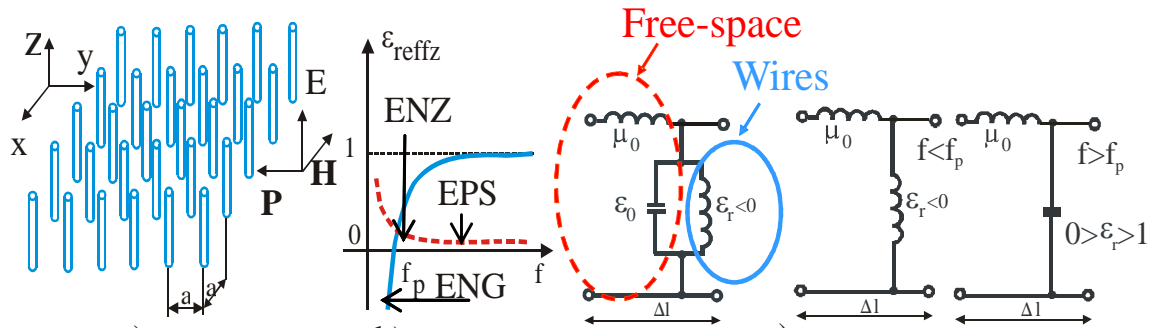


**Figure 3-10** Wire medium, **Left** - physical construction, **Middle** - Dispersion characteristic, **Right** - Transmission-line equivalent circuit

Equation (3.19) applies only if no component of the wave vector is parallel to the wires. If this constraint is not met, the wire-medium exhibits a spatial dispersion. In the case of lossless wires, the effective permittivity of wire medium with spatial dispersion is given by [5]:

$$\epsilon_{\text{reff}} = 1 - \frac{\omega_p^2}{\omega^2 - (q \cdot c)^2} \quad (3.23)$$

Here,  $c$  stands for the speed of light and  $q$  is the component of a wave vector parallel to the wires. In a general case  $q$  may also be dependent on the frequency and  $\epsilon_{\text{reff}}$  becomes a rather complicated function of both geometrical parameters of the array and the frequency.

However, even in this case it is possible to identify several different characteristic regions of the dispersion curve with the ENG behavior, the ENZ behavior and the ordinary positive behavior.

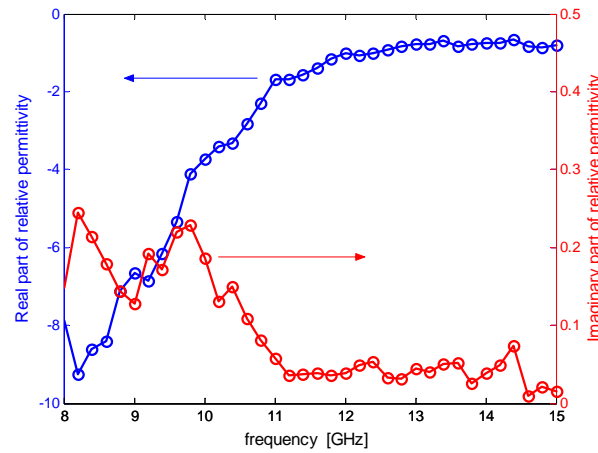


**Figure 3-11** Measured effective permittivity of wire medium [2]

An example of behavior of effective permittivity of typical realistic wire medium (in the case with no spatial dispersion) is shown in Figure 3-11. It can be seen that the real part of extracted relative permittivity qualitatively obeys Drude dispersion model. It can also be noticed that imaginary part of permittivity is rather small (less than 0.25), thus the experimental wire-based ENG metamaterial has low losses. The operating bandwidth (BW) of 58 % and the dispersion bandwidth (DBW) of 16% in ENG part of the curve, have been estimated from Figure 3-11. Finally, the figure of merit that describes loss (FOM) of 10 (defined as ratio of the real and imaginary part of effective permittivity [2-4]) was also estimated from Figure 3-11.

### 3.4.2. Metamaterials based on resonant inclusions (loop-wire, SRR, CSRR)

There are several passive metamaterials based on elemental resonant inclusions. They can be (roughly) divided into the inclusions based on the elemental electric inclusion (a short dipole) and the elemental magnetic inclusion (a small loop). (These are actually parallel and series LC circuits analyzed in chapter 3.3.2). The basic operation of elemental electric inclusion is sketched in the upper part of Figure 3-12.



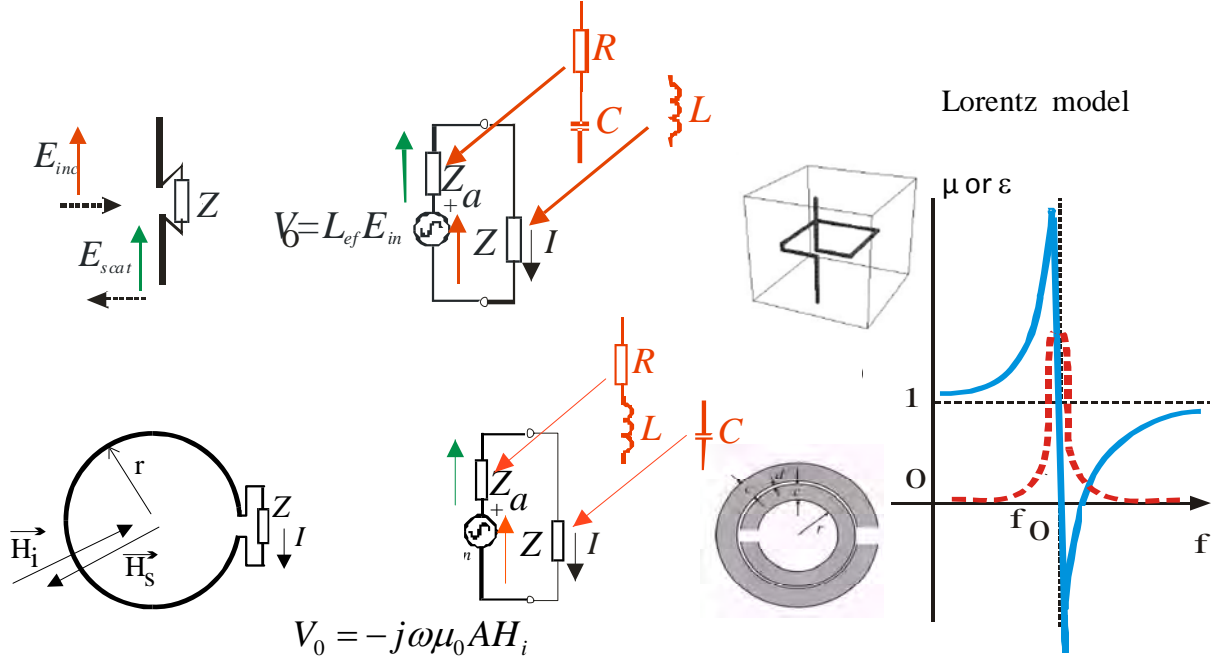


**Figure 3-12** Metamaterials based on resonant inclusions, **Upper** - inductively loaded dipole (loop-wire, CSRR), **Lower** - Capacitively loaded loop (SRR)

It depicts a short dipole loaded with some passive lumped load  $Z$ , illuminated with a plane wave. The equivalent circuit comprises a simple Thevenin voltage source  $V_0$  with internal impedance  $Z_a$  (the self-impedance of an antenna). Assuming that the electric field vector of the incoming plane wave ( $E_{in}$ ) is parallel to the dipole, Thevenin voltage can be found easily:

$$V_0 = L_{ef} E_{in}. \quad (3.24)$$

Here,  $L_{ef}$  stands for the dipole effective length (since the dipole is electrically short, it is actually a half of the geometrical length). The antenna self-impedance can be modeled as a series of a capacitor  $C_a$  and (very small) radiation resistance  $R_a$ :

$$Z_a = R_a + jX_a = R_a - j \frac{1}{\omega C_a}. \quad (3.25)$$

The current flowing within a circuit (a current at the antenna center) is given by:

$$I(0) = \frac{V_0}{Z_a + Z} = \frac{L_{ef} E_{in}}{R_a + jX_a + R + jX}. \quad (3.26)$$

The current  $I$  can be thought of being a superposition of an 'incident current' ( $I_i$ ) and the current 'scattered' from the load ( $I_{sc}$ ) [21]:

$$I(0) = I_i(0) - I_{sc}(0), \quad I_i(0) = \frac{V_0}{Z_a} = \frac{L_{ef} E_{in}}{Z_a}, \quad I_{sc}(0) = \frac{V_0}{Z + Z_a} \cdot \frac{Z}{Z_a} = \frac{L_{ef} E_{in}}{Z + Z_a} \cdot \frac{Z}{Z_a}. \quad (3.27)$$

The incident current is defined as a current flowing through a short-circuited dipole (please note that the net current  $I$  is defined as a difference between  $I_i$  and  $I_{sc}$ ). The induced polarizability  $\alpha$  is proportional to the induced charge along an antenna (thus, it is proportional

to an integral of current in respect to time). In addition, one should take into account the distribution of the current along the antenna. In the case of incident current one should use the current distribution of a short dipole operating in the receiving mode [21]:

$$f_r(x) = I(0) \cdot \left(1 - \frac{x^2}{l^2}\right). \quad (3.28)$$

On the other hand, in the case of the scattered current, one should use the current distribution of a short dipole operating in the transmitting mode:

$$f_t(x) = I(0) \cdot \left(1 - \frac{|x|}{l}\right). \quad (3.29)$$

In (3.27) and (3.28) it was assumed that a dipole is oriented along x axis and its length is  $2l$ . From (3.27) and (3.28) one calculates the polarizability as [21]:

$$\alpha = \frac{1}{E_{in}} \frac{L_{ef}}{j\omega} \int_{-l/2}^{l/2} \left( \frac{1}{R_a + jX_a} f_r(x) - \frac{1}{(R_a + R) + j(X_a + X)} \cdot \frac{R + jX}{R_a + jX_a} f_t(x) \right) dx = \frac{l^2}{j\omega Z_a} \left( \frac{4}{3} - \frac{Z}{Z_a + Z} \right). \quad (3.30)$$

At this point, it is convenient to look at the physical interpretation. As it was previously discussed, in order to achieve ENG (or ENZ) behavior one should get negative polarizability. Therefore, a phase of polarizability  $\alpha$  should be close to 180 degrees:

$$\arg(\alpha) \approx 180^\circ \Rightarrow \arg \left[ \frac{l^2}{j\omega Z_a} \left( \frac{4}{3} - \frac{Z}{Z_a + Z} \right) \right] \approx 180^\circ. \quad (3.31)$$

Inspection of (3.29) reveals that the required phase shift will occur if the losses are small ( $X_a \gg R_a$ ,  $X \gg R$ ) and the reactance  $X$  and the reactance  $X_a$  have the opposite signs i.e. if the load is an inductor. In Figure 3-13, the phase angle and the real part of polarizability (in lossless case) are plotted qualitatively for two different loads: a lossless inductor and a lossless capacitor.

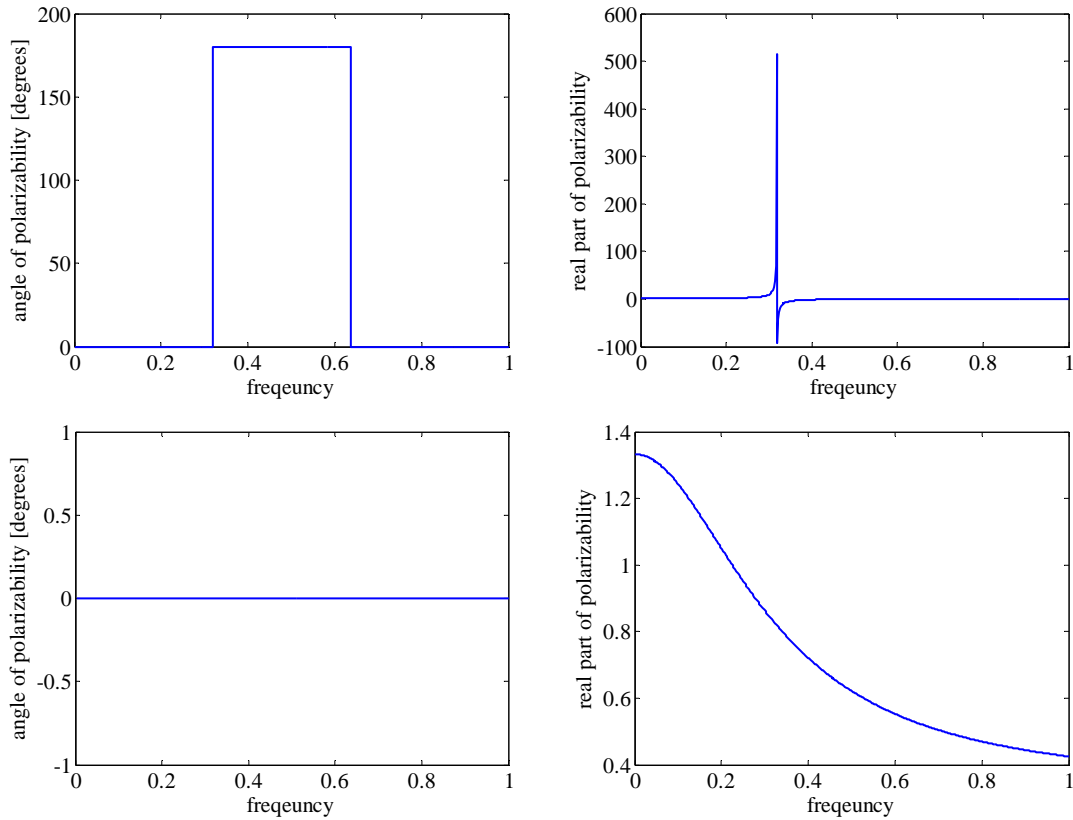


**Figure 3-13** Polarizability of a small electric inclusion, **Upper** – loading element is an inductor, **Lower** - loading element is a capacitor

It can be seen that loading with an inductor results with familiar resonant ENG (and ENZ) behavior of a polarizability. (There are two frequencies with abrupt transition in a phase). This leads to Lorentz dispersion model of equivalent (homogenized) permittivity (Right side of Figure 3-12). Drude model is not applicable here due to a weak capacitive coupling between an incident field and the inclusion (LC circuit). It causes the appearance of additional resonant frequency (a zero in the reactance curve, similar to the right part of Figure 3-7). Taking this into account one easily sketches the transmission line equivalent circuit of metamaterial with array of inductively loaded short dipoles (Figure 3-14);

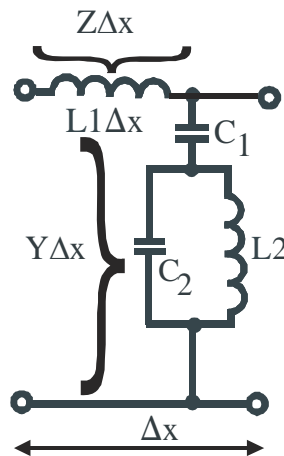


**Figure 3-14** Transmission line equivalent circuit of metamaterial with array of inductively loaded short dipoles

The case of simple capacitive loading (Lower part of Figure 3-13) shows just weak positive polarizability with no resonant phenomenon.

Above conclusion about the resonant behavior with loading inductor can also be achieved in a simpler, more intuitive way. According to the discussion in chapter 3.3.2, it is clear that one should use a loading element that is able to redistribute a part of the energy from electric field stored within capacitive short dipole into the magnetic field. Obviously, the required element is an inductor. Due to required resonant energy exchange one should expect that the polarizability diverges at the resonant frequency. In addition, it should have a positive sign below the resonant frequency and a negative sign above it.

Analogously, one can analyze the operation of a dual particle: a small loaded loop (Lower part of Figure 3-12). A loop antenna is considered being very small (its radius is much smaller than a wavelength), connected to the load with impedance  $Z$  and illuminated with a plane wave with the intensity of the incident magnetic field  $H_i$ . Let us assume that the vector of incident magnetic field is perpendicular to the loop. Using the equivalent circuit sketched in the lower part of Figure 3-12 one derives the expressions for the incident and scattered currents :

$$I = \frac{V_o}{Z_a + Z} = \frac{-j\omega \mu_0 A H_i}{Z_a + Z}. \quad (3.32)$$

$$I = I_i - I_{sc}, \quad I_i = \frac{V_0}{Z_a} = \frac{-j\omega \mu_0 A H_i}{Z_a}, \quad I_{sc} = \frac{V_0}{Z + Z_a} \cdot \frac{Z}{Z_a} = \frac{-j\omega \mu_0 A H_i}{Z + Z_a} \cdot \frac{Z}{Z_a}. \quad (3.33)$$

Here,  $A$  stands for an area of the loop, and  $\mu_0$  is free-space permeability. Obviously, the self-impedance of the loop has inductive character ( $Z_a = R_a + j\omega L_a$ ). Taking this into account one derives the induced magnetic moment ( $m$ ):

$$m = \mu_0 \frac{-j\omega \mu_0 A H_i}{Z_a + Z} = \frac{-j\omega \mu_0^2 A H_i}{R_a + jX_a + R + jX}. \quad (3.34)$$

In the first approximation one can neglect the losses in a load ( $R$ ) and (very small) radiation resistance ( $R_a$ ). Therefore, the expression for induced magnetic moment becomes very simple:

$$m = \frac{-j\omega \mu_0^2 A H_i}{jX_a + jX}. \quad (3.35)$$

Similarly to the previous discussion, in order to achieve the MNG behavior (or the MNZ behavior) one should obtain the negative magnetic moment (thus, the phase angle of  $m$  should be close to 180 degrees):

$$\arg(m) \approx 180^\circ \Rightarrow \arg\left[\frac{-j\omega \mu_0^2 A H_i}{X_a + X}\right] \approx 180^\circ. \quad (3.36)$$

Since this case is a dual of the inductively loaded dipole, it is immediately seen that a use of a capacitive load ( $C$ ) leads to required resonant behavior:

$$m = \frac{-j\omega\mu_0^2AH_i}{jX_a + jX} = \frac{-j\omega\mu_0^2AH_i}{j\omega L - j\frac{1}{\omega C}} = \frac{\mu_0^2\omega^2CAH_i}{1 - \left(\frac{\omega}{\omega_0}\right)^2} \quad \omega_0 = \frac{1}{\sqrt{LC}}. \quad (3.37)$$

However, equation (3.37) fails in the high-frequency limit since the sign of  $m$  remains negative. This behavior is physically incorrect because every (either electric or magnetic) polarization must approach zero if the frequency approaches infinity. From circuit-theory point of view, this drawback is caused by an absence of the coupling element that would add an additional zero in the admittance curve. There are several models available in the literature [2-4] that correct this problem and all of them have the following form of induced magnetic moment:

$$m = K \frac{\omega^2 - \omega_s^2}{\omega^2 - \omega_p^2}. \quad (3.38)$$

Here,  $\omega_p$  and  $\omega_s$  stand for the angular frequency of parallel and series resonance and  $K$  is the constant that depends on the geometry. Clearly, (3.38) leads to Lorentz dispersion model of equivalent (homogenized) permittivity (Right side of Figure 3-12). The graphs for the phase angle and the real part of induced magnetic moment are given in Figure 3-15.

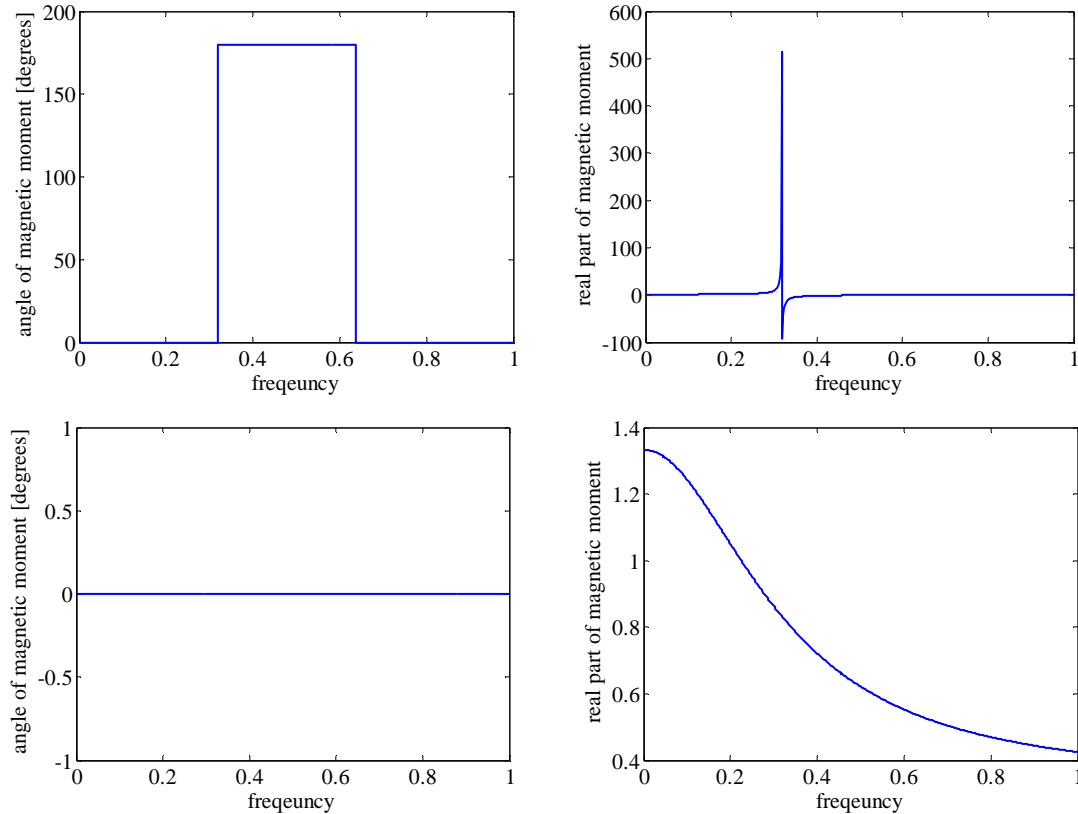


**Figure 3-15** Induced magnetic moment of a small magnetic inclusion, **Upper** – loading element is a capacitor, **Lower** - loading element is an inductor,

Since the loaded loop is coupled with the incoming wave via magnetic field, the equivalent circuit should contain mutual inductance (transformer). One of the possible simplifications of this circuit (consistent with Figure 3-7) is shown in Figure 3-16.

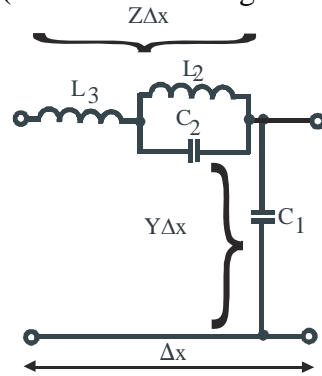


**Figure 3-16** Transmission-line equivalent circuit of MNG (MNZ) metamaterial based on an array of capacitively loaded loops

Probably the most popular inclusion based on a capacitively loaded loop is a split-ring-resonator (SRR). Measured effective permeability of a typical realistic SRR medium is shown in Figure 3-17. It can be seen that the curves for both  $\mu'$  and  $\mu''$  qualitatively agree with the theoretical curve of Lorentz dispersion model. The real part of the permeability becomes negative in a narrow frequency band (7.75 GHz – 7.9 GHz) and reaches a minimal value of  $\sim -0.7$ . This, relatively small value of negative permeability indicates that there was a significant influence on its value by the losses associated with the high current density along the rings in the vicinity of the resonant frequency. The narrow bandwidth and pronounced losses are inherent properties of all metamaterials based on resonant loops. The operating bandwidth (BW) of 5 % and the dispersion bandwidth (DBW) of 1.2% together with a rather bad value of FOM of 1 in an MNG part of the curve, have been estimated from Figure 3-17.

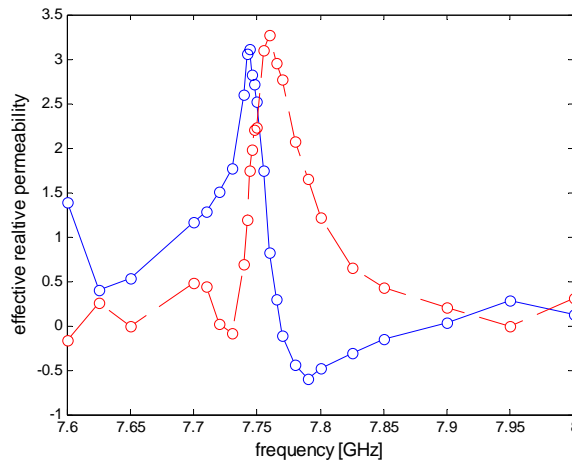


**Figure 3-17** Extracted effective relative permeability of the metamaterial based on SRR inclusions [2], **Solid** – real part, **Dashed** – imaginary part

### 3.4.3. Transmission-line-based metamaterials

In paragraph 3.4.1 it was shown that the propagation of a plane wave in every material (and metamaterial) can be analyzed using a transmission line equivalent circuit (Figure 3-9). It is also possible to think of a reverse approach, in which the transmission line is periodically loaded with lumped elements. If the distance between neighboring elements is a small

fraction of a wavelength this will modify distributed impedance ( $Z$ ) and distributed admittance ( $Y$ ).

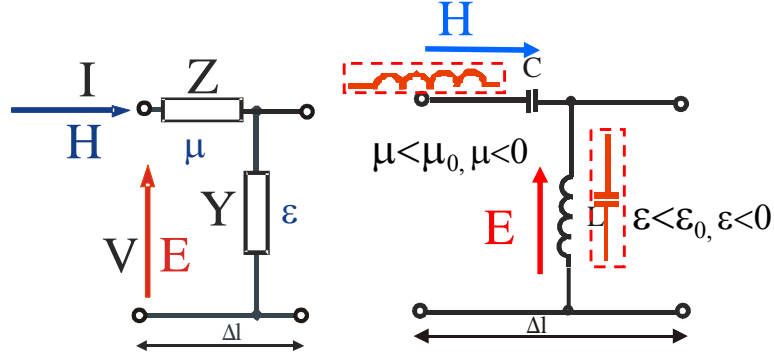


**Figure 3-18** DNG Transmission-line-based metamaterial

In this way, it is possible to *formally* define the equivalent permittivity and permeability for any type of loading elements (or more complicated one-port networks) (Left part of Figure 3-18):

$$Z\Delta x = j\omega\mu_{eff}\Delta x \Rightarrow \mu_{eff} = \frac{Z}{j\omega}, \quad (3.39)$$

$$Y\Delta x = j\omega\epsilon_{eff}\Delta x \Rightarrow \epsilon_{eff} = \frac{Y}{j\omega}. \quad (3.40)$$

Now, one can think of simple swapping of the locations of distributed capacitance and distributed inductance in the transmission line. The equivalent permeability and permittivity of this ‘inverted’ line are given by:

$$\mu_{eff} = \frac{Z}{j\omega} = \frac{-j\frac{1}{\omega C}}{j\omega} = -\frac{1}{\omega^2 C}, \quad (3.41)$$

$$\epsilon_{eff} = \frac{Y}{j\omega} = \frac{-j\frac{1}{\omega L}}{j\omega} = -\frac{1}{\omega^2 L}. \quad (3.42)$$

It can be seen (3.41, 3.42) that both effective permittivity and effective permeability are negative, thus, the structure behaves as 1D DNG metamaterial. This approach of designing metamaterial indeed looks to be very elegant and simple.

However, there are several problems in the interpretation of physic of the achieved results from (3.40, 3.41). At first, the equivalent permittivity and permeability retain negative signs for all the frequencies (please note that (3.41, 3.42) actually obey Drude model with infinite value of plasma frequency). Obviously, this is physically incorrect (in high-frequency limit permittivity and permeability must approach their free-space values). In addition, one cannot identify the elements for resonant energy redistribution, which are needed in order to obtain ‘negative’ and ‘near-zero’ parameters in passive metamaterials. Actually, it seems that the DNG transmission metamaterial, based on swapping locations of distributed inductance and capacitance, does not have resonant elements (LC circuits) at all. This led to the widely accepted opinion that the transmission-line-based metamaterials are of non-resonant nature (as mentioned before, this conclusion *is not correct*).

In order to clear this confusion one should think of energy issue. In Figure 3-18 it is shown that the distributed series impedance  $Z$  is ‘driven’ by current  $I$ , while the distributed shunt admittance  $Y$  is driven by voltage  $V$ . Looking back to an original electromagnetic problem (described by Helmholtz equation) it can be concluded that  $Z$  and  $Y$  are associated with the magnetic and electric fields of the incoming plane wave, respectively. It is clear that in the case of ordinary LC transmission line the distributed series inductance  $L$  is associated with the energy stored in magnetic field. However, in the case of ‘inverted’ DNG line (Right part of Figure 3-18) the distributed series capacitance is ‘driven’ by the magnetic field and the distributed shunt inductance is ‘driven’ by the electric field. It actually means that there is *again* resonant energy distribution from the magnetic field into the electric field (in the case of series distributed capacitance) and from the electric field into the magnetic field (in the case of shunt distributed inductance). Thus, there are again resonant LC circuits, but they are ‘hidden’ in a simplified model of inverted CL line.

From practical point of view, every lumped inductor has parallel parasitic capacitance and every lumped capacitor has series parasitic inductance (for instance, these parasitic elements can be attributed to the element leads). Thus, the more correct equivalent circuit of the transmission-line-based metamaterial should contain a series LC circuit in the series branch and a parallel LC circuit in the shunt branch (these parasitic elements are sketched within dashed rectangles in right part of Figure 3-18). This ‘reconciled’ circuit now shows physically correct behavior that agrees with the experiments. It is known that the DNG operation of every transmission-line-based metamaterial fails at high frequencies, which can be explained easily with explained corrected model. In addition, the new equivalent parameters obey Drude dispersion model (please look at Figure 3-6):

$$\mu_{eff} = \frac{Z}{j\omega} = \frac{j\omega L_{parasitic} - j\frac{1}{\omega C}}{j\omega} = L \left( 1 - \frac{\omega_p^2}{\omega^2} \right), \quad \omega_p = \frac{1}{\sqrt{L_{parasitic} C}}, \quad (3.43)$$

$$\epsilon_{eff} = \frac{Y}{j\omega} = \frac{j\omega C_{parasitic} - j\frac{1}{\omega L}}{j\omega} = C \left( 1 - \frac{\omega_p^2}{\omega^2} \right), \quad \omega_p = \frac{1}{\sqrt{C_{parasitic} L}}. \quad (3.44)$$

The bandwidth and losses of the transmission line-metamaterials are similar to those of wire-based metamaterials (because they use the same dispersion model). Typical well designed transmission-line-based metamaterials have the BW and DBW of approximately 50% and 15%, respectively. Typical value of FOM is 5-10. These good figures are caused by Drude dispersion, but the fundamental bandwidth limit associated with the resonant energy dispersion still does exist.

Explained principle can be extended to all other types NZ or NG of metamaterials. Some typical examples are sketched in Figure 3-19.

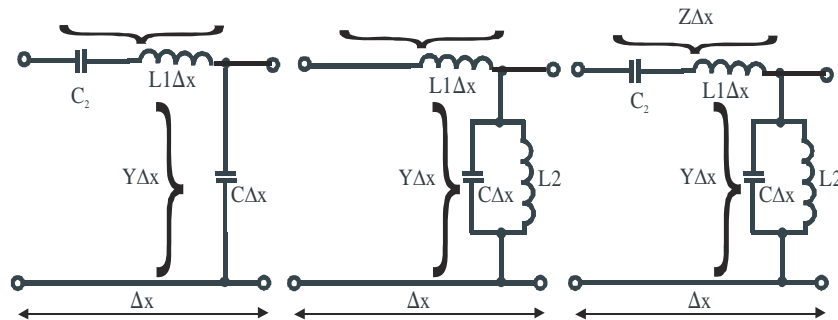


**Figure 3-19** Equivalent circuits of different passive 1D TL-based metamaterials, **Left** – MNG (or MNZ), **Middle** - ENG (or ENZ), **Right**- DNG (or MENZ)



Finally, properties of all discussed passive metamaterials are compared in Table 3-1.

Type of passive MTM		Dispersion model	Typical bandwidth		Typical loss	Mechanism of NG and NZ behavior
			BW	DBW		
Wire medium		Drude	50%	15%	not pronounced (FOM $\approx 10$ )	Resonant energy redistribution caused by energy-dispersion constraints (Foster theorem)
Resonant inclusions	Inductively loaded dipole (loop-wire, CSRR)	Lorentz	5%	1%	pronounced (FOM $\approx 0.5 - 1$ )	
	Capcitively loaded loop (SRR)	Lorentz	5%	1%	pronounced (FOM $\approx 5 - 10$ )	
Transmission-line-based		Drude	50%	15%	not pronounced (FOM $\approx 5 - 10$ )	

**Table 3-1** Comparison of passive metamaterials

### 3.5. Summary

The basic dispersion-bandwidth properties of passive metamaterials have been analyzed in this chapter. The most important issues are summarized below:

- The metamaterial dispersion and bandwidth are the most important criteria in many applications (e.g. in cloaking technology).
- Widely used bandwidth that deals with a frequency band with NG or NZ behavior (BW) is loosely defined and it is inappropriate for applications that rely on precise values of effective parameters (e.g. cloaking). In such a case it is more correct to use 'dispersion bandwidth' (DBW) that deals with the 'flatness' of the dispersion curve. In passive metamaterials, the DBW is always narrower than BW.
- The narrowband operation is caused by the inherent dispersion that occurs in all passive metamaterials (irrespective of their internal structure). The inherent dispersion is a consequence of very fundamental energy-dispersion constraints (or, from circuit-theory point of view, a consequence of Foster theorem).
- These fundamental constraints do not allow existence of the dispersionless 'negative capacitors' and 'negative inductors'.
- The only way of achieving of 'negative' (ENG, MNG) or 'near-zero' (ENZ, MNZ) behavior deals with the resonant energy redistribution between the electric and magnetic fields. This redistribution occurs in all lossless passive metamaterials (irrespective of their internal structure).
- From circuit-theory point of view, the resonant energy redistribution can be achieved by reactive networks, input impedance of which behaves as dispersive 'negative capacitor' or dispersive 'negative inductor'.

Chapter 4 ACTIVE NON-FOSTER METAMATERIAL - THEORETICAL INVESTIGATION

## A concept of active metamaterial - theoretical analysis

### 4.1 Previous work

In the previous chapter it was shown that the realization of ‘negative’ or ‘near-zero’ media implies the use of the resonant devices. The resonant device is a necessity due to inevitable energy redistribution that enables required NG or NZ behavior. This behavior is possible only within a narrow frequency band near the resonance, where the metamaterial is highly dispersive (i.e. the media parameters quickly vary with the frequency). This drawback is a direct consequence of the basic energy-dispersion relations, or (from the circuit theory point of view) a consequence of Foster reactance theorem.

As it is well known, the energy-dispersion constraints and Foster theorem are valid only for passive structures. Thus, if one allows the existence of the active materials (or active inclusions) there will not be any theoretical restrictions on the realized bandwidth.

The idea of the incorporation of active circuits into an artificial material is not new. There had been several theoretical studies about the active inclusions for various potential microwave applications. They included structures with non-linear response and the wide-band active absorbers [22,23,24].

The first paper (to the best of our knowledge) that theoretically discussed a possible use of active non-Foster elements in metamaterials was published in 2001 [25]. This paper analyzed the equations for polarizability of metamaterials based on (previously discussed) short loaded dipoles and small loaded loops. It was shown analytically that a loading of a short dipole with a *negative capacitance* (instead of ordinary, positive inductance) should lead to the wideband dispersionless ENG behavior. Similarly, the loading of a small loop with a *negative inductance* (instead of ordinary, positive capacitance) should lead to the wideband dispersionless MNG behavior. It is important to stress that, in this case, the bandwidth would be limited only by the bandwidth of realized non-Foster element. Thus, one might expect multi-octave bandwidth, which would be a significant progress in the metamaterial field. The authors in [25] also proposed active ‘impedance sheets’ (i.e. very thin metamaterials) with ENG or MNG properties. In the conclusion, it was noted that required negative non-Foster elements appear to be feasible at lower end of RF range using available technology (operational amplifiers). However, the subsequent theoretical study [26] revealed that the dispersionless ENG and MNG metamaterials based on negative non-Foster elements are inherently unstable. Due to this serious drawback, they appear to be not feasible in practice.

It is in agreement with a commonly accepted rule that a sum of the capacitances (or inductances) along a closed mesh should be a positive number for stable operation. Following original idea from [25] the authors in [27] theoretically investigated stability of an array of small loops loaded with non-Foster reactive elements. Surprisingly, it was found that such a metamaterial can be stable, but only if the array is infinitely large. In this case (that is probably non-practical), the predicted MNG behavior was not entirely dispersionless, but the estimated bandwidth was significantly larger than a bandwidth of passive metamaterials.

There are a few other studies that deal with the incorporation of active devices into the metamaterial structure. A remarkable experimental study [27] reported low losses metamaterial based on the use of ‘sensing and intervening’ active structure. The ‘sensing’ (receiving) loop was connected to the amplifier that modified the signal (both the amplitude and phase). The amplifier output was connected to the ‘intervening’ (transmitting) loop that radiated the signal in backward direction. It was shown possible to obtain a metamaterial with low loss within the bandwidth (BW) of 25%. The drawback of this approach is that needed gain of an amplifier was pretty high (around 30 dB), which seems to be impractical. There is also an approach based on anomalous dispersion [18,19], i.e. based on a change of the slope of the dispersion curve in the vicinity of the absorption line (or a gain line). Briefly, one (drastically) decreases the  $Q$  factor of some resonator (usually a simple  $LC$  circuit). This introduces anomalous dispersion with broadband behavior, but at the cost of huge losses (typically about 20 dB per unit cell). In order to compensate for this loss, the gain stage is added after the resonator (a gain is usually achieved by the use of negative resistance amplifier). The obvious drawback of this approach is a poor noise figure of the system. However, this approach can generate negative group delay (and negative group velocity) that can be useful for delay compensation in communication systems. The best achieved bandwidth (BW) with negative delay was approximately 50% [19].

This brief review of proposed active metamaterial structures shows that the approach based on non-Foster elements offers potentially the largest (multi-octave) bandwidth. However, theoretical investigation conducted so far predicted unstable operation of these metamaterials. This is a very serious obstacle, which was probably the reason that no experimental results have been published so far.

In the subsequent sections we propose a novel approach that allows construction of a stable broadband non-Foster-elements-based ENZ or MNZ metamaterials for cloaking applications. This approach uses the periodic loading of a transmission line with negative capacitors or negative inductors.

## **4.2 A novel concept of ultra-broadband ENZ or MNZ active metamaterial**

In this section we propose a novel idea of modifying the dispersion of one of the reactive elements (either a capacitor or an inductor) in the unit cell of a transmission-line-based metamaterial by adding a ‘negative’ element. We show that this approach lead to the broadband dispersionless ENZ or MNZ behavior.

#### 4.2.1. Inclusion of $CC_{\text{neg}}$ circuit into transmission line – Broadband active 1D ENZ metamaterial

Let us analyze a typical one-dimensional (1D) implementation of ENZ (or ENG) metamaterial based on a transmission line periodically loaded with the lumped inductances (Fig. 2 (A)).

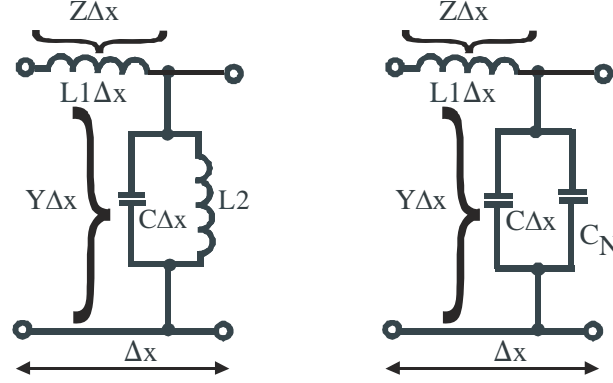


**Figure 4-1** Left - Transmission-line model of 1D passive ENG (or ENZ) metamaterial, **Right** Proposed active ENZ metamaterial

For instance, this equivalent circuit describes a well-known wire medium analyzed in paragraph 3.4.1. The resonator in the left part of Figure 4-1 is actually a tank circuit formed by the line shunt capacitance  $C\Delta x$  ( $C$  being the distributed capacitance and  $\Delta x$  being the line segment length) and the lumped inductor  $L_2$ .

If the length of the transmission line segment ( $\Delta x$ ) is a small fraction of the wavelength, the distributed shunt admittance is given by:

$$Y = j\omega C + \frac{1}{j\omega L_2 \Delta x} = j\omega \left( C - \frac{1}{\omega^2 L_2 \Delta x} \right). \quad (4.1)$$

Here,  $C$  stands for the distributed capacitance of the transmission line, while  $L_2$  is the loading lumped inductance. By applying a basic relation for distributed shunt admittance  $Y = j\omega\epsilon$ , one immediately derives the equivalent relative permittivity:

$$\epsilon_r(\omega) = \left[ \frac{1}{\epsilon_0} \left( C - \frac{1}{\omega^2 L_2 \Delta x} \right) \right]. \quad (4.2)$$

The permittivity (4.2) is, obviously, a nonlinear function of frequency, and is lower than one when the quantity in the parentheses is smaller than  $\epsilon_0$ . The energy stored in the capacitor is lower than the energy that would be stored in the electric field in vacuum within the same volume. As explained before, a fraction of the ‘electric’ energy from the capacitor is converted into the ‘magnetic’ energy in the inductor, since the inductor is driven by the voltage (the electric field). This happens only within a narrow band above the resonant frequency of a parallel tank circuit (Left part of Figure 4-1).

Is it possible to go around the basic dispersion constraints (3.7) and construct a broadband dispersionless material? From circuit-theory point of view, the dispersion actually

happens due to the different frequency behavior of the capacitive susceptance ( $+j\omega C$ ) compared to the inductive susceptance ( $-j/\omega L$ ) (4.2).

Now let us introduce a negative capacitance  $C_n < 0$  and a negative inductance  $L_n < 0$ . The susceptances of these fictitious ‘negative’ elements read:

$$B_{L_n} = -j \frac{1}{\omega L_n} = +j \frac{1}{\omega |L_n|}, \quad B_{C_n} = j\omega C_n = -j\omega |C_n|. \quad (4.3)$$

The dispersion curves of negative elements are inverse to their counterparts of the ordinary elements (Figure 4-2)

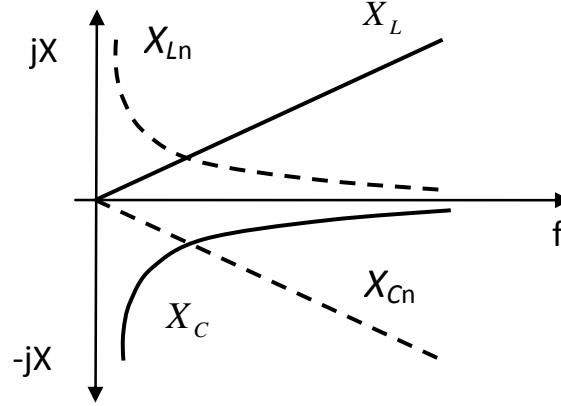


**Figure 4-2** Reactance of positive (solid line) and negative (dashed line) reactive elements

Now, one may think of a periodic loading of a transmission line with lumped negative capacitors  $C_n$ . The admittance and the equivalent permittivity of this ‘ $CC_n$  tank circuit’ (Right part of Figure 4-1) read as:

$$Y = j\omega C + j\omega \frac{C_n}{\Delta x} = j\omega \left( C - \frac{|C_n|}{\Delta x} \right). \quad (4.4)$$

$$\varepsilon_r(\omega) = \left[ \frac{1}{\varepsilon_0} \left( C - \frac{|C_n|}{\Delta x} \right) \right]. \quad (4.5)$$

Contrary to the case of a transmission line loaded with positive inductances (4.1), one finds that this new equivalent permittivity (4.5) is *not dependent on frequency at all*. Thus, if one chooses  $(|C_n|/\Delta x) < C$ , he will get an entirely dispersionless ENZ metamaterial [29]. In order to understand this counter-intuitive behavior one should briefly analyze the physics of non-Foster element (more detailed analysis will be presented in paragraph 4.3).

The susceptances in (4.3) are functions that monotonically decrease with frequency, so the Foster theorem is obviously violated. A counter-intuitive fact that the average energy is negative ( $W < 0$  in (3.5)) indicates that the ‘negative capacitor’ and the ‘negative inductor’ must contain active elements. They can be viewed as the ‘inverted’ ordinary elements. Probably the simplest principle of this inversion is shown in Figure 4-3. The (grounded) impedance that should be inverted ( $Z$ ) is shown in the left part of the figure. In order to invert the impedance, one should swap the sign of either the voltage across the element ( $V$ ) or the

sign of the current flowing through it ( $I$ ). This can be achieved by inserting the additional 'dependent' voltage source of amplitude  $2V$  in series with impedance  $Z$  (the middle part of Figure 4-3). The voltage drop across the impedance ( $\Delta V$ ) is now given by:

$$\Delta V = V - 2V = -V. \quad (4.6)$$

This causes the change of the sign of current  $I$ :

$$I = \frac{\Delta V}{Z} = -\frac{V}{Z}. \quad (4.7)$$

Thus, the current  $I$  now flows outward from the circuit. This causes the inversion of the impedance  $Z_{in}$  (seen from the input terminals):

$$Z_{in} = \frac{V}{-\frac{V}{Z}} = -Z. \quad (4.8)$$

A possible realization of the dependent source by an ideal amplifier with voltage gain  $A=+2$  is shown in the right part of Figure 4-3.

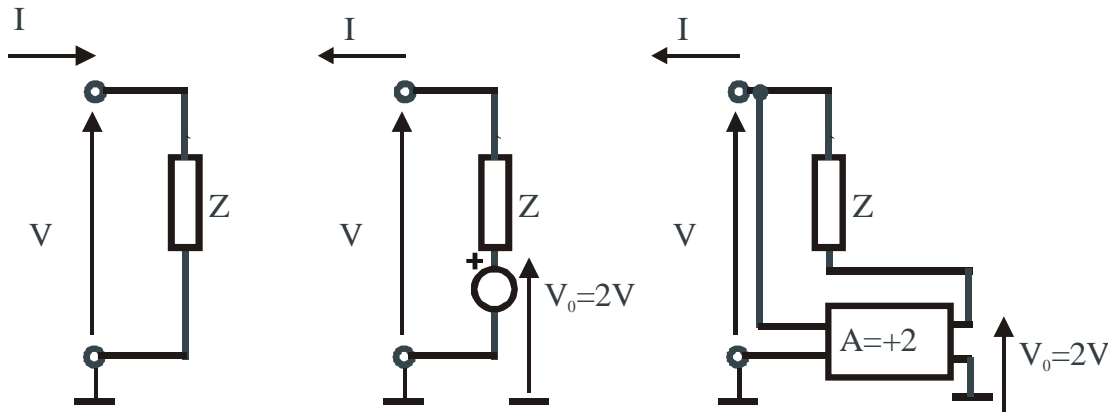


**Figure 4-3** An example of operating principle of negative non-Foster impedance

Now it is possible to explain the difference between an ordinary  $LC$  tank circuit and an active  $CC_n$  circuit.

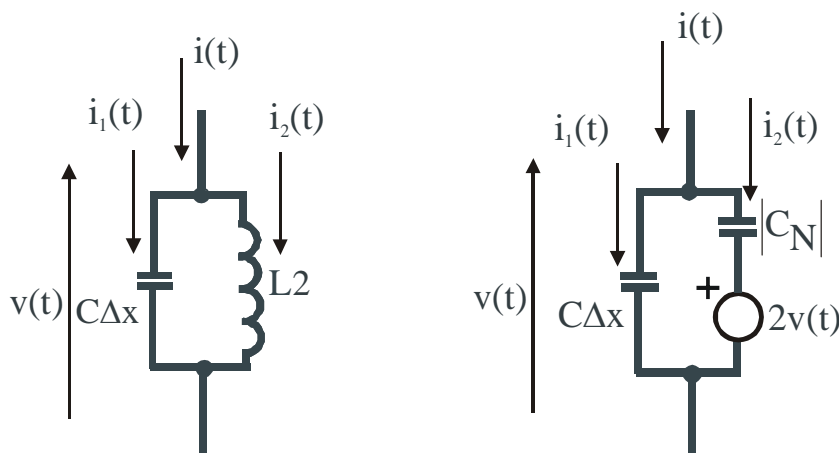


**Figure 4-4** Comparison between LC circuit and  $CC_n$  circuit

The ordinary LC circuit driven by monochromatic signal  $v(t)=V_0\cos(\omega t)$  is depicted in the left part of Figure 4-4. The currents in the circuits are given by simple equations:

$$i_1(t) = C\Delta x \frac{d[v(t)]}{dt} = -V_0\omega C\Delta x \sin(\omega t), \quad (4.9)$$

$$i_2(t) = \frac{1}{L} \int v(t) dt = \frac{V_0}{\omega L} \sin(\omega t). \quad (4.10)$$

$$i(t) = i_1(t) + i_2(t) = -V_0\omega C\Delta x \sin(\omega t) + \frac{V_0}{\omega L} \sin(\omega t) = V_0\omega C \left(1 - \frac{1}{\omega^2 L}\right) \sin(\omega t). \quad (4.11)$$

Associated (instantaneous) reactive power quantities are given by:

$$p_1(t) = v(t)i_1(t) = -\frac{V_0^2\omega C}{4} \sin(2\omega t), \quad (4.12)$$

$$p_2(t) = v(t)i_2(t) = \frac{V_0^2}{2\omega L} \sin(2\omega t), \quad (4.13)$$

$$p(t) = v(t)[i_1(t) + i_2(t)] = -\frac{V_0^2\omega C}{2} \sin(2\omega t) + \frac{V_0^2}{2\omega L} \sin(2\omega t) = -\frac{V_0^2}{2} \left(\omega C + \frac{1}{\omega L}\right) \sin(2\omega t). \quad (4.14)$$

Equation (4.14) again highlights the previously discussed phenomenon on resonant energy redistribution. The instantaneous reactive power delivered from the source is divided into two, generally unequal, parts: the reactive capacitive power and the reactive inductive power. Looking from the source side, this can be interpreted as the reactive capacitive power on the equivalent dispersive negative capacitor  $C_{eff}$  that obeys Drude dispersion model:

$$p(t) = p_1(t) + p_2(t) = -\frac{V_0^2}{2} \left(\omega C - \frac{1}{\omega L}\right) \sin(2\omega t) = -\frac{V_0^2\omega C_{eff}}{2} \sin(2\omega t),$$

$$C_{eff} = C \left(1 - \frac{1}{\omega^2 LC}\right) = C \left(1 - \frac{\omega_p^2}{\omega^2}\right), \quad \omega_p = \frac{1}{\sqrt{LC}}. \quad (4.15)$$

At the resonant frequency  $\omega_p$  (plasma frequency) reactive power is delivered in equal parts to the capacitor and inductor. Since there is no current  $i(t)$  flowing from the external source the energy is only circulating between reactive elements.

If an inductor is replaced with an active negative non-Foster capacitor (modeled as a dependent source in the right part of Figure 4-4), the situation becomes fundamentally different. Deriving again the currents and reactive power quantities one gets:



$$i_1(t) = C\Delta x \frac{d[v(t)]}{dt} = -V_0\omega C\Delta x \sin(\omega t), \quad (4.16)$$

$$i_2(t) = |C_n| \frac{d[-v(t)]}{dt} = V_0\omega |C_n| \sin(\omega t). \quad (4.17)$$

$$i(t) = i_1(t) + i_2(t) = -V_0\omega C\Delta x \sin(\omega t) + V_0\omega |C_n| \sin(\omega t) = V_0\omega (C\Delta x - |C_n|) \sin(\omega t). \quad (4.18)$$

$$p_1(t) = v_1(t)i_1(t) = -\frac{V_0^2\omega C}{2} \sin(2\omega t), \quad (4.19)$$

$$p_2(t) = v_2(t)i_2(t) = -v(t)i_2(t) = \frac{V_0^2\omega |C_n|}{2} \sin(2\omega t), \quad (4.20)$$

$$\begin{aligned} p(t) &= v(t)[i_1(t) + i_2(t)] = \\ &= V_0 \cos(\omega t) (-V_0\omega C\Delta x \sin(\omega t) + V_0\omega |C_n| \sin(\omega t)) = \\ &= -\frac{V_0^2}{2} \omega (C - |C_n|) \sin(2\omega t). \end{aligned} \quad (4.21)$$

It can be seen that a negative capacitor behaves as an inductor, but with the frequency characteristic equal to that of an *ordinary capacitor*. Looking from the external source side one can think of the effective capacitor, capacitance of which can be arbitrarily small (and even negative):

$$C_{eff} = C - |C_n|. \quad (4.22)$$

One should be very cautious in the interpretation of (4.21). *It does not* mean that the reactive power from the source is simply delivered to two capacitors ( $C$  and  $|C_n|$ ). One should not forget that there is a second source of energy in the network. That (dependent) source assures a voltage at  $|C_n|$  that is, at any instant of time, exactly opposite to  $v(t)$ . This source delivers reactive power given by:

$$p'(t) = 2v(t)i_2(t) = 2V_0 \cos(\omega t) |C_n| V_0 \omega \sin(\omega t) = V_0^2 |C_n| \sin(2\omega t). \quad (4.23)$$

Of course, this energy actually comes from the DC source that acts as a power supply of an electronic circuit that behaves as the dependent source. Therefore, the capacitor  $C$  is actually charged and discharged from two sources: the external source and the depending source. In addition, the amount of charge transferred from the external source is lower than the amount of charge that would be transferred from the external source if there were only the capacitor  $C$  present in the circuit. Since the net amount of charge is lower, the effective capacitance looked from the external source is lower than  $C$ . Thus, one may say that the negative capacitor acts as the additional energy source/sink lowering the net 'electric' energy.

Above discussion shows that the  $CC_n$  circuit is not a tank circuit at all. This is just a capacitor, the capacitance of which can have arbitrary low value. This is the reason of dispersionless operation of proposed ENZ active material.

Negative ‘non-Foster’ networks are not new at all and they are based on Negative Impedance Converter (NIC), originally introduced back in the 1950’s [14]. Although this idea is indeed old, there are only a few papers [31-38] in the open literature that report successful practical implementations of negative capacitor or negative inductor in RF and microwave range. The main problem is the inherent instability caused by the fact that all NIC circuits employ amplifiers with positive feedback.

Our investigation (explained in details in chapter 4.3.3) have found that the choice of method for assessing the stability issue is very important, as well. Traditionally, RF and microwave engineers analyze the stability in the frequency domain with the help of ‘stability factors’ [17], based on the input reflection coefficient of a circuit. In addition, almost all standard RF and microwave circuit simulators use these stability factors. However, it is very often neglected that all stability factors based on the reflection coefficient presume that the Nyquist stability criterion is *a priori* satisfied, i.e. that the transfer function has no poles in the right half-plane. If one neglects this fact, it is possible that the analysis of the stability factor predicts stable operation even for a circuit that is inherently unstable. For instance, the modulus of the reflection coefficient of an ideal negative capacitance is one, as is the modulus of an ordinary positive capacitance. Looking at this result, one could (wrongly) conclude that a pure negative capacitor is a stable device. However, a very simple and intuitive transient analysis presented in [26] clearly shows an unbounded growth of voltage across the negative capacitance, i.e. instability. Simply stated, in order to assure stable operation in active metamaterial sketched in the right part of Figure 4-1), the net loop capacitance (overall capacitance along a closed  $CC_n$  mesh in a circuit) should always be positive (thus  $C\Delta x > |C_n|$ ). Therefore, it appears that is impossible to construct broadband non-Foster ‘negative’ metamaterials (ENG, MNG, DNG) (at least using simple one-port non-Foster networks). However, ENZ and MNZ metamaterials (needed in cloaking applications) can be designed to be stable (because they need only  $0 < \epsilon_r < 1$  or  $0 < \mu_r < 1$ , which significantly relaxes the stability problem [29]).

#### 4.2.2. Inclusion of $LL_{neg}$ circuit into transmission line – Broadband active 1D MNZ metamaterial

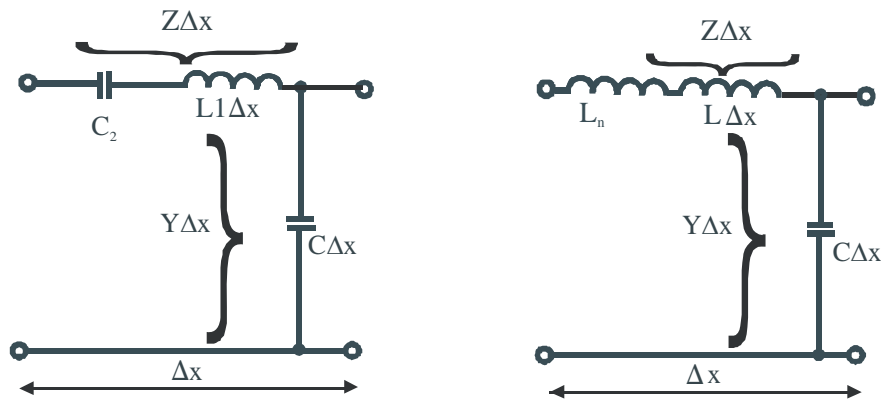


**Figure 4-5 Left** - Transmission-line model of 1D passive MNZ metamaterial, **Right** - Proposed active MNZ metamaterial

It is now straightforward to extend the proposed principle to the design of active MNZ metamaterial. Classical passive MNZ transmission-line-based metamaterial (Left part of Figure 4-5) employs periodical loading with series lumped capacitors. . Thus, each differential distributed inductance  $L_1$  is connected to the additional lumped capacitor  $C_2$  forming a resonant  $LC$  circuit. Following the previous analysis, one directly derives the equivalent effective permeability:

$$\begin{aligned}\mu_{r_{eff}} &= \frac{1}{\mu_0} \frac{Z}{j\omega} = \frac{1}{\mu_0} \frac{j\omega L_1 \Delta x - j \frac{1}{\omega C_2}}{j\omega} = \frac{1}{\mu_0} \frac{j\omega \left( L_1 \Delta x - \frac{1}{\omega^2 C_2} \right)}{j\omega} \\ &= \frac{1}{\mu_0} L_1 \Delta x \left( 1 - \frac{\omega_p^2}{\omega^2} \right), \quad \omega_p = \frac{1}{\sqrt{L_1 \Delta x C_2}}.\end{aligned}\quad (4.24)$$

As in the previous cases, the resonant energy redistribution occurs within a series  $LC$  circuit. The instantaneous reactive power delivered from the source to the series branch is divided into two, generally unequal parts: the reactive capacitive power and the reactive inductive power. Looking from the source side, this can be interpreted as the reactive inductive power on the equivalent dispersive negative inductor  $L_{eff}$  that obeys Drude dispersion model:

$$L_{eff} = L_1 \Delta x \left( 1 - \frac{1}{\omega^2 L_1 \Delta x C_2} \right) = L_1 \Delta x \left( 1 - \frac{\omega_p^2}{\omega^2} \right), \quad \omega_p = \frac{1}{\sqrt{L_1 \Delta x C_2}}. \quad (4.25)$$

At the resonant frequency  $\omega_p$  (plasma frequency) the reactive power is delivered in equal amounts to the capacitor and the inductor. Thus, there is no voltage across series  $LC$  circuit and it behaves as a short circuit.

The replacement of the lumped capacitor  $C_2$  with the negative non-Foster inductor  $L_n$  leads to a broadband dispersionless behavior (Right part of Figure 4-5):

$$\begin{aligned}\mu_{r_{eff}} &= \frac{1}{\mu_0} \frac{Z}{j\omega} = \frac{1}{\mu_0} \frac{j\omega L_1 \Delta x - j\omega |L_n|}{j\omega} = \frac{1}{\mu_0} \frac{j\omega (L_1 \Delta x - |L_n|)}{j\omega} \\ &= \frac{1}{\mu_0} (L_1 \Delta x - |L_n|).\end{aligned}\quad (4.26)$$

Physical explanation is very similar to the case with negative capacitor. The additional reactive energy comes from the DC source that acts as a power supply of an electronic circuit that behaves as the negative inductor. Therefore, the magnetic energy in inductor  $L_1 \Delta x$  is growing and decaying due to two sources: the external source and the dependent source (within the negative inductor). Due to this, the effective inductance looked from the external source is lower than  $L_1 \Delta x$ . Actually, the negative inductor acts as the additional energy source/ sink lowering the net ‘magnetic’ energy. It can be concluded that the  $LL_n$  circuit is not a tank circuit at all (in an ordinary sense). This is just an inductor with arbitrary low value of the inductance. This is the reason of dispersionless operation of proposed MNZ active material.

Finally, it is possible to combine the principles of proposed active ENZ and MNZ metamaterials into the dispersionless active MENZ metamaterial.

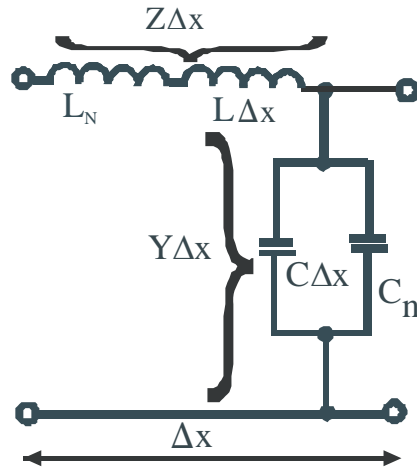


**Figure 4-6** Broadband active non-Foster MENZ metamaterial

From practical point of view, both active MNZ and MENZ metamaterials are slightly more difficult for realization comparing to an active ENZ metamaterial because they require ‘floating’ non-Foster elements.

#### 4.2.3. Extension to Broadband active 2D metamaterial

Several applications of ‘negative’ and ‘near-zero’ metamaterials require 2D designs. Moreover, some of these metamaterials should be anisotropic (a typical example is transformation electromagnetic cloak). The extension of proposed approaches in 2D (both the isotropic and anisotropic cases) is, at least in principle, straightforward. Some basic ideas are sketched in Figure 4-7). The circuit in the upper part of the figure depicts a unit cell of 2D ENZ active metamaterial. It has two orthogonal branches, by inductances of which one can adjust needed values of (positive) permeability in x and y directions. The shunt susceptance contains a negative capacitor (connected in parallel with a distributed capacitance of the transmission line assuring the ENZ behavior). Thus, the permeability and permittivity tensors of this metamaterial read as:

$$\mu_{r\text{eff}} = \begin{bmatrix} \mu_{rx} & 1 \\ 1 & \mu_{ry} \end{bmatrix}, \quad \mu_{rx} \geq 1, \mu_{ry} \geq 1, \quad \varepsilon_{r\text{eff}} = \begin{bmatrix} \varepsilon_r & 1 \\ 1 & \varepsilon_r \end{bmatrix}, \quad 0 \leq \varepsilon_r \geq 1. \quad (4.27)$$

Middle part of Figure 4-7 shows an anisotropic MNZ metamaterial with (in a general case) unequal negative inductances in orthogonal branches. The permeability and permittivity tensors of this metamaterial are given by:

$$\mu_{r\text{eff}} = \begin{bmatrix} \mu_{rx} & 1 \\ 1 & \mu_{ry} \end{bmatrix}, \quad 0 \leq \mu_{rx} \geq 1, \quad 0 \leq \mu_{ry} \geq 1, \quad \varepsilon_{r\text{eff}} = \begin{bmatrix} \varepsilon_r & 1 \\ 1 & \varepsilon_r \end{bmatrix}, \quad \varepsilon_r \geq 1. \quad (4.28)$$

Finally, the most general anisotropic 2D active broadband MENZ metamaterial is shown in the lower part of Figure 4-7. The constitutive tensors of this metamaterial are:

$$\mu_{r\text{eff}} = \begin{bmatrix} \mu_{rx} & 1 \\ 1 & \mu_{ry} \end{bmatrix}, \quad 0 \leq \mu_{rx} \geq 1, \quad 0 \leq \mu_{ry} \geq 1, \quad \varepsilon_{r\text{eff}} = \begin{bmatrix} \varepsilon_r & 1 \\ 1 & \varepsilon_r \end{bmatrix}, \quad 0 \leq \varepsilon_r \geq 1. \quad (4.29)$$

The isotropic versions of above active metamaterials are simply constructed by selecting identical values of the impedances in x and y branches.

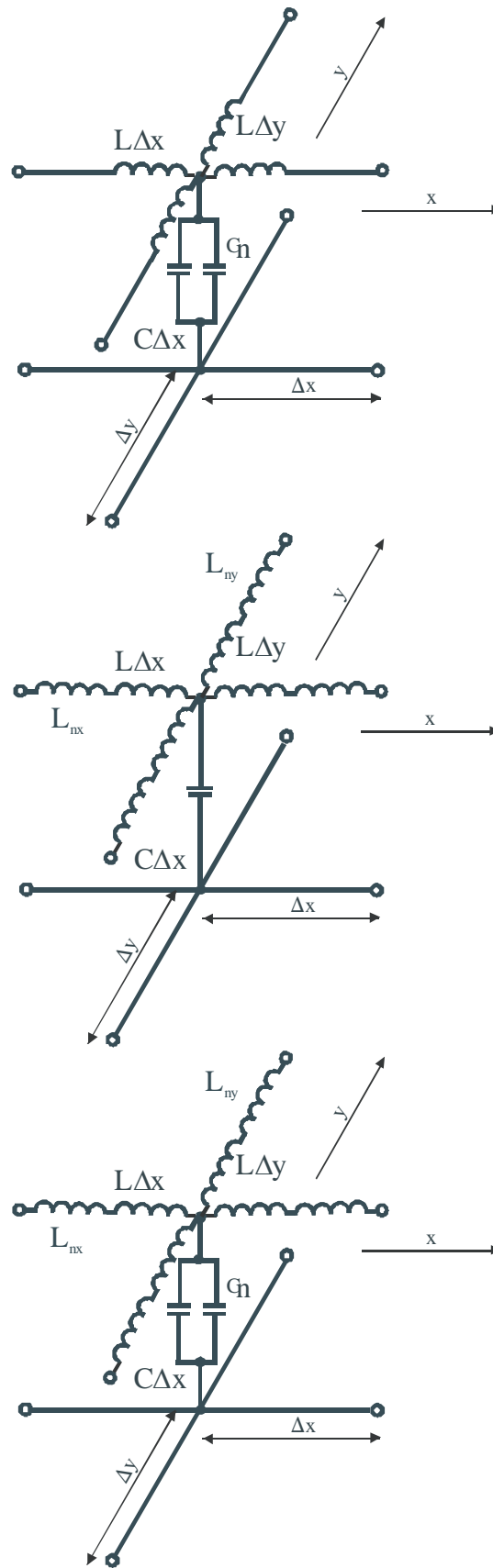


**Figure 4-7** Examples of proposed 2D anisotropic active metamaterials, **Upper - ENZ, Middle - MNZ, Lower - MENZ**

### 4.3 Stability analysis of non-Foster negative reactance elements

#### 4.3.1. Introduction

A numerous research efforts concerning potential application of non-Foster elements have been put in broad-band matching of small antennas [30-45]. The main idea is to use negative capacitors and negative inductors to compensate for the reactive part of the input impedance of a small antenna and remove the frequency dependent behavior of the radiating resistance.

In majority of these studies, the stability was recognized as the main problem in practical realization. However, the stability issue is quite often (incorrectly) solely attributed to the imperfections of the applied technology (for instance, to the occurrence of the parasitic capacitances). Some studies even concluded that the experimental verification of proposed design would have not failed if the better technology had been available. Unfortunately, this conclusion is incorrect.

Actually there are two distinct problems in stability issue: the stability of the electronic circuit used for achieving required negative behavior (it is primarily related to the imperfections of used elements and available technology) and the stability of the whole circuit that contains a non-Foster element (it is primarily related to basic physics of negative elements). In other words, the stability depends not only on the non-Foster elements but also on the topology of the external loading circuit. Even if one had ideal negative elements, many proposed circuits would never be stable due to chosen topology of the external circuit. This is extremely important, but indeed widely overlooked issue.

Stability of electronic circuits that emulate negative elements has been treated in the literature in some details, both on the theoretical and technological levels [34]. Nevertheless, there is certainly much work that should be done, particularly in microwave range. On the contrary, the basic issue of the stability of the circuits containing (even ideal) negative elements has been just touched so far [26, 46]. It is important to stress one again that the choice of a method for assessing the stability issue is very important and some traditional frequency-domain methods (e.g. evaluation of Rollet factor) give wrong predictions. It happens because every non-Foster network does not satisfy the Nyquist stability criterion. i.e. its transfer function has poles either on the imaginary axis or in the right half-plane.

Therefore, in this section, we analyze the basic physics of some circuits that contain ideal negative elements. All these circuits are also simulated using a standard circuit simulator [63] in order to cross-check the developed theory. The examples are selected in a way that mimics typical scenarios in proposed active metamaterials. In addition, a negative capacitor has been chosen as a basic element for the analysis. It was done because the obtained results can be used for the intended design of the experimental demonstrator of active broadband ENZ metamaterial. By applying duality, it is straightforward to extend the results to the circuits that contain negative inductors (MNZ metamaterials).

#### 4.3.2. Charging/discharging of a positive/negative capacitor and occurrence of the instabilities

Let us start with the analysis of a very simple circuit (Figure 4-8) that contains the DC source, the resistor  $R$  and the capacitor  $C$  that can be either positive ( $C > 0$ ) or negative ( $C < 0$ ). It is an easy exercise to derive the current in the circuit from KVL:

$$\left. \begin{aligned} V_0 &= i(t) \cdot R + V_c(t) \\ V_c(t) &= \frac{1}{C} \int_0^t i(\tau) d\tau \end{aligned} \right\} \xrightarrow{\frac{\partial}{\partial t}} R \cdot \frac{\partial i(t)}{\partial t} + \frac{1}{C} i(t) = 0 \Rightarrow i(t) = I_0 \cdot e^{-\frac{1}{R \cdot C} t} = \frac{V_0}{R} e^{-\frac{1}{R \cdot C} t} \quad (4.30)$$

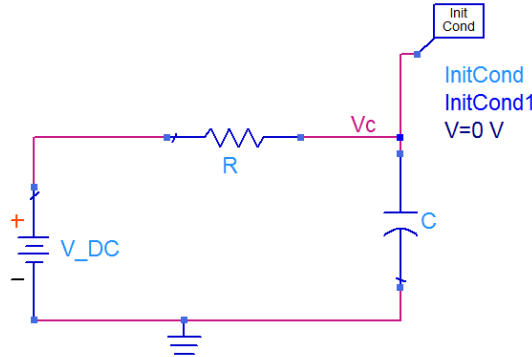


**Figure 4-8** Charging of positive/negative capacitor

From (4.2) one finds a voltage across the capacitor  $C$ :

$$V_c(t) = V_0 - i(t) \cdot R = V_0 \cdot \left( 1 - e^{-\frac{1}{R \cdot C} t} \right) \quad (4.31)$$

If  $C > 0$  the voltage shows well-known exponential growth indicating the charging process (left part of Figure 4-9). However, if one allows a negative value of the capacitance ( $C < 0$ ), the time constant  $\tau = RC$  becomes a negative number. In such a case, there is unbounded exponential growth of the (negative) voltage across  $C$ . i.e. the circuit is *unstable*. As time approaches infinity, the voltage across the capacitor would also approach infinite value. Obviously, this is not physical since the stored energy would approach infinite value. In practice, the voltage will grow to the value limited by the DC power supply of the electronic circuit that emulates the negative capacitor.

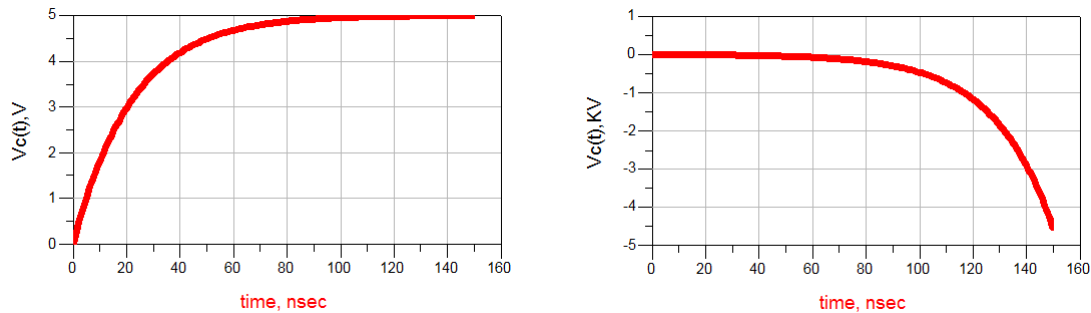


**Figure 4-9** Charging of positive/negative capacitor. **Left:**  $C > 0$ , **Right:**  $C < 0$

Even more striking counter-intuitive behavior occurs during the discharging process (Figure 4-10). The analyzed circuit consists of capacitor  $C$ , resistor  $R$  and a switch. It is assumed that the capacitor was initially charged to voltage  $V_0$ . The switch closes at  $t=0$ . Applying KVL one derives the differential equation with a well known solution:

$$v(t) + CR \frac{dv(t)}{dt} = 0, \quad \Rightarrow v(t) = v(0) e^{-\frac{t}{RC}} = V_0 e^{-\frac{t}{RC}}. \quad (4.32)$$

If the capacitor  $C$  is of ordinary (positive) type ( $C > 0$ ), the time constant  $\tau = RC$  is a positive number and the voltage decays exponentially showing ordinary discharging process. However, if  $C < 0$ , the time constant  $\tau = RC$  becomes a negative number and there is again unbounded exponential growth of the voltage across the capacitor  $C$ . It is not easy to interpret the physics of this counter-intuitive behavior. In [26] it was mentioned that the negative capacitor actually acts as 'the energy attractor' that attracts free electrons from the conductors and charges itself. However, there is no device that can store infinite amount of energy. This confusion occurs due to the assumption that the ideal negative capacitor is entirely dispersionless, which is in contradiction with causality.

From practical point of view, electronic elements used in construction of negative capacitor always have some maximal operating frequency. Thus, every realistic negative capacitor must be band-limited i.e. it must be (even slightly) dispersive and, above some frequency it exhibits positive capacitance. In addition, every realistic electronic circuit that emulates negative capacitor has a DC source with finite amount of energy. The parameters of the DC source will limit maximum value of the exponential voltage growth. However, this does not mean that the realistic negative capacitor will be stable. The voltage will grow until the DC power supply level is reached and then, the circuit will start to oscillate due to its inherent positive feedback.

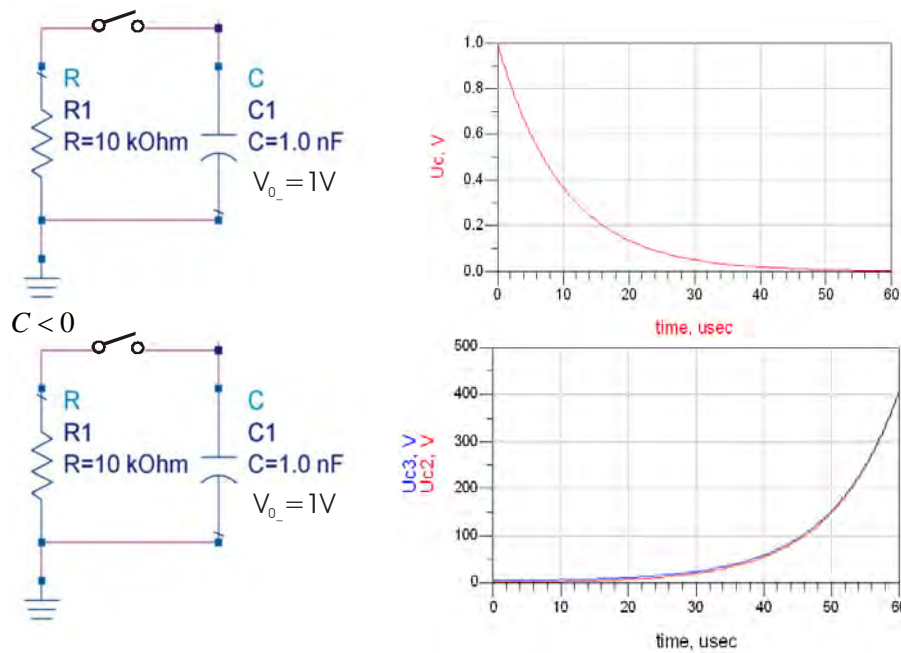


**Figure 4-10** Discharging of positive/negative capacitor. **Upper:**  $C > 0$ , **Lower:**  $C < 0$

#### 4.3.3. Positive/negative parallel LC tanks – natural response

In this section the behavior of a generalized version of a  $LC$  tank, in which both positive and negative values of capacitance are allowed, is analyzed. At first, both the natural response and stability of the generalized  $LC$  tank are discussed. In subsequent discussion, the behavior of the driven circuit is studied.

A simple  $LC$  circuit [46] is used for the analysis of the natural response. It comprises an initially charged ( $V_0 = 5V$ ) capacitor  $C$ . Using a switch, the capacitor is (at  $t = t_0$ ) abruptly connected in series to an inductor  $L$ . At that moment, there is no energy stored in the inductor (there is no current), while the energy stored in the capacitor is given by the familiar equation:



$$W_C = \frac{1}{2} \cdot C \cdot V_0^2$$

$$W_L = 0$$
(4.33)

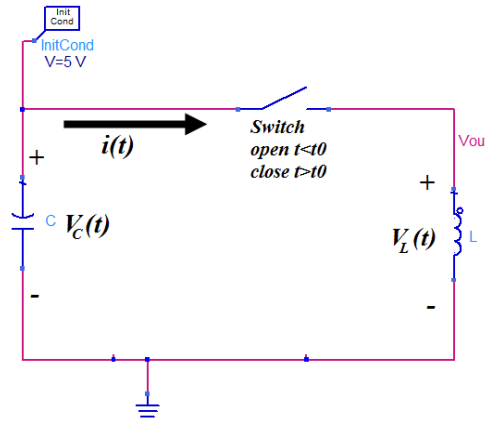


**Figure 4-11** Generalized LC tank circuit

A simple analysis of the circuit in Figure 4-11 results with a second-order differential equation::

$$\left. \begin{aligned} V(t) &= L \cdot \frac{\partial i(t)}{\partial t} \\ i(t) &= -C \cdot \frac{\partial V(t)}{\partial t} \end{aligned} \right\} i(t) = -C \cdot L \cdot \frac{\partial^2 i(t)}{\partial t^2} \Rightarrow \frac{\partial^2 i(t)}{\partial t^2} + \frac{1}{LC} \cdot i(t) = 0.$$
(4.34)

The solution of this equation is found from the roots of a characteristic polynomial:

$$s^2 + \frac{1}{LC} = 0 \Rightarrow \begin{cases} s_1 = j \cdot \frac{1}{\sqrt{LC}} \\ s_2 = -j \cdot \frac{1}{\sqrt{LC}} \end{cases} \Rightarrow i(t) = A \cdot \cos\left(\frac{1}{\sqrt{LC}} \cdot t\right) + B \cdot \sin\left(\frac{1}{\sqrt{LC}} \cdot t\right).$$
(4.35)

It is immediately seen from (4.35) that if both inductance and capacitance are *either positive or negative*, the roots are purely imaginary. In that case, the current will have a simple sinusoidal waveform with a fundamental frequency of:

$$\omega_0 = \frac{1}{\sqrt{LC}}.$$
(4.36)

This stable solution with a sinusoidal waveform is certainly familiar and expected. However, it is quite surprising that a *LC* circuit with negative inductor and negative capacitor is stable, as well.

On the other hand, if an inductor and a capacitor have opposite signs, the roots of a characteristic polynomial will be real numbers with the opposite signs, as well. In that case, the positive real root will lead to unstable exponential solutions. These stability criteria are summarized in Table 4-1

sign of L	sign of C	Stability
+	+	Stable
-	+	Unstable
+	-	Unstable
-	-	Stable

**Table 4-1** Stability criteria for generalized positive/negative LC tank circuit

The constants A and B that appear in stable solution can be determined easily from the initial conditions:

$$A = 0 \Rightarrow i(t) = B \cdot \sin(\omega_0 \cdot t)$$

$$V(t) = L \frac{\partial i(t)}{\partial t} = L \cdot B \cdot \omega_0 \cdot \cos(\omega_0 \cdot t), \quad V(t=0) = V_0 \Rightarrow B = \frac{V_0}{L \cdot \omega_0}. \quad (4.37)$$

The loop current and voltage read as:

$$i(t) = \frac{V_0}{L \cdot \omega_0} \cdot \sin(\omega_0 \cdot t) \quad (4.38)$$

$$V(t) = V_0 \cdot \cos(\omega_0 \cdot t)$$

These familiar waveforms are sketched in Figure 4-12.

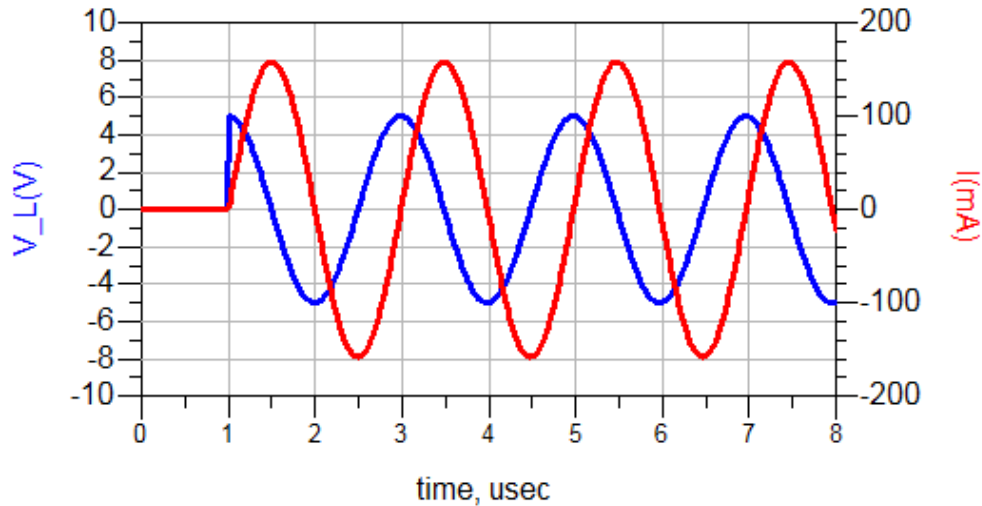


**Figure 4-12** Signal waveforms in a stable LC tank circuit, **blue** – voltage, **red** - current

As it is well known the phase shift between voltage and current is 90 degrees. The instantaneous power at the inductor and the capacitor can be found as:

$$p_L(t) = v(t) \cdot i(t) = \frac{V_0^2}{L \cdot \omega_0} \cdot \sin(\omega_0 \cdot t) \cdot \cos(\omega_0 \cdot t)$$

$$p_C(t) = -v(t) \cdot i(t) = -\frac{V_0^2}{L \cdot \omega_0} \cdot \sin(\omega_0 \cdot t) \cdot \cos(\omega_0 \cdot t) \quad (4.39)$$

The instantaneous stored energy quantities read as:

$$W_L = \frac{1}{2} \cdot L \cdot i^2(t) = \frac{V_0^2}{2 \cdot L \cdot \omega_0^2} \cdot \sin^2(\omega_0 \cdot t) = \frac{V_0^2}{2} \cdot C \cdot \sin^2(\omega_0 \cdot t)$$

$$W_C = \frac{1}{2} \cdot C \cdot V^2(t) = \frac{V_0^2}{2} \cdot C \cdot \cos^2(\omega_0 \cdot t)$$

$$W_{total} = \frac{V_0^2}{2} C [\cos^2(\omega_0 t) + \sin^2(\omega_0 t)] = \frac{V_0^2}{2} C.$$

(4.40)

The instantaneous power and energy waveforms are plotted in Figure 4-13 and Figure 4-14, respectively.

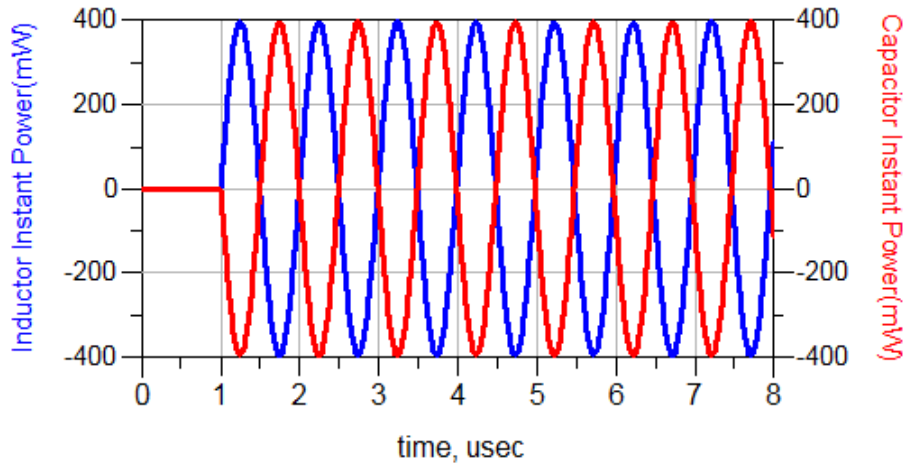


**Figure 4-13** Instantaneous power on the elements of a stable LC tank circuit, **Blue** - power on the inductor, **Red** - power on the capacitor

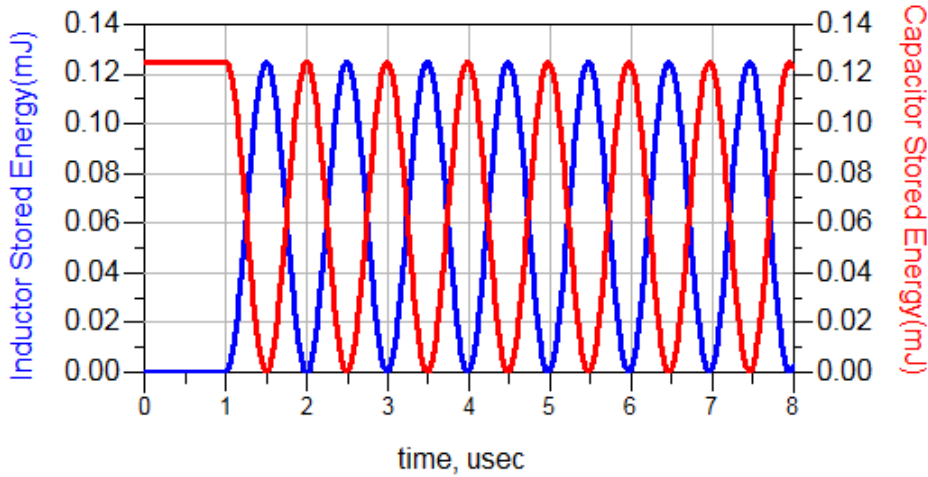


**Figure 4-14** Instantaneous stored energy on the elements of a stable LC tank circuit, **Blue** – energy on the inductor, **Red** – energy on the capacitor

Until the switch is closed ( $0 < t < 1\mu\text{s}$ ), the whole amount of energy is stored in the capacitor. (Figure 4-13). When the switch closes at  $t_0 = 1\mu\text{s}$ , the instant power becomes negative in the capacitor and positive in the inductor (Figure 4-14). This means that the energy is being transferred from the capacitor to the inductor. At  $T/4$  ( $T$  being the period of the signal) the whole amount of the energy is stored in the inductor. After this moment, the instant power in the inductor becomes negative, so the inductor starts to transfer the energy back to the

capacitor. At  $T/2$  the whole amount of energy is again stored in the capacitor. This process repeats periodically each  $T/2$  and (in an idealized case with no losses) does not stop at all.

It is interesting (and somehow surprising) that this familiar *stable* resonant process occurs even in the case of negative capacitor *and* negative inductor. In this case, a negative capacitor behaves as an ordinary inductor, while the negative inductor behaves as an ordinary capacitor. Of course, their frequency characteristics are ‘inverted’ characteristics of ordinary positive elements. However, this difference cannot be noticed from ‘outside world’ (for instance by measuring the voltage developed across and the current flowing through the  $LC$  circuit). Thus, the behavior of an idealized ‘negative’  $LC$  circuit, in the case with no driving source, is equal to the behavior of an ordinary  $LC$  circuit.

#### 4.3.4. Positive/negative parallel $LC$ tank circuit driven by an external source

Let us now consider the positive/negative parallel tank circuit connected to an external harmonic voltage source with internal resistance  $R$  (Figure 4-15). In order to analyze the most general case, the resistor  $R$  is allowed to be either positive ( $R>0$ ) and negative ( $R<0$ ).

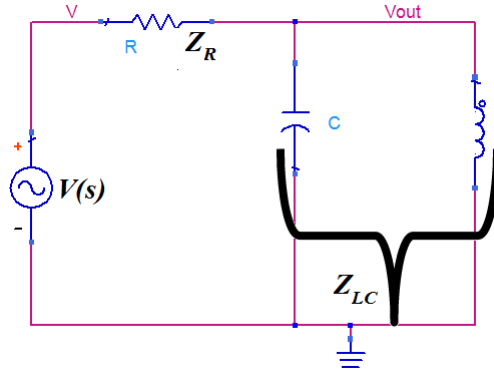


**Figure 4-15** Positive/negative  $LC$  tank circuit driven by a voltage source

The stability properties of this circuit can be studied by using the Laplace transform. The elements of the network in the Laplace domain read as:

$$\begin{aligned} Z_{CL}(s) &= 1 / (s \cdot C) // L \cdot s = \frac{s \cdot L}{1 + s^2 \cdot L \cdot C} \\ Z_R &= R \\ V(s) &= V_0 \cdot \frac{\omega_0}{\omega_0^2 + s^2} \end{aligned} \quad (4.41)$$

Then, the Laplace transform of the output voltage (the voltage across  $LC$  circuit) is given by:

$$\begin{aligned} V_{out}(s) &= V_s(s) \cdot \frac{Z_{CL}(s)}{Z_{CL}(s) + Z_R} = \frac{V_0 \cdot \omega_0}{(\omega_0^2 + s^2)} \cdot \frac{L \cdot s}{(s \cdot L + R + R \cdot L \cdot C \cdot s^2)} = \\ &= \frac{V_0 \cdot \omega_0 \cdot L \cdot s}{R \cdot L \cdot C \cdot s^4 + L \cdot s^3 + (R + \omega_0^2 \cdot R \cdot L \cdot C) \cdot s^2 + \omega_0^2 \cdot L \cdot s + \omega_0^2 \cdot R} \end{aligned} \quad (4.42)$$

Now, one can simply inspect the roots of the polynomial in the denominator. The circuit is stable if there are no roots (poles) in the right-hand-side of complex plane. Therefore, the stability of the circuit can be studied by analyzing the poles locations for the different combinations of positive and negative signs of  $R$ ,  $L$  and  $C$ .

The first example (Figure 4-16) shows poles loci for the positive inductor ( $L>0$ ) and the positive resistor ( $R>0$ ). It can be seen that for an increase of a positive capacitance ( $C>0$ ), the poles move toward the imaginary axis but they never come into the RHS of the complex plane. So, in this case ( $R>0$ ,  $C>0$ ,  $L>0$ ) the driven  $LC$  circuit is stable (since it is actually ordinary driven  $LC$  circuit, a stable operation is, of course, expected). In the case of the negative capacitor ( $C<0$ ), one pole is always located in the RHS of the complex plane and the circuit is unstable.

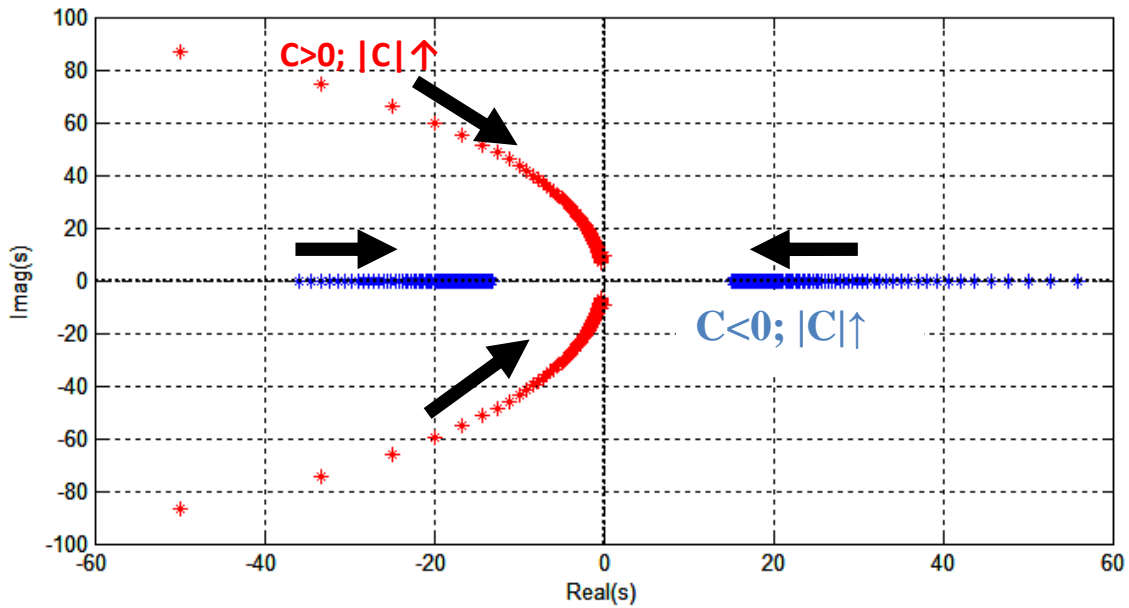


**Figure 4-16** Loci of the poles of the driven positive/negative  $LC$  circuit for  $L>0$ ,  $R>0$

In the second example, an inductor is negative while the resistor is positive ( $L<0$ ,  $R>0$ ). Analysis of the pole loci in Figure 4-17 reveals that a circuit is unstable either for positive capacitor ( $C>0$ ) or for negative capacitor ( $C<0$ ).

Finally, Figure 4-17 shows loci of the poles in the case of both negative inductor ( $L<0$ ) and negative resistor ( $R<0$ ). It can be seen that this driven  $LC$  circuit is stable if a capacitor is negative ( $C<0$ ). On the contrary, the circuit is unstable if the capacitor is positive ( $C>0$ ).

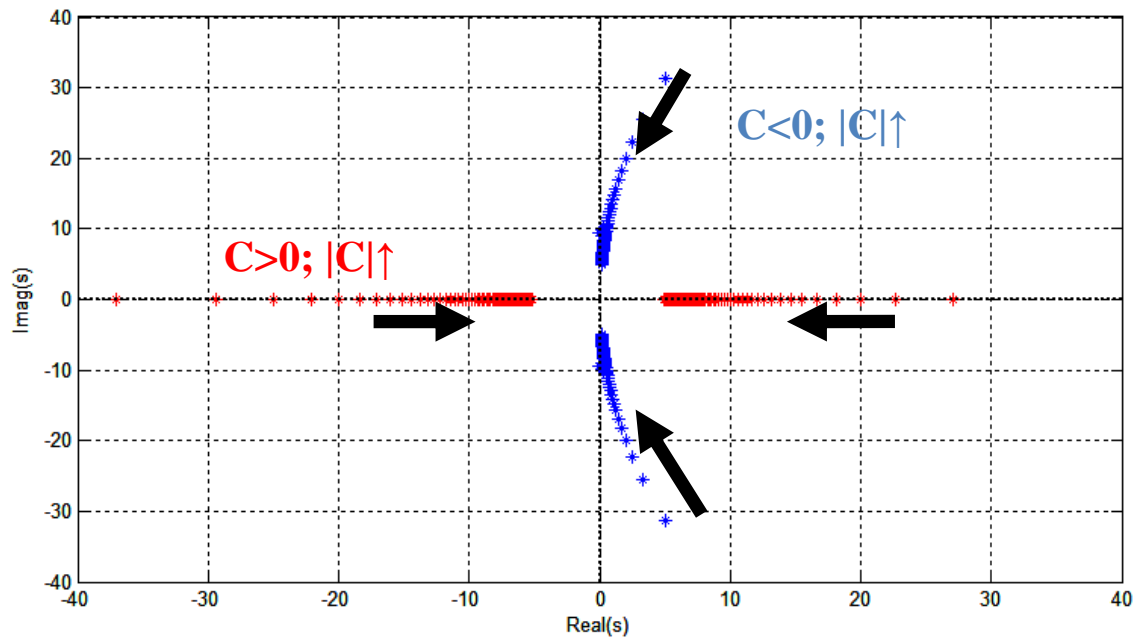


**Figure 4-17** Loci of the poles of the driven positive/negative  $LC$  circuit for  $L<0, R<0$

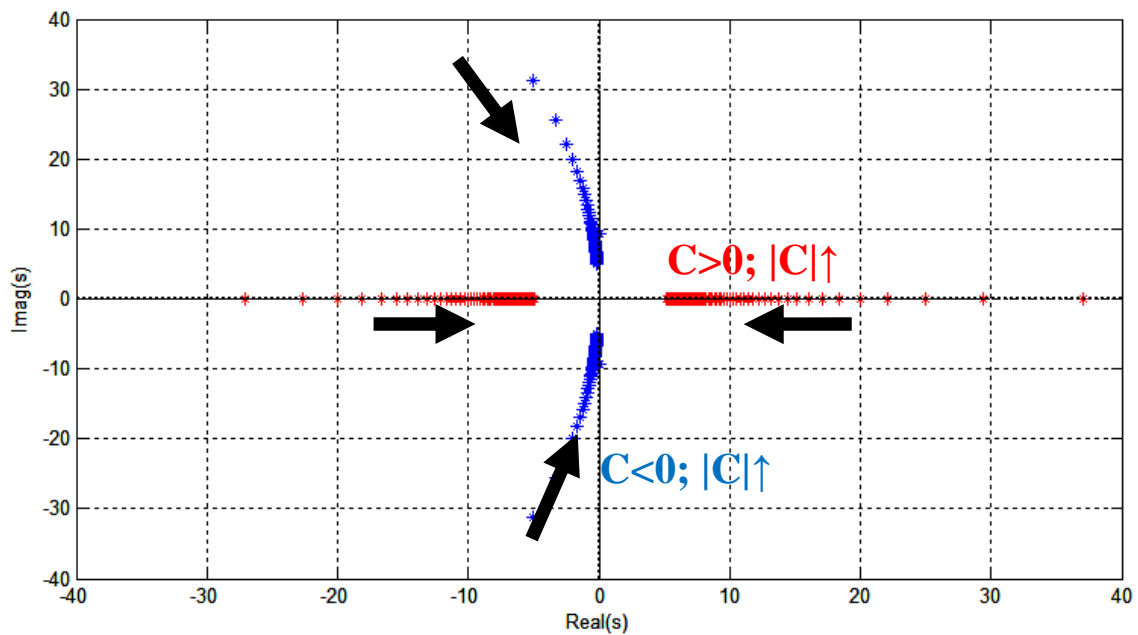


**Figure 4-18** Loci of the poles of the driven positive/negative  $LC$  circuit for  $L<0, R<0$

One can notice the similarity with the analysis of the natural response of positive/negative  $LC$  circuit: the circuit is stable only if all the elements have the same sign (either positive or negative).

The stability of the driven positive/negative  $LC$  circuit is summarized in Table 4-2 :

sign of R	sign of C	sign of L	Stability
+	+	+	Stable
+	-	+	Unstable
+	+	-	Unstable
+	-	-	Unstable
-	+	+	Unstable
-	-	-	Stable
-	+	-	Unstable
-	-	+	Unstable

**Table 4-2** Stability criteria for driven positive/negative LC tank circuit

#### 4.3.5. Parallel $CC_n$ circuit – natural response

The parallel  $CC_n$  circuit (Figure 4-19) that represents a basic building element of an active broadband ENZ metamaterial [29] is analyzed in this section. At the same time, it can be interpreted as an equivalent circuit of frequently proposed active matching circuit of a small antenna [30-45]. The circuit comprises both positive ( $C_1$ ) and negative ( $C_2$ ) capacitor, which are connected in parallel. It actually resembles classical  $LC$  ‘tank’ circuit. The capacitor  $C_1$  is assumed to be initially charged (initial voltage  $V_0=5V$ ). The switch abruptly connects  $C_1$  to  $C_2$  at  $t_0$ .

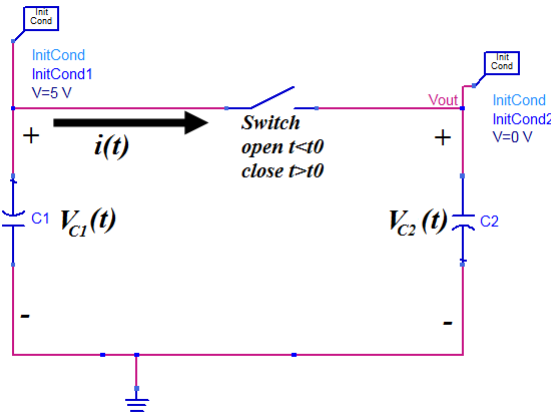


**Figure 4-19** Parallel  $CC_n$  circuit

The currents in the loop are given by:

$$\left. \begin{aligned} i(t) &= -C_1 \cdot \frac{\partial V(t)}{\partial t} \\ i(t) &= C_2 \cdot \frac{\partial V(t)}{\partial t} \end{aligned} \right\} \Rightarrow \frac{i(t)}{-C_1} = \frac{i(t)}{C_2} \quad (4.43)$$

It can be seen that the analysis of the circuit in Figure 4-19 gives rather unusual results. The current  $i(t)$  can exist in the loop only if  $C_1 = -C_2$ , and this current can have *completely arbitrary waveform*. So, the solution is not a monochromatic sinusoidal signal, as it would be the case

in an ordinary  $LC$  tank circuit. It is a direct consequence of the assumption of ideal non-dispersive nature of the negative capacitor. From practical point of view, the arbitrary waveform means just the onset of the instability (oscillations). On the contrary if  $C_1$  is not equal to  $C_2$ , the equations (4.43) are satisfied only if the current  $i(t)$  is equal to zero. In other words, the voltages on two capacitors are equal, but with the opposite signs. This constant voltage can be determined by an analysis of the total charge in the circuit:

$$Q_{total} = C_1 \cdot V_0 \quad (4.44)$$

After the time instant  $t_0$ , at which the switch closes, the total charge becomes  $Q_{total}=q_1+q_2$ ,  $q_1$  and  $q_2$  being the charges on the two capacitors:

$$Q_{total} = q_1 + q_2 = V_{final} \cdot C_1 + V_{final} \cdot C_2 = V_{final} \cdot (C_1 + C_2) \quad (4.45)$$

So, the final voltage will be:

$$V_{final} = V_0 \cdot \left( \frac{C_1}{C_1 + C_2} \right) \quad (4.46)$$

It is interesting that the result of this calculation shows the difference in amount of total energy before and after the time instant at which the switch closes ( $t_0$ ):

$$W_0 = \frac{1}{2} \cdot C_1 \cdot V_0^2$$

$$W_{final} = W_{c1} + W_{c2} = \frac{1}{2} \cdot C_1 \cdot V_{final}^2 + \frac{1}{2} \cdot C_2 \cdot V_{final}^2 = \frac{1}{2} \cdot V_{final}^2 \cdot (C_1 + C_2) = \frac{1}{2} \cdot V_0^2 \cdot \frac{C_1^2}{(C_1 + C_2)} = W_0 \cdot \frac{C_1}{(C_1 + C_2)} \quad (4.47)$$

When both  $C_1$  and  $C_2$  are positive, the final voltage is lower than the initial one,  $V_{final} < V_0$  and also the energy is lower than the initial one,  $W_{final} < W_0$ . This artifact of “lost” energy is known and it comes from the fact that the circuit theory presumes infinitely small loops and neglects the magnetic flux generated across the closed loop. Therefore, it neglects the associated induced voltage along the ‘wires’ (i.e. the existence of inevitable ‘parasitic inductances’). This approach is valid only if the dimension of the loop is much smaller than the wavelength at the maximal frequency of the signal. However, in this analysis, the signal that occurs during the discharging of the capacitor has infinite spectrum and a circuit-theory approach fails here. Actually, the ‘missing energy’ is associated with the neglected magnetic field generated during the transient state, i.e. with the radiation. This phenomenon is shown in the next numerical example (the upper part of Figure 4-20):

- The initial voltage is  $V_0=5V$  and the capacitors are  $C_1=10\mu F$  and  $C_2=5\mu F$ 
  - Initial energy:  $W_0=1/2 \cdot 10^{-6} \cdot 5^2=0.125mJ$
  - Final Voltage:  $V_{final}=3.33V$
  - Final Energy:  $W_{final}=0.0833mJ$



On the other hand, if  $C_2$  is negative, both the calculated final voltage and total final energy are found to be larger than the initial values. The parameters of the numerical example (the lower part of Figure 4-20) are:

- The initial voltage is  $V_0=5V$  and the capacitors are  $C_1=10\mu F$  and  $C_2=-5\mu F$ 
  - Initial energy:  $W_0=1/2 \cdot 10^{-6} \cdot 5^2=0.125mJ$
  - Final Voltage:  $V_{final}=10V > V_0$
  - Final Energy:  $W_{final}=0.25mJ > W_0$

The energy increase observed in this example is not just an artifact. It can only be explained by taking into account that the negative capacitance is active, so the active electronic circuit of the negative capacitance ( $C_2$ ) transfers energy to the positive capacitor ( $C_1$ ).

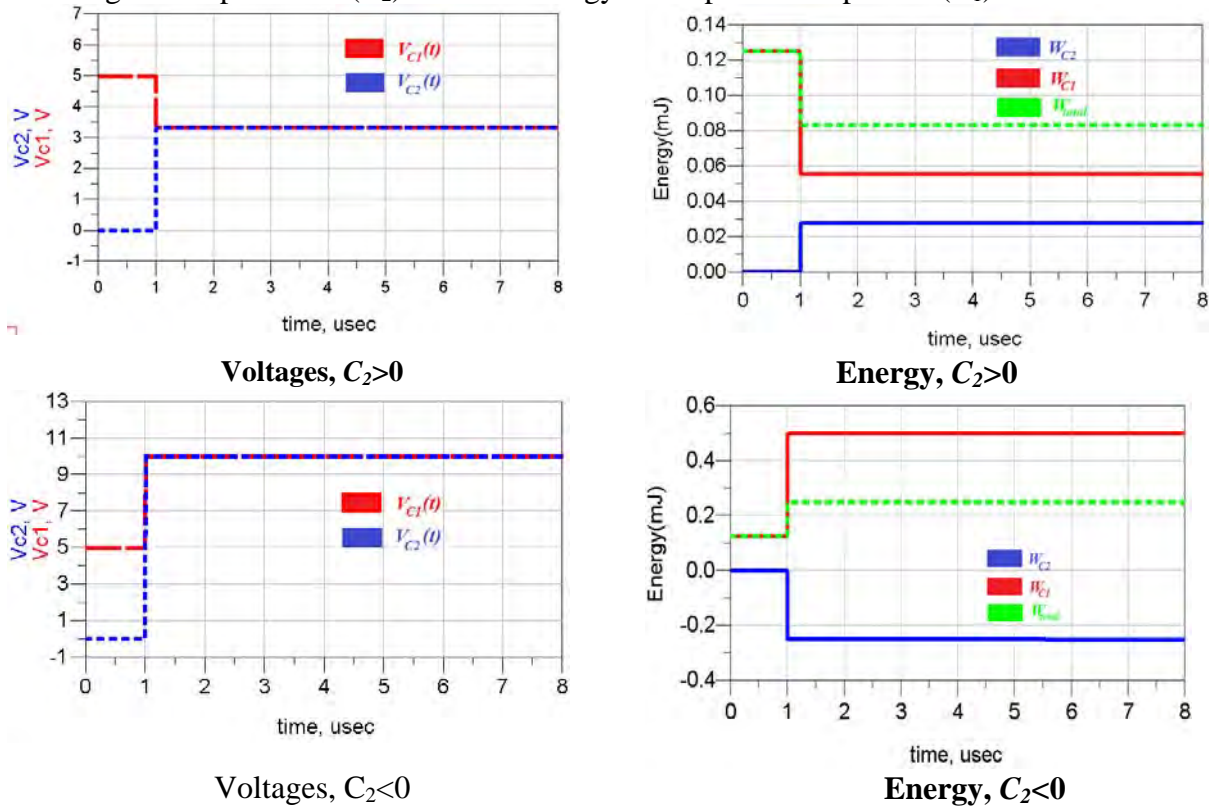


**Figure 4-20** Voltages and Energy in a  $C$ - $C_n$  circuit

According to (4.43), the circuit is stable for all values and the signs of capacitances, except for the case of  $C_2 = -C_1$ . For these values, the final voltage ( $V_s C_2 / C_1$ ) diverges (showing unstable behavior) (Figure 4-21). However, this result seems to be in a conflict with known experimental result that this circuit is unstable not only for  $C_2 = -C_1$  but also for  $C_1 > 0$ ,  $C_2 < 0$  and  $|C_2| > C_1$ . This (apparent) inconsistency happens because the above analysis neglects existence of any AC signal at  $t=0$ . In practice, the noise is always present, so one should study a driven circuit. Analysis in the next section will show that this leads to instability for the case of  $C_1 > 0$ ,  $C_2 < 0$  and  $|C_2| > C_1$ .

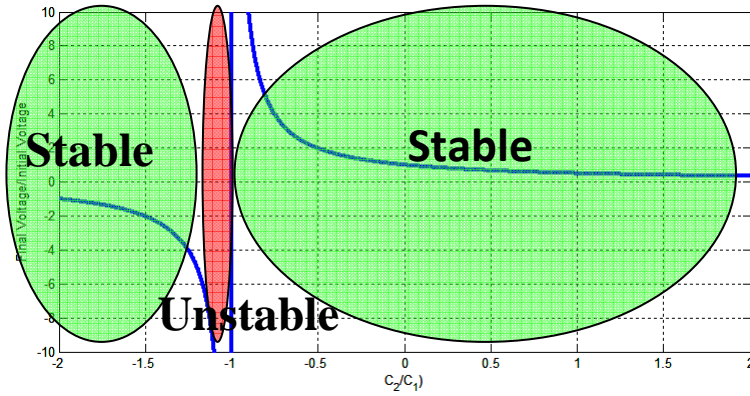


**Figure 4-21** Stability regions for the  $CC_n$  circuit with no driving source

sign of $C_1$	sign of $C_2$	Stability
+	+	<b>Stable</b>
+	-	<b>Stable</b>
+	-	<b>Unstable (if <math> C_2  = C_1</math>)</b>

**Table 4-3** Stability criteria for  $CC_n$  circuit with no driving source

#### 4.3.6. Parallel $CC_n$ circuit driven by an external source

The analysis of the parallel  $CC_n$  circuit driven by an external harmonic voltage source with internal resistance  $R$  (Figure 4-22) is shown in this section. Again, the most general case, in which the resistor  $R$  is allowed to be either positive ( $R > 0$ ) or negative ( $R < 0$ ) is considered.

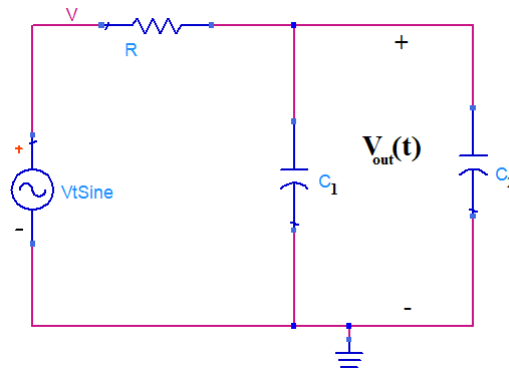


**Figure 4-22** Parallel  $CC_n$  circuit driven by an external source

The network elements and signals in Laplace domain are given by:

$$\begin{cases} Z_{C_1 C_2} = \frac{1}{s \cdot (C_1 + C_2)} = \frac{1}{s \cdot C_{eq}} \\ Z_R = R \\ V(s) = V_0 \cdot \frac{\omega_0}{\omega_0^2 + s^2} \end{cases} \quad (4.48)$$

The Laplace transform of the output voltage (the voltage across the capacitors) is given by:

$$V_{out}(s) = \frac{V_0 \cdot \omega_0}{\omega_0^2 + s^2} \cdot \left[ \frac{1/s \cdot C_{eq}}{R + \frac{1}{s \cdot C_{eq}}} \right] = \frac{V_0 \cdot \omega_0}{\omega_0^2 + s^2} \cdot \left( \frac{1}{1 + s \cdot R \cdot C_{eq}} \right) = \frac{V_0 \cdot \omega_0}{R \cdot C_{eq} \cdot s^3 + s^2 + R \cdot C_{eq} \cdot \omega_0^2 \cdot s + \omega_0^2} \quad (4.49)$$

This circuit will be stable if all the poles are located in the left-hand side of the complex plane. Figure 4-23 shows the loci of the poles for  $R>0$ ,  $C_1>0$  and for different values of  $C_2$ . If  $C_2>0$  the solution is stable as it was expected (red curve). However, if  $C_2<0$  the circuit will be stable only if  $|C_2|<C_1$ , or, what is the same, if  $C_{eq}$  is positive (blue trace). When  $C_2$  is equal to  $-C_1$ , the circuit is at the edge of stable region ( $V_{out}(t)=V_o(t)$ ) and the impedance of the  $CC_n$  circuit becomes infinite. On the other hand, if  $|C_2|>C_1$ , the  $CC_n$  circuit is unstable (green curve).

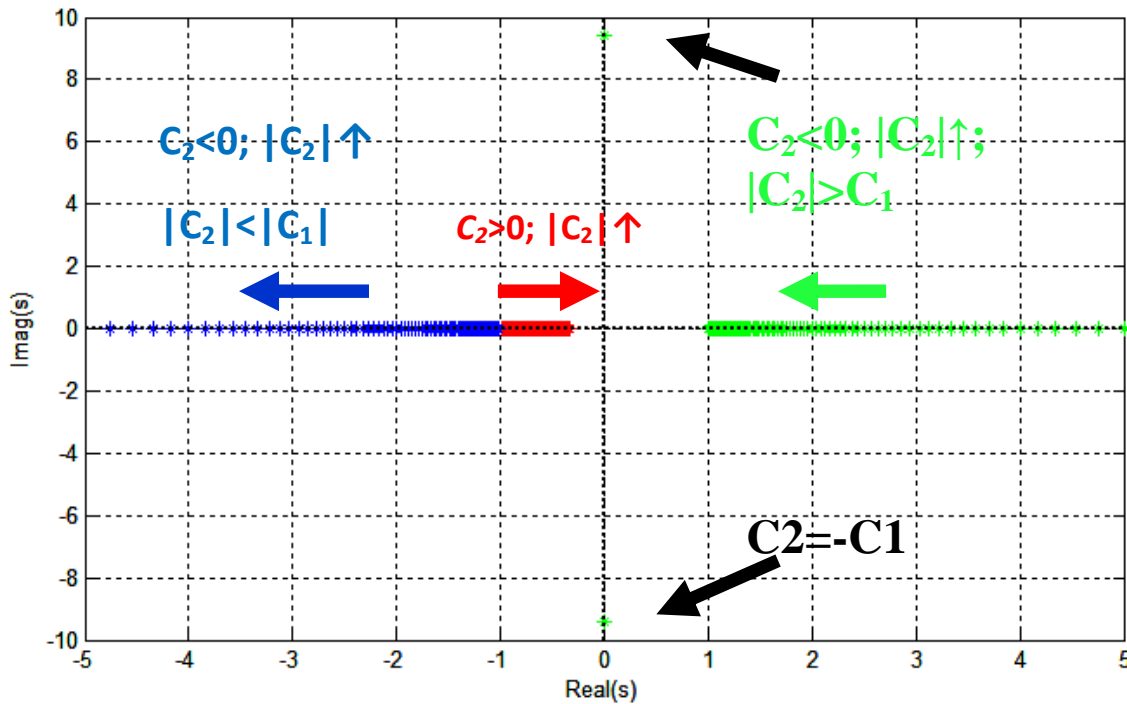


**Figure 4-23** Loci of the poles of the driven  $CC_n$  circuit for  $C_1>0$ ,  $R>0$

The waveforms of voltage, currents, powers and energies for all the stable cases are shown in Figure 4-24 and Figure 4-25. When both  $C_1>0$  and  $C_2>0$ , the currents through the capacitors are in phase, as well as the instantaneous power levels. Thus, both capacitors charge and discharge simultaneously extracting/transferring energy from/to the driving voltage source (please see the lower part of Figure 4-25).

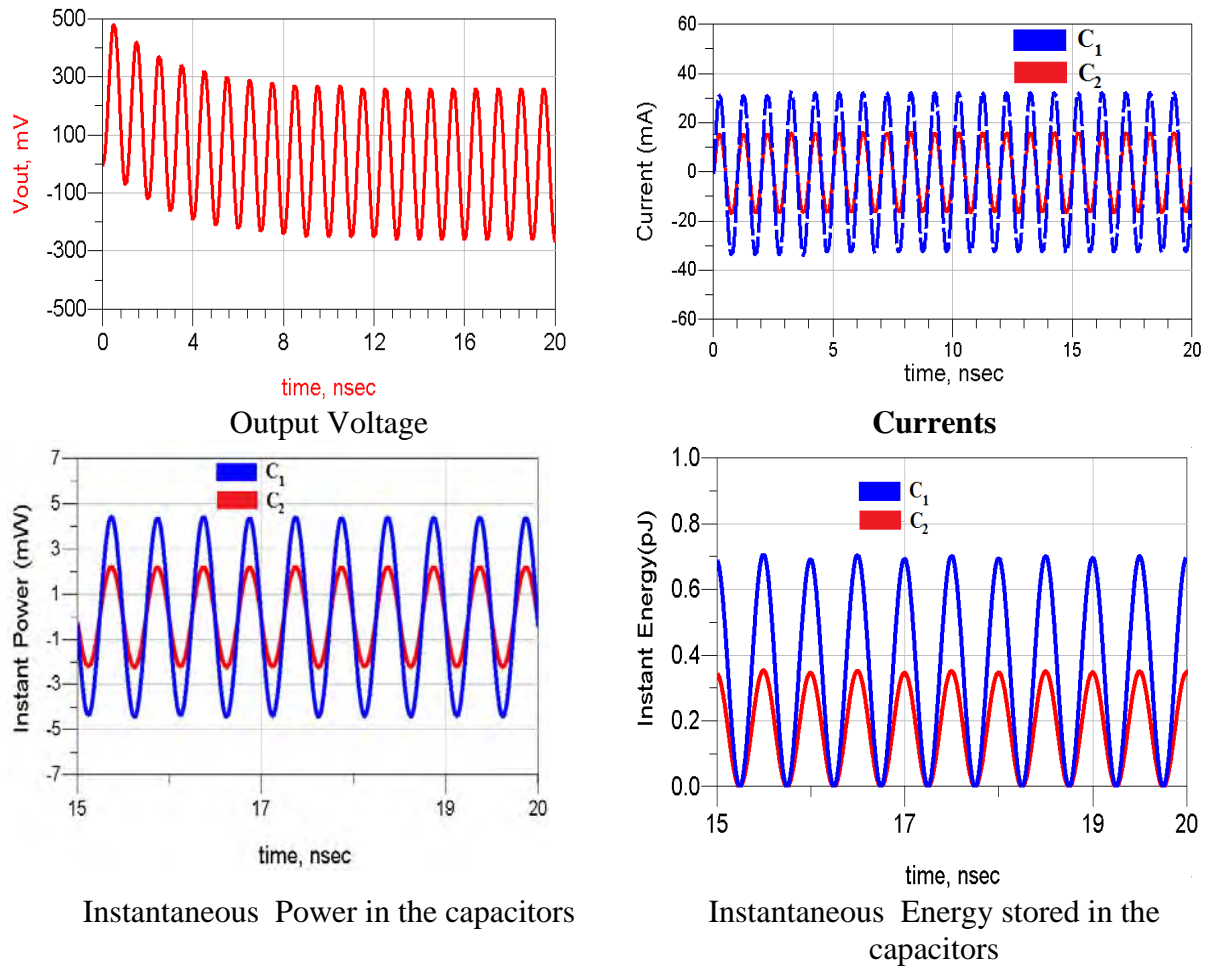


**Figure 4-24** Voltage, currents, power and energy in the  $CC_n$  circuit with  $C_2 > 0$

In the case of  $C_2 < 0$  and  $|C_2| < C_1$  (a stable solution shown in Figure 4-25), the currents and the instantaneous powers on the capacitors are out of phase. It means that the negative capacitor ( $C_2$ ) is transferring energy to the positive capacitor ( $C_1$ ). The amount of energy in  $C_1$  is larger than in  $C_2$ , so the positive capacitor ( $C_1$ ) extracts some energy from the voltage source (as in the previous case). For  $C_2 < 0$  and  $|C_2| > C_1$  the output voltage increases exponentially (the unstable solution).

Above results show that is possible to build a stable broadband active ENZ metamaterial (its equivalent capacitance is positive, thus,  $|C_2| < C_1$ ). Unfortunately, the stable active ENG metamaterial (its equivalent capacitance is negative, thus,  $|C_1| < C_2$ ) does not seem to be feasible (at least if it uses the  $CC_n$  circuit). Here, one can make a comment on the research in the field of small antennas [31-36, 39-45]. Many (mainly numerical) studies did not consider stability issues at all and they suggested complete compensation of antenna reactance by non-Foster negative capacitance ( $|C_1| = C_2$ ). This would inevitably lead to the unstable operation.

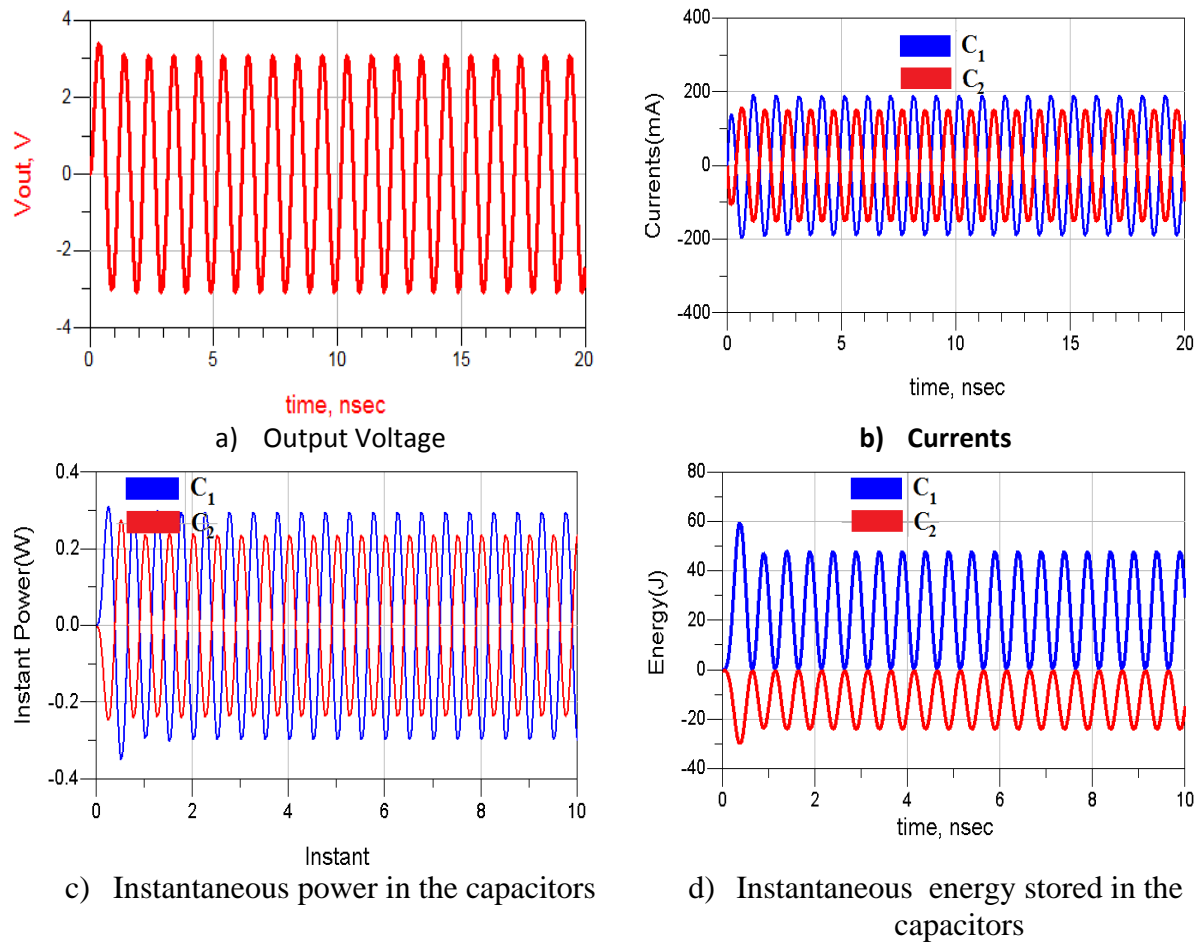


**Figure 4-25** Voltage, currents, instantaneous power and energy in  $CC_n$  circuit with  $C_2 < 0$

The results of above discussion are summarized in Table 4-4.

sign of $C_1$	sign of $C_2$	Stability
+	+	Stable
+	-	Stable (if $ C_2  < C_1$ )
+	-	Unstable (if $ C_2  < C_1$ ) or $ C_2  = C_1$ (edge of the stability region)

**Table 4-4** Stability criteria for  $CC_n$  circuit driven by an external source

#### 4.3.7. Series/parallel $RC_n/C$ circuit – natural response

The next example (Figure 4-26) comprises initially charged ( $V_0=5V$ ) capacitor  $C_1$ , ( $C_1>0$ ) connected in parallel with series combination of the capacitor  $C_2$  (either  $C_2>0$  or  $C_2<0$ ), and a series resistor  $R$ . As in the previous case, there is an initially charged ( $V_0=5V$ )

positive capacitor  $C_1$ , that is connected to other capacitor  $C_2$ , with a series resistor  $R$  (either  $R>0$  or  $R<0$ ). This circuit represents a realistic negative capacitor with losses, connected in parallel with positive capacitor (a unit cell of broadband active ENZ metamaterial). The second interpretation could be an ideal negative capacitor connected to a small antenna, equivalent circuit of which contains a positive capacitance and a small radiation resistance.

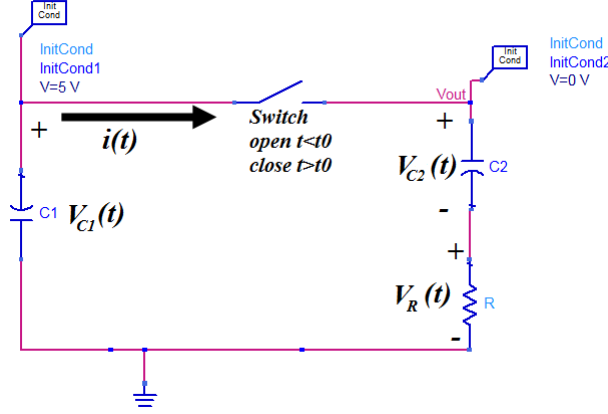


**Figure 4-26** Series/parallel  $RC_n/C$  circuit

The standard derivation of the voltages and the currents in the circuit directly leads to the first order differential equation:

$$\left. \begin{aligned} V_{c1}(t) &= -\frac{1}{C_1} \cdot \int_0^t i(\tau) d\tau + V_{c1}(0) \\ V_{c1}(t) &= i(t) \cdot R + \frac{1}{C_2} \cdot \int_0^t i(\tau) d\tau + V_{c2}(0) \end{aligned} \right\} \xrightarrow{\frac{\partial}{\partial t}} R \cdot \frac{\partial i(t)}{\partial t} + \frac{1}{C_2} i(t) + \frac{1}{C_1} i(t) = 0$$

$$\frac{\partial i(t)}{\partial t} + \frac{1}{R} \cdot \left( \frac{1}{C_2} + \frac{1}{C_1} \right) i(t) = 0 \xrightarrow{C_{eq} = \frac{C_1 \cdot C_2}{C_1 + C_2}} \frac{\partial i(t)}{\partial t} + \frac{1}{R \cdot C_{eq}} i(t) = 0 \quad (4.50)$$

The solution of above equation reads as:

$$i(t) = I_0 \cdot e^{-\left(\frac{1}{R \cdot C_{eq}}\right) \cdot t} \Rightarrow \text{If } C_2 < 0 \rightarrow C_{eq} = \frac{-|C_2| \cdot C_1}{C_1 - |C_2|} \Rightarrow \begin{cases} |C_2| > C_1 \rightarrow \text{Stable} \\ |C_2| < C_1 \rightarrow \text{Unstable} \end{cases} \quad (4.51)$$

As it can be seen, the resultant equivalent capacitance is the series combination of  $C_1$  and  $C_2$  rather than the parallel combination (which was the case in the previously analyzed example). Therefore, this circuit will be stable if  $C_{eq}>0$ , or, (what is actually the same),  $|C_2|>C_1$ . Comparing to the previous case ( a parallel  $CC_n$  circuit), *the stability criterion is flipped*.

Once the current  $i(t)$  is known, the voltages in the circuit can be derived easily:

$$\begin{aligned}
 V_{c1}(t) &= -\frac{1}{C_1} \cdot \int_0^t i(\tau) \cdot d\tau + V_0 = \frac{I_0}{C_1} \cdot R \cdot C_{eq} \cdot \left[ e^{-\frac{1}{R \cdot C_{eq}} t} - 1 \right] + V_0 \\
 V_{c2}(t) &= \frac{1}{C_2} \cdot \int_0^t i(\tau) \cdot d\tau + 0 = \frac{I_0}{C_2} \cdot R \cdot C_{eq} \cdot \left[ 1 - e^{-\frac{1}{R \cdot C_{eq}} t} \right]
 \end{aligned}
 \tag{4.52}$$

The voltages at the capacitors  $C_1$  and  $C_2$  become equal when time approaches infinity. Taking this into account one derives the initial current  $I_0$  and the final voltage  $V_{final}$ :

$$\begin{aligned}
 i(t \rightarrow \infty) &= 0 \rightarrow V_{c1}(t \rightarrow \infty) = V_{c2}(t \rightarrow \infty), \\
 V_0 - \frac{I_0}{C_1} \cdot R \cdot C_{eq} &= V_0 - \frac{I_0}{C_2} \cdot R \cdot C_{eq} \Rightarrow I_0 = \frac{V_0}{R}, \\
 V_{final} &= V_0 \frac{C_1}{C_1 + C_2}.
 \end{aligned}
 \tag{4.53}$$

As it was expected, the final voltage is equal to final voltage in the previously analyzed case. The difference is that, due to existence of series resistor, the voltage changes with time in an exponential manner (thus, the final voltage level is not reached instantaneously).

Figure 4-27 and Figure 4-28 show simulated voltage and currents for series/parallel  $RC_n/C$  circuit with  $C_1=10\mu F$ ,  $C_2=5\mu F$ , and  $R=250\ \Omega$ . The results obtained from simulations perfectly agree with those from presented theoretical analysis.

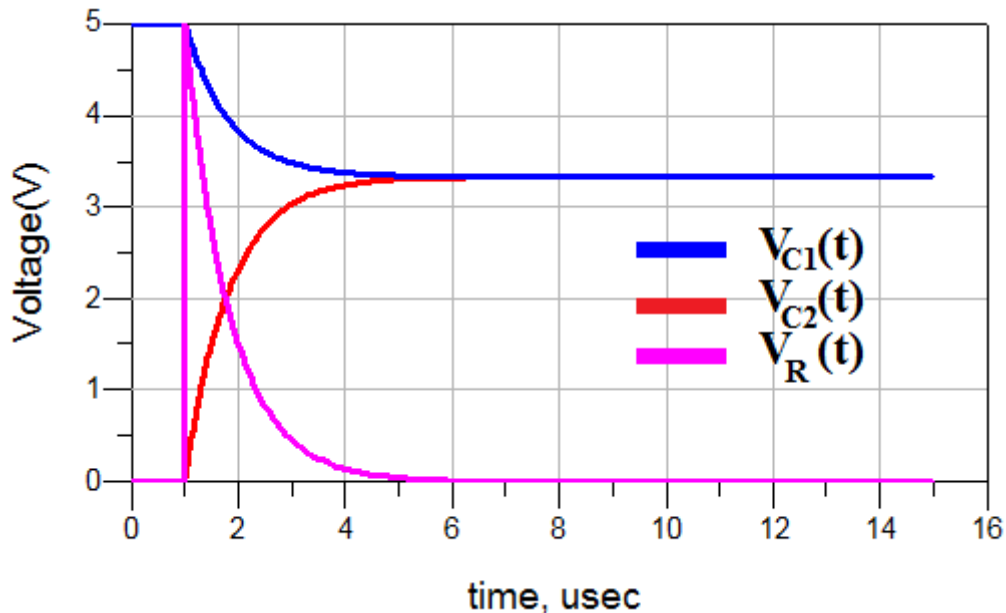


**Figure 4-27** Voltages in series/parallel  $RC_n/C$  circuit with  $C_2 > 0$

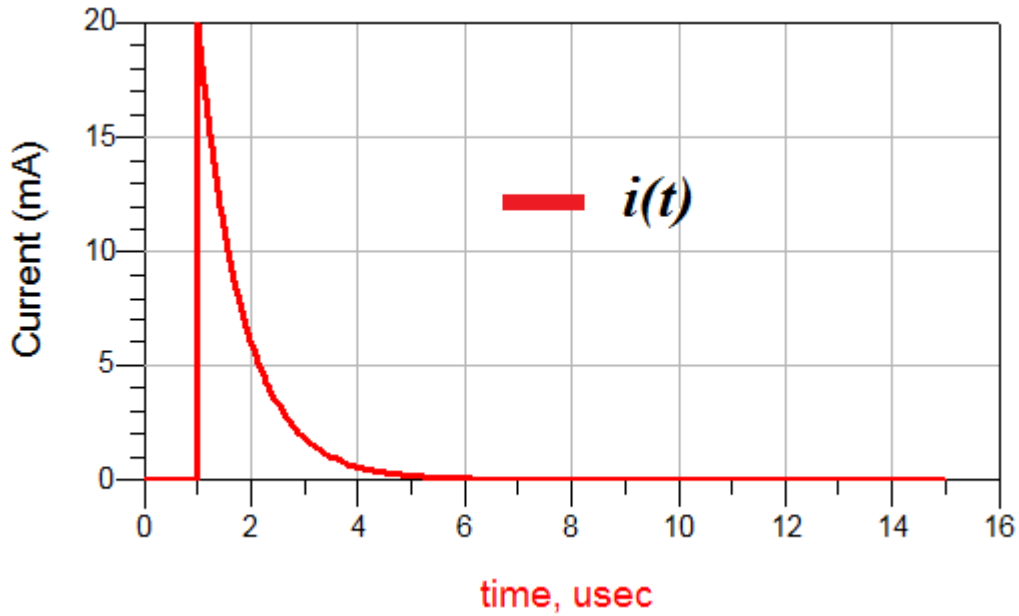


**Figure 4-28** Voltages in series/parallel  $RC_n/C$  circuit with  $C_2 > 0$

The instantaneous power and the energy stored/dissipated in the capacitors/resistors have also been simulated (Figure 4-29, Figure 4-30). When the switch closes at  $t_0 = 1 \mu s$ , the charged capacitor  $C_1$  transfers the energy to the uncharged capacitor  $C_2$  and to the resistor  $R$  (instant power at  $C_1$  is negative). After  $3 \mu s$ , the voltages at the capacitors are equal ( $V_{final}$ ) and the stored energy remains constant. Total energy within this period of time is constant (taking into account that the energy that is not stored in the capacitors  $C_1$  and  $C_2$  was dissipated in the resistor  $R$ ).

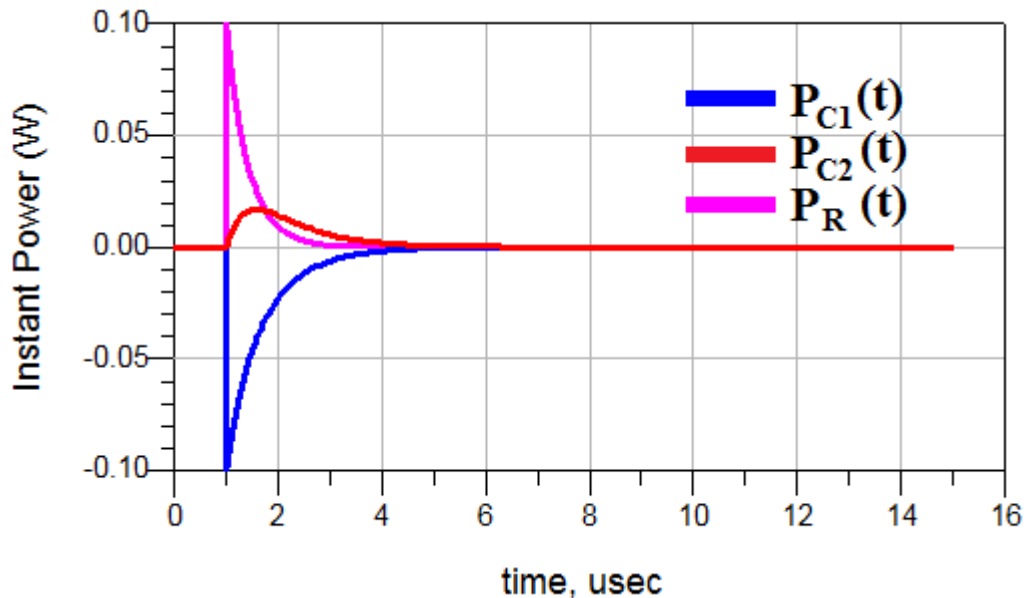


**Figure 4-29** Instantaneous power in series/parallel  $RC_n/C$  circuit with  $C_2 > 0$



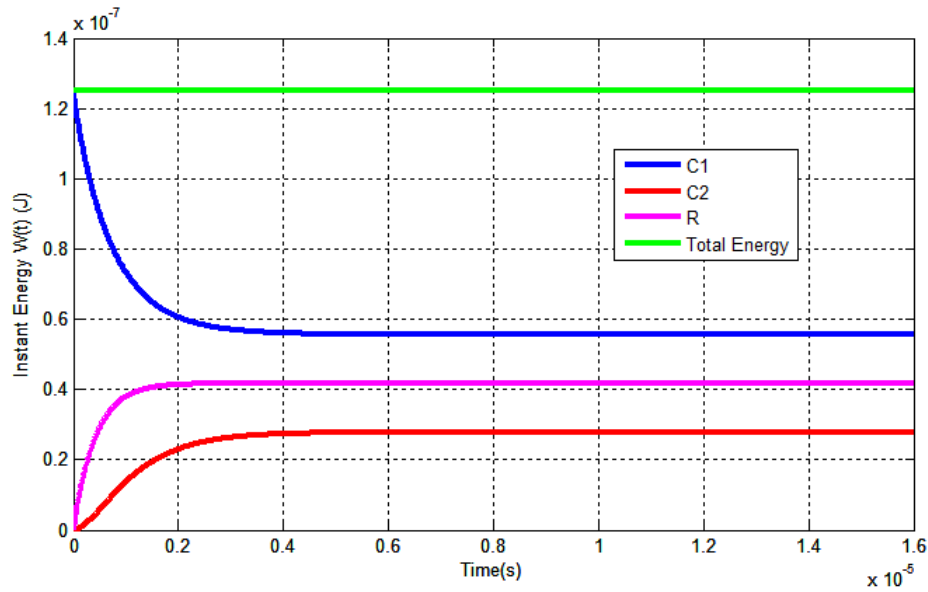


**Figure 4-30** Instantaneous energy in series/parallel  $RC_n/C$  circuit with  $C_2 > 0$

Figure 4-31 and Figure 4-32 show the simulated voltages and currents for the case with  $C_1 > 0$ ,  $C_2 < 0$  and  $|C_2| > C_1$  (the stable solution). The final voltage is negative due to  $|C_2| > C_1$ .

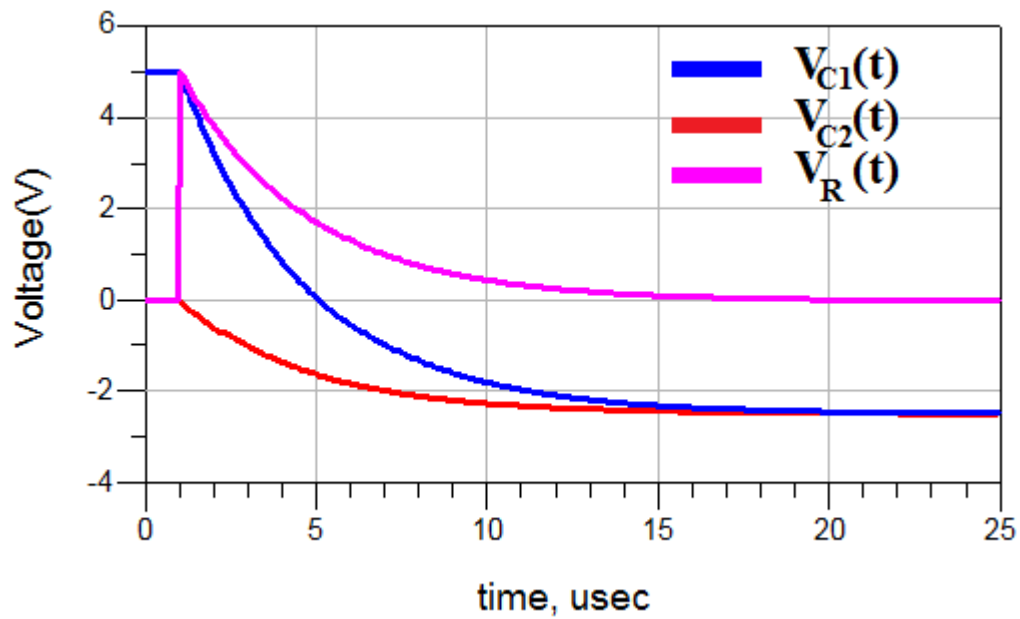


**Figure 4-31** Voltages in series/parallel  $RC_n/C$  circuit with  $C_2 < 0$  and  $C_2 < |C_1|$

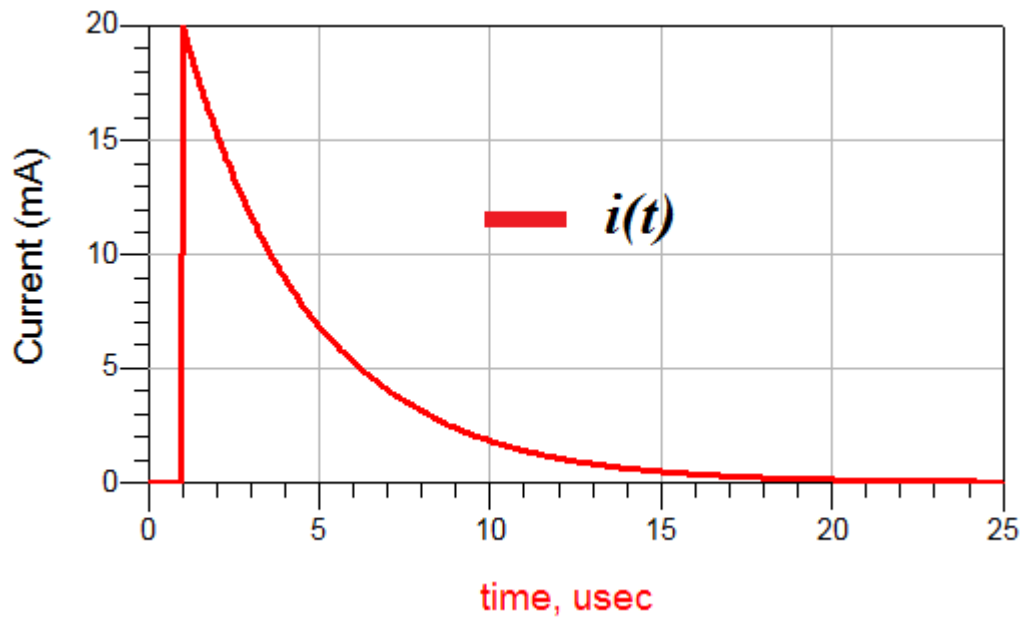


**Figure 4-32** Currents in series/parallel  $RC_n/C$  circuit with  $C_2 < 0$  and  $C_2 < |C_1|$

The instantaneous power and the energy stored in the capacitors and dissipated in the resistor have also been simulated and they are shown in Figure 4-33 and Figure 4-34, respectively.

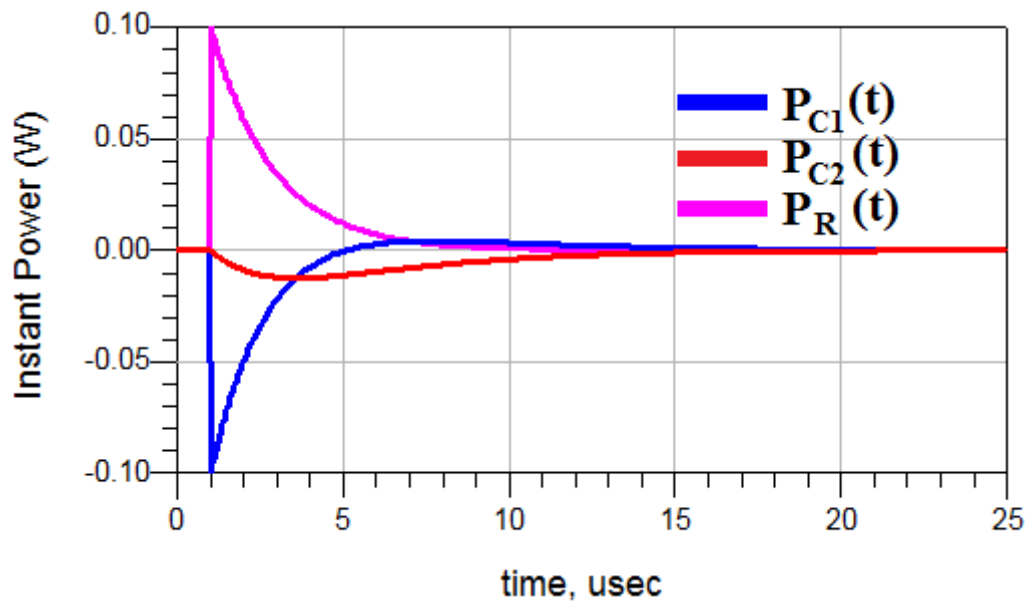


**Figure 4-33** Instantaneous power in series/parallel  $RC_n/C$  circuit with  $C_2 < 0$  and  $C_2 < |C_1|$

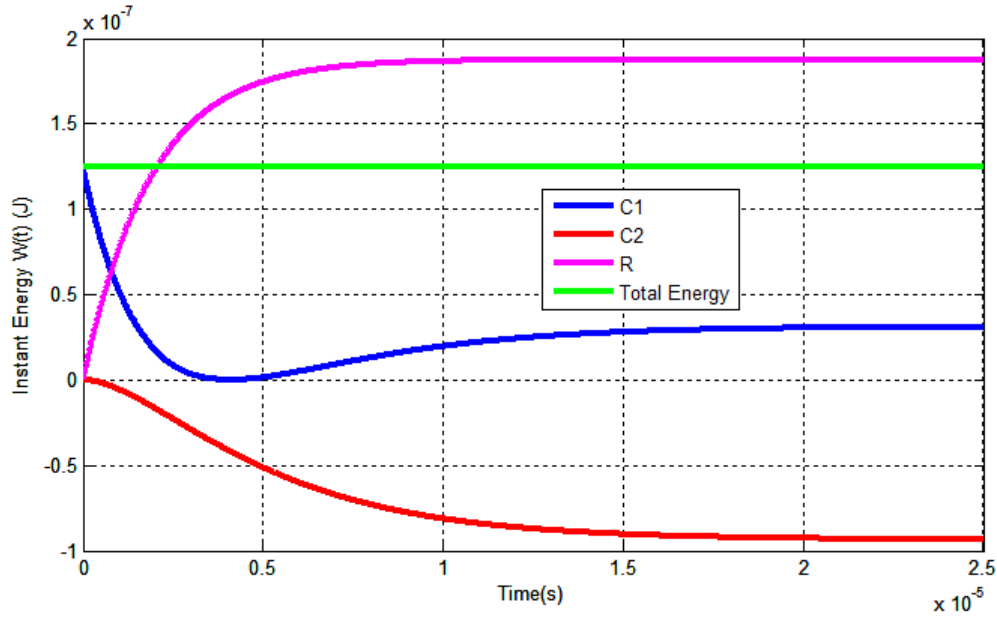


**Figure 4-34** Instantaneous energy in series/parallel  $RC_n/C$  circuit with  $C_2 < 0$  and  $C_2 < |C_1|$

After the switch closes, the energy (Figure 4-34) is transferred from the capacitors  $C_1$  ( $C_1 > 0$ ) and  $C_2$  ( $C_2 < 0$  so it can “store” negative energy) until the capacitor  $C_1$  is completely discharged. At this moment, the charging starts again and the energy is transferred from the capacitor  $C_2$ .

Finally, the voltages in the unstable case ( $C_2 < 0$  and  $|C_2| < C_1$ ) were simulated. Obtained results (Figure 4-35) clearly show exponential grow predicted by the theoretical analysis.

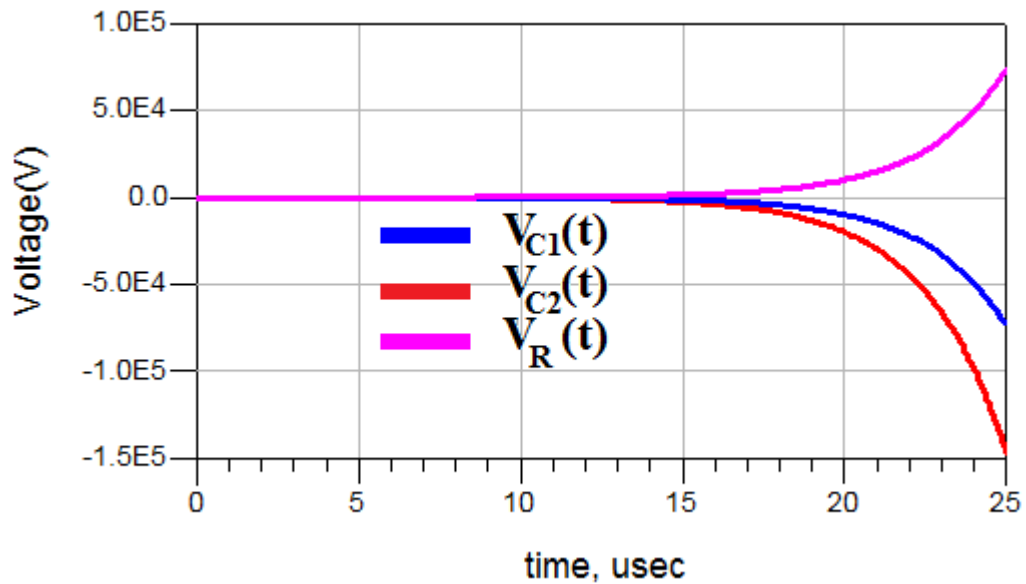


**Figure 4-35** Voltages in series/parallel  $RC_n/C$  circuit with  $C_2 < 0$  and  $C_2 > |C_1|$

Finally, it should be pointed out that the final voltage level is equal to that in case of  $CC_n$  circuit:

$$V_{final} = V_0 \cdot \frac{C_1}{C_1 + C_2} \quad (4.54)$$

However, there is also one important difference: the circuit is unstable for the case of  $-1 < C_2/C_1 < 0$ , i.e. the stability criterion is flipped (Figure 4-36). This is a direct consequence of the existence of series resistor  $R$ .

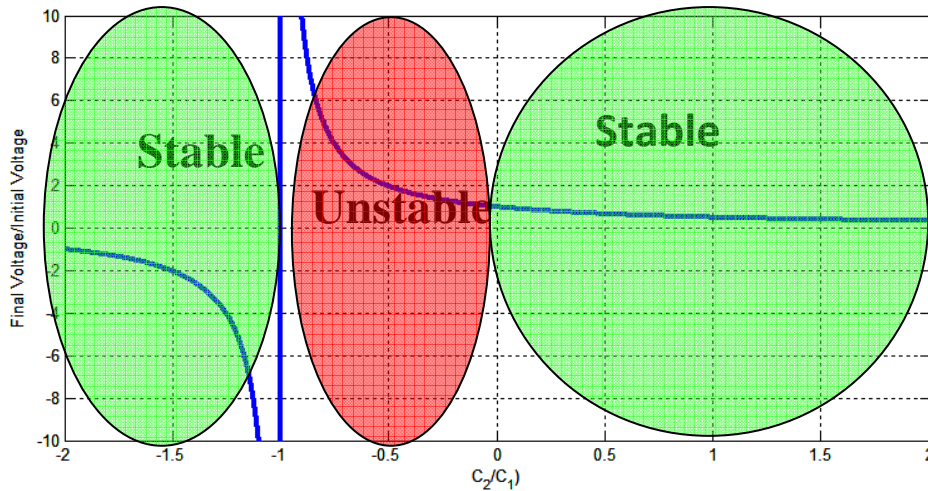


**Figure 4-36** Stability regions for series/parallel  $RC_n/C$  circuit with no driving source

The stability criteria of the series/parallel  $RC_n/C$  circuit is summarized in:

$R$	$C_{eq} = C_1 C_2 / (C_1 + C_2)$	Stability
+	+	Stable (if $C_2 > 0$ , $C_2 < 0$ and $ C_2  > C_1$ )
+	-	Unstable (if $ C_2  < C_1$ )
-	-	Stable
-	+	Unstable

**Table 4-5** Stability criteria for series/parallel  $RC_n/C$  circuit with no driving source

#### 4.3.8. Parallel $RCC_n$ circuit – natural response

In this section we study the natural response of a circuit formed by two parallel capacitors and a resistor. The circuit is shown in Figure 4-37. As is it was the case in the previous examples, the capacitor  $C_1$  is initially charged and it is abruptly connected to  $C_2$  and  $R$  in  $t=t_0$ . This circuit can model the behavior of a  $CC_n$  circuit connected to a spectrum analyzer. (This situation occurs during the measurement of realistic negative capacitors. Since

the isolated negative capacitor is unstable, a stabilizing positive capacitor is usually connected in parallel and its influence is de-embedded afterwards, see section 5.3.)

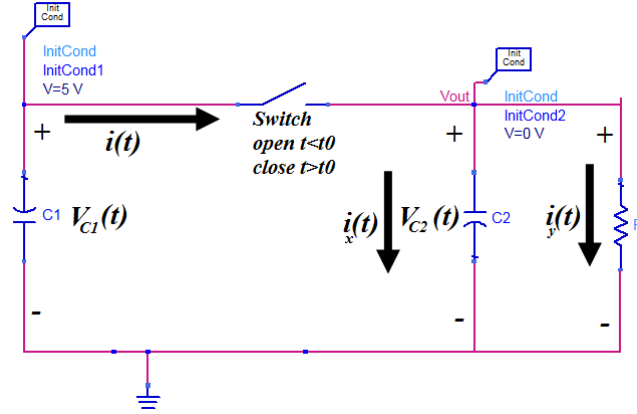


**Figure 4-37** Parallel  $RCC_n$  circuit with no driving source

The voltages and currents in the circuit are:

$$\begin{cases} V_{c2}(t) = \frac{1}{C_2} \cdot \int_0^t i_x(\tau) d\tau + V_{c2}(0) \\ V_{c1}(t) = -\frac{1}{C_1} \cdot \int_0^t i(\tau) d\tau + V_{c1}(0) \\ V_{c2}(t) = i_y(t) \cdot R \\ i(t) = i_x(t) + i_y(t) \end{cases} \quad (4.55)$$

Matching the first two equations and taking the derivatives one gets:

$$\begin{aligned} -\frac{1}{C_1} \cdot \int_0^t i(\tau) d\tau + V_{c1}(0) &= \frac{1}{C_2} \cdot \int_0^t i_x(\tau) d\tau + V_{c2}(0) \xrightarrow{\frac{\partial}{\partial t}} \\ \longrightarrow \frac{1}{C_2} \cdot i_x(t) + \frac{1}{C_1} \cdot i(t) &= 0 \Rightarrow \frac{1}{C_2} \cdot i_x(t) + \frac{1}{C_1} \cdot (i_x(t) + i_y(t)) \\ \xrightarrow{i_y(t) = \frac{V_{c2}(t)}{R}} \left( \frac{1}{C_2} + \frac{1}{C_1} \right) \cdot i_x(t) + \frac{1}{R \cdot C_1} \cdot V_{c2}(t) &= 0 \end{aligned} \quad (4.56)$$

Now, substituting  $V_{c2}(t)$  with an integral form from (4.55) , one obtains a differential equation, similar to the ones previously studied:

$$\begin{aligned} & \left( \frac{1}{C_2} + \frac{1}{C_1} \right) \cdot i_x(t) + \frac{1}{R \cdot C_1} \cdot \frac{1}{C_2} \cdot \int_0^t i_x(\tau) d\tau + V_{c2}(0) = 0 \\ & \xrightarrow{\frac{\partial}{\partial t}} \left( \frac{C_1 + C_2}{C_1 \cdot C_2} \right) \cdot \frac{\partial i_x(t)}{\partial t} + \frac{1}{R \cdot C_1 \cdot C_2} \cdot i_x(t) = 0 \end{aligned} \quad (4.57)$$

The result of this equation is the well-known exponential function:

$$\begin{aligned} & \frac{\partial i_x(t)}{\partial t} + \frac{1}{R \cdot (C_1 + C_2)} \cdot i_x(t) = 0 \xrightarrow{C_{eq}=C_1+C_2} i_x(t) = I_x \cdot e^{-\left(\frac{1}{R \cdot C_{eq}}\right)t} \\ & \rightarrow \text{If } C_2 < 0 \rightarrow C_{eq} = C_1 - |C_2| \Rightarrow \begin{cases} |C_2| < C_1 \rightarrow \text{Stable} \\ |C_2| > C_1 \rightarrow \text{Unstable} \end{cases} \end{aligned} \quad (4.58)$$

However, in this case the net equivalent capacitance is the parallel combination of  $C_1$  and  $C_2$  ( $C_{eq}=C_1+C_2$ ) Therefore, if  $R$  is positive (and it is the case when  $R$  models the input impedance of an instrument) the circuit will be only stable if  $C_{eq}$  is also positive which implies  $C_2 \in \{-C_1, \text{Inf}\}$ . It is important to notice that this behavior is the opposite to that obtained in the previous section (series/parallel  $RC_n/C$  circuit).

Once, one of the variables is known, it is easy to derive all other voltages and currents in the circuit. So, the voltage across  $C_2$  is given by:

$$\begin{aligned} V_{c2}(t) &= \frac{1}{C_2} \cdot \int_0^t i_x(\tau) d\tau + V_{c2}(0) = \frac{I_x \cdot R \cdot C_{eq}}{C_2} \cdot \left[ 1 - e^{-\frac{1}{R \cdot C_{eq}}t} \right] + V_0 \cdot \frac{C_1}{C_1 + C_2} \\ V_{c2}(t \rightarrow \infty) &= 0 \longrightarrow I_x = \frac{-V_0 \cdot C_1 \cdot C_2}{(C_1 + C_2)^2 \cdot R} \end{aligned} \quad (4.59)$$

In addition,:

$$\begin{aligned} i_x(t) &= -\frac{V_0 \cdot C_1 \cdot C_2}{(C_1 + C_2)^2 \cdot R} \cdot e^{-\left(\frac{1}{R \cdot C_{eq}}\right)t} \\ V_{c2}(t) &= V_0 \cdot \frac{C_1}{(C_1 + C_2)} \cdot e^{-\left(\frac{1}{R \cdot C_{eq}}\right)t} \\ i_y(t) &= \frac{V_{c2}(t)}{R} = \frac{V_0}{R} \cdot \frac{C_1}{(C_1 + C_2)} \cdot e^{-\left(\frac{1}{R \cdot C_{eq}}\right)t} \end{aligned} \quad (4.60)$$

It is important to notice that at  $t=t_0$  the charged capacitor instantaneously transfers charge to the second capacitor causing an abrupt change of voltage:

$$V_{c1}(t) = \begin{cases} V_0 & t \leq t_0 \\ V_{c2}(t) = V_0 \cdot \frac{C_1}{(C_1 + C_2)} \cdot e^{-\left(\frac{1}{R \cdot C_{eq}}\right)t} & t > t_0 \end{cases} \quad (4.61)$$

As it was explained before, this phenomenon is a consequence of the presumed dispersionless behavior of an ideal negative capacitor.

Figure 4-38 shows the simulated voltages and currents in this circuit, for different values of  $C_2$ .

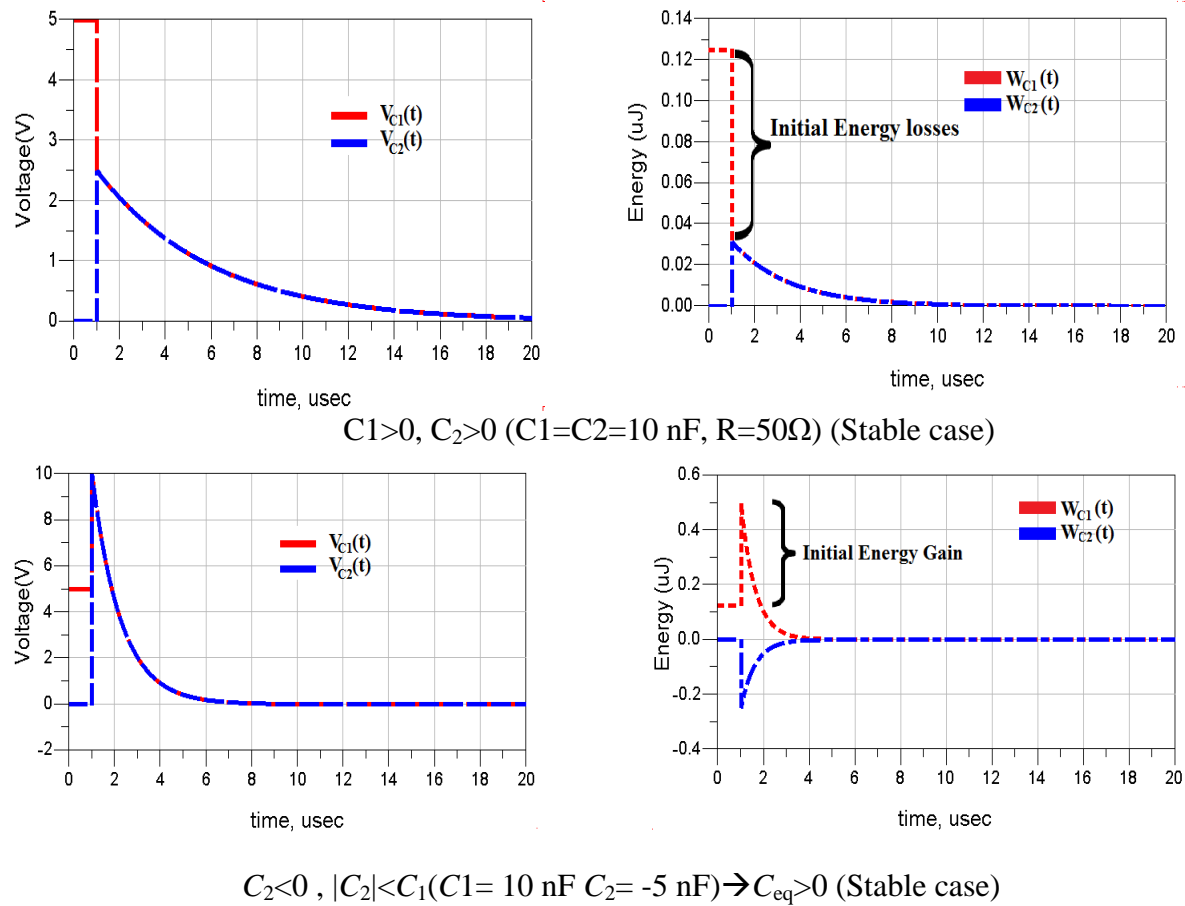


**Figure 4-38** Voltages and currents in parallel  $RCC_n$  circuit with no driving source

Obtained results again perfectly match those from the theoretical analysis. In the upper part of Figure 4-38, it can be observed how the voltage in  $C_1$  drops infinitely fast to the voltage level given by (4.61) when the switch closes. At this moment, both the capacitors discharge simultaneously through the resistor  $R$ . On the other hand, if  $C_2 < 0$  and  $|C_2| < C_1$  (the lower part of Figure 4-38) both the voltage and energy increase. This increase is a consequence of the active nature the negative capacitor. After this initial increase, both capacitors discharge through the resistor  $R$ . Clearly, this is stable behavior.

Finally if  $C_2 < 0$ , and  $|C_2| > C_1$ , the circuit is unstable and the voltages, currents, and energies grow exponentially.

The stability criteria of parallel  $RCC_n$  circuit are summarized in Table 4-6:

$R$	$C_{eq}=C_1+C_2$	Stability
+	+	Stable (if $-C_1 < C_2 < \infty$ )
+	-	Unstable (if $C_2 < 0$ and $ C_2  < C_1$ )
-	-	Stable
-	+	Unstable (if $-C_1 < C_2 < \infty$ )

**Table 4-6** Stability criteria for parallel  $RCC_n$  circuit with no driving source

#### 4.4. Summary

A novel concept of active broadband dispersionless metamaterial based on negative non-Foster reactance has been proposed in this chapter. The brief summary of presented discussion is given below:

- Active non-Foster elements (a negative capacitor and a negative inductor) have dispersion curves that are the exact inverse of the dispersion curves of ordinary ‘positive’ elements. Therefore, the dispersion of ordinary passive metamaterials can be compensated for with the ‘inverse’ dispersion of non-Foster elements, resulting in the broadband behavior.
- A 1D transmission line periodically loaded with shunt  $CC_n$  circuits (providing that  $C > |C_n|$ ) shows stable ENZ dispersionless behavior. A dual circuit (a transmission line periodically loaded with series  $LL_n$  circuits (providing that  $L > |L_n|$ ) shows stable MNZ dispersionless behavior. On the other hand, active ENG and MNG metamaterials (at least those based on simple one-port non-Foster networks) are unstable, so, they do not seem to be feasible.
- It is straightforward to extend the proposed principle of 1D broadband active ENZ and MNZ metamaterials to 2D (both isotropic and anisotropic implementations are possible).
- The most important issue in application of non-Foster networks deals with stability. Widely used frequency-domain methods of stability analysis can give completely wrong predictions in the case of non-Foster networks. Therefore, the stability analysis should be performed in time-domain.
- It has been shown that the stability does not depend only on the active negative elements and its parasitic effects (as it is usually believed), but it also depends on the elements of the external passive network. Different parallel and series networks that contain non-Foster elements have different stability criteria. This fact is almost completely overlooked both in the metamaterial field and in the field of active matching of small antennas.



Chapter 5 TECHNOLOGICAL ISSUES AND EXPERIMENTAL INVESTIGATION

## Technological issues and experimental investigation

### 5.1. NEGATIVE IMPEDANCE CONVERTER (NIC)

Negative non-Foster elements are realized by terminating a two-port called a Negative Impedance Converter (NIC) in the corresponding positive element Figure 5-1). It is, by analogy, a form of an ideal transformer with a ratio of an impedance transformation of  $-k$ . This impedance transformation operates in both directions (bilateral behavior).

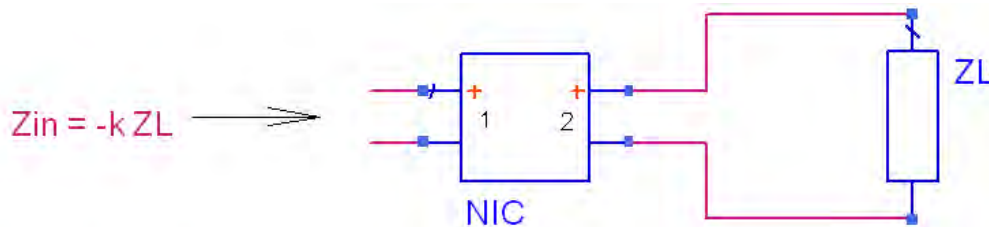


**Figure 5-1** Basic definition of NIC as a two-port network

The first practical transistorized NICs were designed, built and tested by Linvill [30] in 1954. He built negative resistance circuits using both grounded and floating NICs, which initiated many research efforts both in developing of underlying theory and practical devices. Nowadays, NIC circuits are well documented but practical realization is still difficult due to stability problems.

Here, the basic definitions and parameters of NIC circuits are very briefly presented, while the different designs of practical devices together with associated technological issues are reviewed in the chapter 5.2.

#### 5.1.1 Current inverter (INIC)

A simple ways to describe NIC circuit is use of hybrid h-parameters (Figure 5-2) [36].

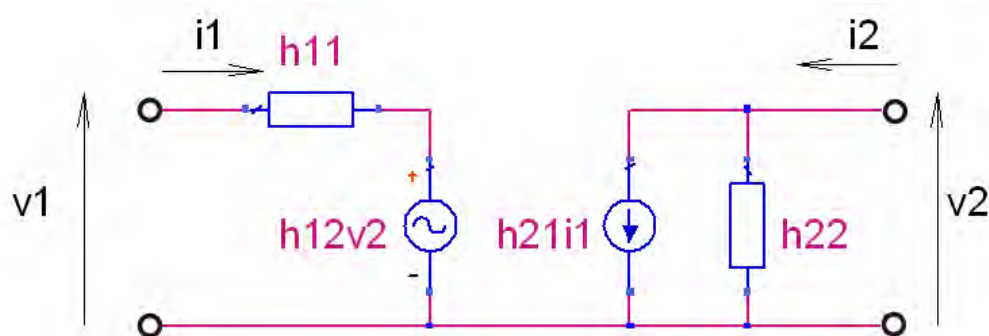


**Figure 5-2** General NIC modeled with h-parameters

The h-parameter model is defined by well-known equations:

$$V_1 = h_{11} \cdot I_1 + h_{12} \cdot V_2 \quad (5.1)$$

$$I_2 = h_{21} \cdot I_1 + h_{22} \cdot V_2 \quad (5.2)$$

If the port 2 is terminated with impedance  $Z_1$ , the input impedance (seen into the port 1) reads as:

$$Z_{in} = \frac{V_1}{I_1} = h_{11} - \frac{k \cdot Z_1}{1 + h_{22} \cdot Z_1}, \quad k = h_{12} \cdot h_{21}. \quad (5.3)$$

Here,  $k$  stands for the conversion ratio [36]. An ideal NIC should have  $k=1$ . Inspection of (5.3) shows that this will be achieved if the following conditions are satisfied:

$$h_{11} = h_{22} = 0, \quad (5.4)$$

$$h_{12} \cdot h_{21} = 1. \quad (5.5)$$

Two basic types of NIC are realizable from (5.4, 5.5) depending on whether current or voltage inversion occurs. The first type is referred to as a current inverter or INIC, and it does current inversion without affecting the polarity of input and output voltages. If the load  $Z_1$  is connected to port 2 (as it is in Figure 5-1) the inversion of one port current generates voltage  $V_1$  that now enforces current flow in the opposite direction such as to oppose the applied voltage (Figure 5-3). Thus, the input impedance is negative while  $I_1=I_2$ ,  $V_1=V_2$ . This can be written in matrix form as:

$$\begin{bmatrix} h_{11} & h_{12} \\ h_{21} & h_{22} \end{bmatrix} = \begin{bmatrix} 0 & 1 \\ 1 & 0 \end{bmatrix}. \quad (5.6)$$

Equation (5.6) defines an ideal INIC.

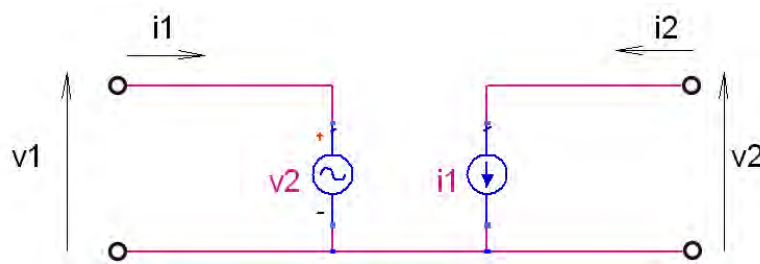


**Figure 5-3** h-parameter model of an ideal INIC

It can be seen that the load voltage  $V_2$  is actually ‘transferred’ to the input port voltage  $V_1$  without change of sign. On the contrary, the input port current  $I_1$  is transferred to the load with reversed sign.

### 5.1.2 Voltage inverter (VNIC)

Another possible way of achieving negative input impedance is to reverse one port voltage leaving polarity of currents unchanged. Thus,  $I_1 = -I_2$ ,  $V_1 = V_2$ , which again leads to a simple matrix equation:

$$\begin{bmatrix} h_{11} & h_{12} \\ h_{21} & h_{22} \end{bmatrix} = \begin{bmatrix} 0 & -1 \\ -1 & 0 \end{bmatrix}. \quad (5.7)$$

The device defined by (5.7) is referred to as a voltage inverter or VNIC (Figure 5-4).

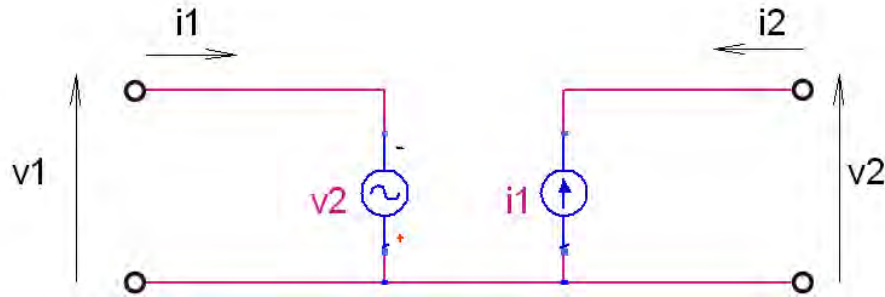


**Figure 5-4** h-parameter model of an ideal VNIC

### 5.1.3 Reducing number of dependent sources in NIC circuits

Basic INIC (Figure 5-3) and VINIC (Figure 5-4) models have two dependent sources. At first sight, this appears impractical. However, these circuits can be reduced to the circuits that use a single dependent source by very simple transformations.

In the case of a basic INIC circuit (Left part of Figure 5-5), the upper input terminal and upper output terminal have equal potentials (referring to the common lower terminals) due to  $V_1 = V_2$ . Thus, it is possible to connect upper input terminal to upper output terminal. The dependent voltage source will be connected in parallel to the dependent current source. In the next step, the voltage source can be dropped out if the current source amplitude is changed to  $2I_1$ . This leaves port voltages and port currents unchanged, thus the circuit in the right part of Figure 5-5 is INIC equivalent circuit that contains single (dependent) current source. Please note that lower terminal of this current source is connected to the common point (ground), thus, a floating source is not needed here.

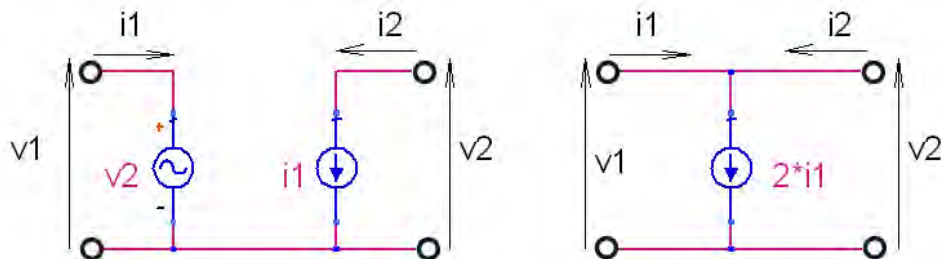


**Figure 5-5** Transformation of basic INIC into with single current source

Very similar approach can be applied to the case of VNIC circuit (Figure 5-6).

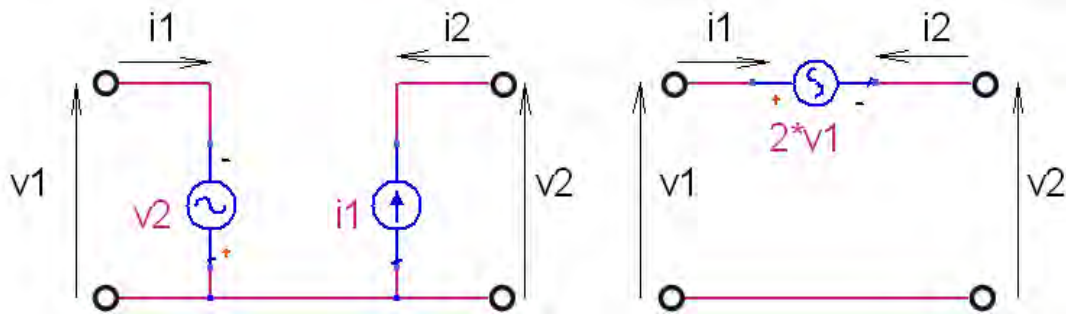


**Figure 5-6** Transformation of basic VNIC into VNIC with single voltage source

Here (left part of Figure 5-6), it is noted that a potential of upper input terminal is equal to the potential of upper output terminal, but with the reversed sign. At the same time, the port currents are equal but they flow in different directions. Due to this, it is possible to drop out the original voltage and current sources and replace them by a single series voltage source with amplitude of  $2V_1$  (right part of Figure 5-6).

The circuit in Figure 5-6 uses a floating voltage source, which would lead to complicated practical realization. Looking from the input terminal, a floating source is connected in series with the load (left part of Figure 5-7). Of course, the input current and voltage will not change if the locations of a voltage source and the load are swapped (right part of Figure 5-7). Here, the voltage source is not floating any more (the lower terminal is connected to the ground).

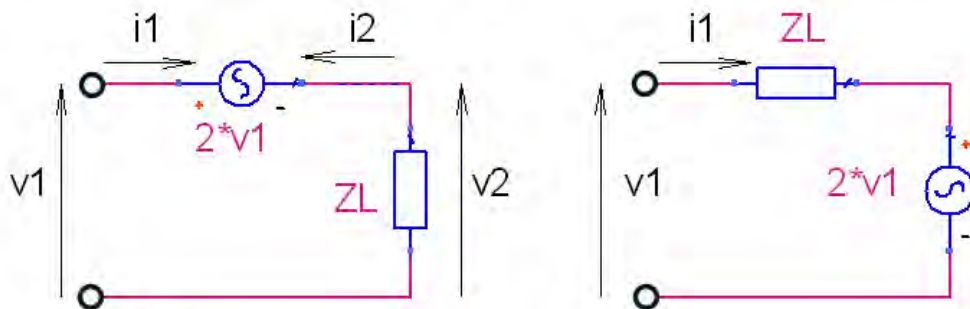


**Figure 5-7** Two possible equivalent circuits of VNIC with single voltage source

#### 5.1.4 Stability of NIC circuit

In chapter 4.3 we developed a simple, but effective theoretical framework for analyzing stability of arbitrary network that contains both positive (passive) and negative (active) non-Foster elements. This approach uses circuit-theory approach with known values of resistance, capacitance and inductance of all elements in the analyzed network (the values of both ordinary passive elements and active non-Foster elements). This approach is exact, quite intuitive, and gives clear physical picture of network behavior.

Another approach is a standard method that divides the NIC circuits into “open-circuit stable” (OCS) and “short-circuit stable” (SCS) types. Practically speaking OCS means, that if a very large resistance terminates the port 1 on NIC, then the overall network will be stable.

Similarly, SCS means that overall network will be stable if a very large conductance is placed across the input. It can be shown that one port of any NIC must always be SCS with the other port being OCS. Linvill [30] suggested that OCS versions should be used only as series elements, while SCS versions should be used as shunt elements. As noted in [34] these conditions are, in fact, a consequence of the Brownlie-Hoskins theorems.

We think that this OCS/SCS approach is (together with some other methods reviewed in [34]) less intuitive and less suitable for analysis of stability of active non-Foster-based metamaterials. Therefore, the above analysis methods are not used in this study.

## 5.2. REVIEW OF SOME COMMON NIC DESIGNS

The selection of particular NIC design depends on the application. Generally speaking, there are two main realizations:

- **Grounded NIC.** One of the terminals of this NIC is connected to ground. This type of NIC is convenient for parallel connection into transmission lines or other circuits that have one common grounded terminal. Grounded NIC can be used for the construction of the broadband active ENZ metamaterial discussed in chapter 4.2. The construction of grounded NIC is usually based on two BJTs (or two FETs) or on one OPAMP.
- **Floating NIC.** The terminals of floating NIC may have different potentials, thus they can be connected to two different points of some network. This NIC is convenient for series insertion into an external network. For instance, floating NIC is needed for the construction of the broadband active MNZ metamaterial discussed in chapter 4.2.2). The construction of floating NIC is significantly more complicated than the construction of grounded NIC.

At the present state of the art, the NIC circuits can be realized in BJT, FET and OPAMP technology. Brief review of available designs is given in the following paragraph.

### 5.2.1. BJT-based circuits

Classical NIC circuits employ two BJTs and they are based on original Linvill's design [30]. These designs are shown in Figure 5-8 [41] and compared in Table 5-1

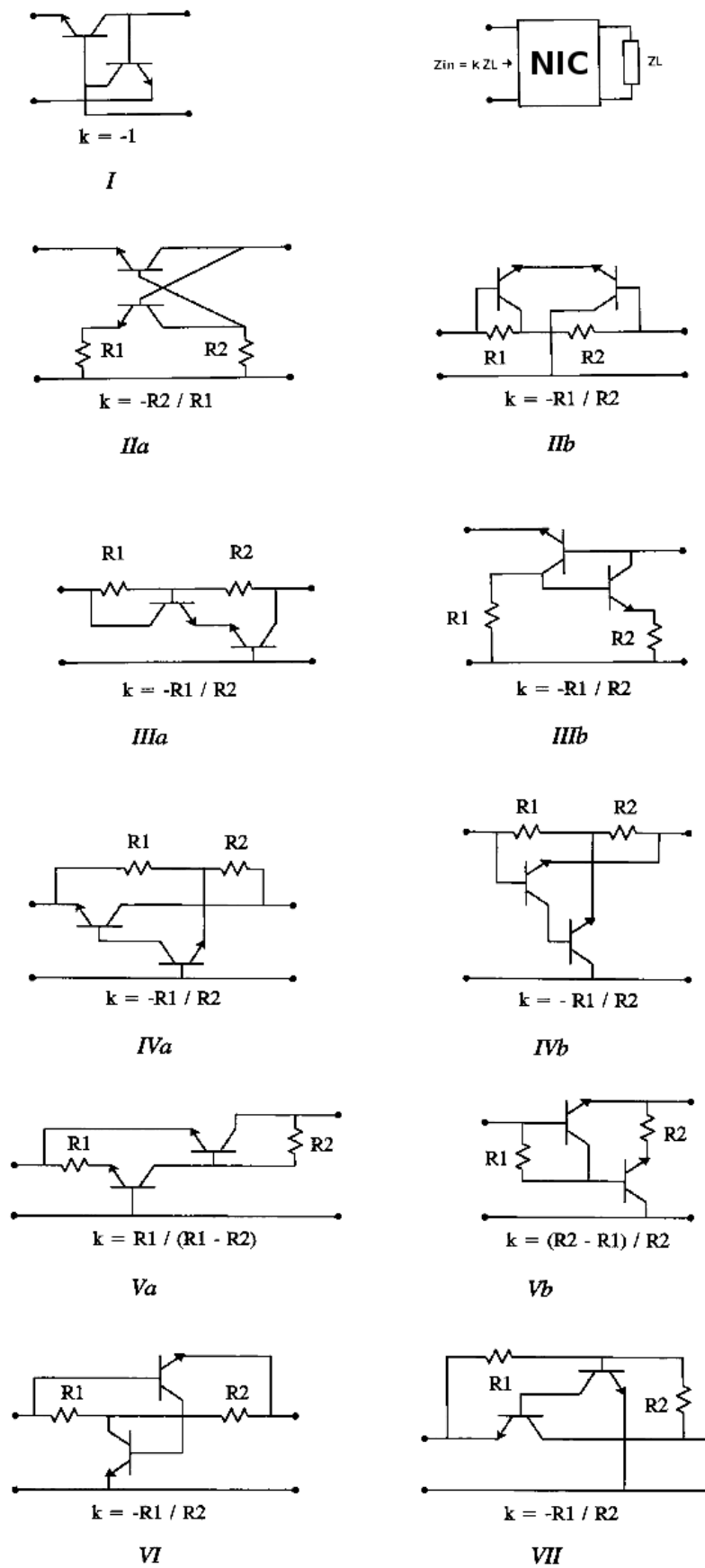


**Figure 5-8** Different designs of NIC circuits with two BJTs (taken from [41])

Circuit No. (Figure 5-8)	Author	Year	Equation for conversion factor $k$ (transistors are assumed to have finite transconductance $g_m$ )
I,IIa	Linvill	1953.	IIa: $k = \frac{1 + g_m R_1 - g_m^2 R_2 R_L}{g_m + g_m^2 R_1}$
IIb,IIIa,IV	Myers	1965.	IIb,IIIa: $k = \frac{2(R_1 + R_2 + R_L) - g_m R_1 R_L}{2 + g_m R_2}$
IIIb	Yanagisawa	1957.	IIIb: $k = \frac{1 + g_m R_2 - g_m^2 R_1 R_L}{g_m + g_m^2 R_2}$
IVa,Va,Vb	Hakim	1965.	Va: $k = \frac{2(R_1 + R_2 + R_L) - g_m R_1 R_L}{2 + g_m R_2}$ Vb: $k = \frac{1 + g_m (R_1 + R_L) - g_m^2 R_1 R_L}{2g_m + g_m^2 (R_1 - R_2)}$
IVb	Larky	1957.	$k$ does not depend on $g_m$
VII	Nagata	1965.	$k$ does not depend on $g_m$

**Table 5-1** Comparison of different designs of NIC with two BJT

All the circuits from Table 5-1 would operate equally well if they used the ideal transistors. However, one could expect significant differences in performances of practical realizations. Simulations in [41] revealed that only circuits IVa, IVb, VI and VII (Figure 5-8) do not depend on finite values of transconductance  $g_m$ . All other designs require (unrealistic) infinite value of  $g_m$  for achieving required conversion factor  $k$ .

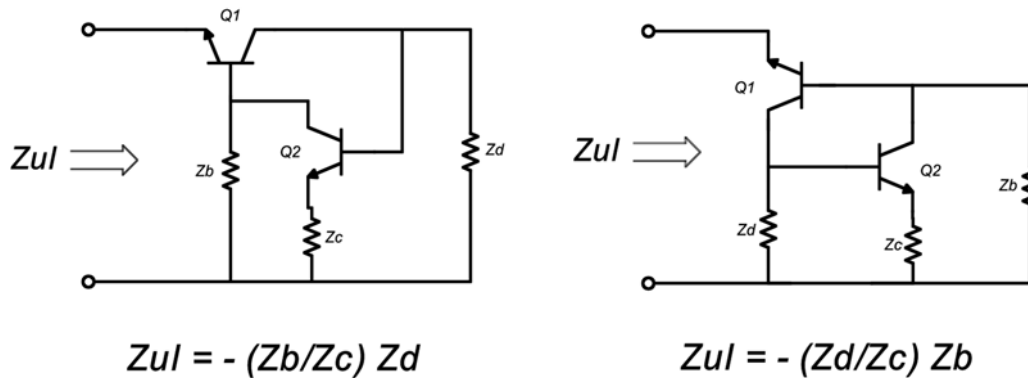


**Figure 5-9** Operation of Linvill (left) and Yanagisawa (right) NIC circuits

Among all the circuits shown in Figure 5-8, only the designs proposed by Linvill (I,IIa) and Yanagisawa (IIIb) have been used in practical applications so far. These two circuits are actually the same, which can be seen from Figure 5-9. The basic principle of operation is briefly explained below (Using Linvill's variant of a circuit shown in the left part of Figure 5-9):



- Input current flows into emitter electrode of Q<sub>1</sub>. Approximately the same current (neglecting a base current of Q<sub>1</sub>) flows out of collector electrode. This collector current produces a voltage drop across the load impedance  $Z_d$ .
- The voltage across  $Z_d$  is amplified by Q<sub>2</sub> (operating in CE configuration) that introduces a phase shift of 180 degrees.
- Amplified (output) signal is superimposed to input signal (across  $Z_b$ ). These two signals have (in ideal case) the opposite signs (due to the phase difference of 180 degrees)
- Voltage drop across  $Z_b$  is equal to the voltage at input port (with neglected  $h_{12}$  parameter of Q<sub>1</sub>).

Voltage gain of Q<sub>2</sub> (operating in CE configuration) is given by

$$A = -\frac{Z_b}{Z_c} \quad (5.8)$$

If  $Z_b = Z_c$ , voltage gain  $A = -1$ , thus the voltages across  $Z_b$  and  $Z_d$  are equal and these voltages have opposite signs. In addition, the currents flowing through  $Z_b$  and  $Z_d$  are approximately equal. Therefore, the input impedance is a negative replica of a load impedance ( $Z_{in} = -Z_d$ ).

As it will be shown in detail in chapter 5.3.1, the main drawback of BJT-based NIC circuit is rather complicated DC bias network. It is extremely difficult to build broad-band chokes (or bias TEEs). On the other hand, a transistor must have high  $f_T$  (our experimental investigation revealed that the  $f_T$  should be at least ten times higher than  $f_{max}$ ,  $f_{max}$  being the maximal operating frequency of NIC). So, non-ideal bias network may cause unwanted oscillations (instability) at high frequencies. Conversely, due to biasing requirements, transistors are DC decoupled, thus the circuits contains the coupling capacitors. Due to the finite value of the capacitance, this may cause stability problems at very low frequency. Taking everything into account, it appears that is very difficult to built BJT-based NIC that operates above 100 MHz. Very recent practical implementation (negative capacitor for active matching of a short dipole antenna) with several embedded stabilizing networks reported in [34] operated in the frequency range 20 MHz to 100 MHz. Within this range, the achieved negative capacitance varied between -40 pF and -70 pF.

### 5.2.2. FET-based circuits

NIC circuits with two FETs are basically rather similar to the associated BJT designs. The main difference is that FET is a transconductance element (thus, the output current is controlled by the input voltage) while BJT is a pure current amplifier. In some FET-based NICs, the 'conversion' of input voltage into the output current also transforms impedance  $Z_L$  into  $1/Z_L$ , thus the inductive reactance is transformed into the capacitive reactance and vice versa. Another important issue is the construction of DC bias network, which is in FET-based NIC significantly simpler comparing to BJT-based circuits.

A typical example of FET-based NIC is Meunier's NIC [41] (Figure 5-10) (the same design was used in its microelectronic version in [59]). Input impedance of the circuit is given by:

$$Z_{in} = \frac{V_1}{I_1}, \quad (5.9)$$

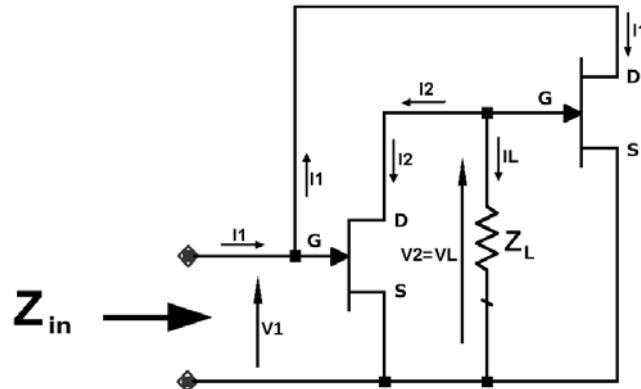


Figure 5-10 Meunier's NIC

while the load impedance reads as:

$$Z_L = \frac{V_L}{I_L} . \quad (5.10)$$

The transconductances of the transistors  $M_1$  and  $M_2$  are given by:

$$g_{m1} = \frac{I_2}{V_1}, g_{m2} = \frac{I_1}{V_2} . \quad (5.11)$$

From (5.9) and (5.10) one gets:

$$Z_{in} = \frac{V_1}{I_1} = \frac{\frac{I_2}{g_{m2}}}{g_{m1} \cdot V_2} = \frac{1}{g_{m1} g_{m2}} \frac{I_2}{V_2} \quad (5.12)$$

Taking into account that  $V_L = V_2$  and the currents  $I_2$  and  $I_L$  flow in opposite directions, one finds the relationship between  $V_2$  and  $I_2$ :

$$Z_L = \frac{V_L}{I_L} = -\frac{V_2}{I_2} \Rightarrow \frac{I_2}{V_2} = -\frac{1}{Z_L} . \quad (5.13)$$

By insertion of (5.13) into (5.12) one finally derives the expression for the input impedance:

$$Z_{in} = -\frac{1}{g_{m1} g_{m2} Z_L} \quad (5.14)$$

There are three important conclusions that can be drawn from (5.14):

1. Input impedance is negative, thus the circuit indeed behaves as NIC.
2. The load impedance is transformed into its inverse ( $1/Z_L$ ) at the input. Therefore, if one wants to achieve a negative capacitor a load must be an inductor (and vice versa). This is a unique property of FET-based NICs (or, more precisely, of NICs based on

transconductance elements). From technological point of view, the use of inductors may be awkward (especially in an microelectronic implementation, if a value of the required inductance is high).

3. The input impedance depends on the transconductances of used transistors. This appears to be a significant drawback of the design in discrete implementation because it is difficult to control value of  $g_m$  (it depends on  $I_D$ ). In the microelectronic implementation, the transconductance can be controlled by a proper choice of FET dimensions or by active biasing techniques.

A microelectronic version of negative capacitor based on this circuit [58] generated capacitance of -1pF within the frequency range 1GHz to 5GHz, which is a very good result. We used similar design and managed to produce stable negative capacitance of -50 pF both in low (20 MHz-80 MHz) and high (1 GHz – 2 GHz) RF bands (see chapter 5.3). These are also very good results, especially taking into account that the whole circuit (as well as all other circuits in this report) was ‘hand-crafted’.

As second example of FET-based NIC is very recent design shown in Figure 5-11.

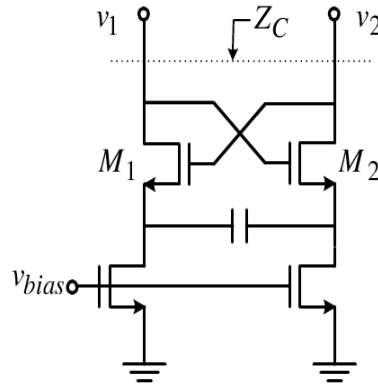


**Figure 5-11** Floating NIC with two FET's

This is a floating type of NIC, which has been used for decreasing of the input capacitance of microwave amplifiers [60] and in the construction of inductorless integrated oscillator [61]. It resembles a relaxation oscillator (without cross-capacitors) and it inverts the impedance connected between the source electrodes of two FETs. It is interesting that this very recent and popular design is actually a modern version of one of the first vacuum-tube-based NICs proposed back in 1951 [62]. An approximate equation for input impedance [60] is given by:

$$Z_{in} \approx -\frac{1}{j\omega C} \frac{g_m + j\omega(C_{gs} + 2C)}{g_m}, \quad \omega \ll \omega_t. \quad (5.15)$$

Here,  $C$  is the load capacitance and  $C_{gs}$  stands for the internal capacitance between gate and source electrodes. This circuit is used exclusively in microelectronic version, which allows extremely broad operating bandwidth (a prototype reported in [60] used 180 nm CMOS technology and generated capacitance of -60 fF in the frequency range 100 MHz – 1.9 GHz). It could be even possible to extend the operating frequency up to more than 20 GHz using modern 90 nm technology. This circuit seems to be a very good candidate for application in proposed active ENZ or MNZ metamaterial. The only possible drawback might be the low

value of generated negative capacitance (or inductance). However, this needs further investigation.

### 5.2.3. OPAMP-based circuits

NIC circuits can also be realized using technology of operational amplifiers (OPAMP).

The basic idea of grounded NIC (type A that uses an inverting input as the input impedance port) is shown in Figure 5-12.

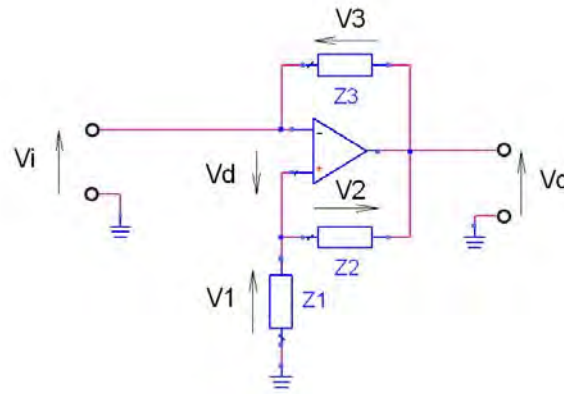


**Figure 5-12** OPAMP-based NIC, type A

This circuit can easily be analyzed by KCLs and KVLs:

$$V_i + V_d - i_2 \cdot Z_1 = 0, \quad (5.16)$$

$$V_i + i_i \cdot Z_3 - V_o = 0, \quad (5.17)$$

$$V_o - i_2 \cdot (Z_1 + Z_2) = 0, \quad (5.18)$$

$$V_d + i_i \cdot Z_3 - i_2 \cdot Z_2 = 0, \quad (5.19)$$

$$V_o = A(f) \cdot V_d. \quad (5.20)$$

Here,  $A(f)$  denotes an inherent OPAMP open-loop gain. By solving the system of equations (5.16-5.20) one derives the expression for the input impedance:

$$Z_i = \frac{V_i}{i_i} = \frac{(Z_1 - A(f) \cdot Z_1 + Z_2) \cdot Z_3}{Z_1 + Z_2 + A(f) \cdot Z_2}. \quad (5.21)$$

If the open-loop gain  $A(f)$  is high enough, (5.21) can be simplified to:

$$Z_i = -\frac{Z_1 \cdot Z_3}{Z_2}. \quad (5.22)$$

It can be seen (5.22) that the sign of the impedance  $Z_3$  will be reversed while the ratio  $Z_1/Z_2$  is the conversion factor  $k$ . This type of OPAMP NIC will be referred to as A1.

Another (equally valid) interpretation of (5.22) can be that a sign of the impedance  $Z_1$  is reversed while a ratio  $Z_3/Z_2$  is the conversion factor  $k$ . This type of OPAMP NIC will be

referred to as A2. Thus, there are two possible locations of the impedance that should be converted) in type A of OPAMP-based NIC. In other words the load can be either impedance  $Z_3$  or impedance  $Z_1$ ).

Another possible design of grounded NIC (type B that uses a non-inverting input for the input impedance port) is shown in Figure 5-13.

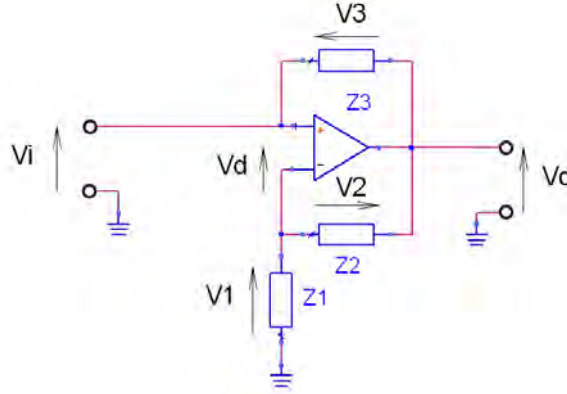


**Figure 5-13** OPAMP-based NIC, type B

KCLs and KVLs of the circuit are:

$$V_i - V_d - i_2 \cdot Z_1 = 0, \quad (5.23)$$

$$V_i - i_1 \cdot Z_3 - V_o = 0, \quad (5.24)$$

$$V_o - i_2 \cdot (Z_1 + Z_2) = 0, \quad (5.25)$$

$$V_d - i_1 \cdot Z_3 - i_2 \cdot Z_2 = 0, \quad (5.26)$$

$$V_o = A(f) \cdot V_d. \quad (5.27)$$

By solving the system of equations (5.23-5.27) one finds an expression for input impedance:

$$Z_i = \frac{V_i}{i_i} = \frac{(Z_1 + A(f) \cdot Z_1 + Z_2) \cdot Z_3}{Z_1 + Z_2 - A(f) \cdot Z_2}. \quad (5.28)$$

If the open-loop gain  $A(f)$  is high enough, (5.28) can be simplified to:

$$Z_i = -\frac{Z_1 \cdot Z_3}{Z_2} \quad (5.29)$$

Again, there are two possible interpretations of (5.29). In the first one, a sign of the impedance  $Z_3$  is assumed to be reversed while a ratio  $Z_1/Z_2$  is the conversion factor  $k$ . This type of OPAMP NIC will be referred to as B1 (impedance  $Z_3$  is the load).

In the second interpretation of (5.21), a sign of the impedance  $Z_1$  is assumed to be reversed while a ratio  $Z_3/Z_2$  is the conversion factor  $k$ . This type of OPAMP NIC will be referred to as B2 (impedance  $Z_1$  is the load).

All four types of OPAMP-based NIC should behave equally well if the OPAMP is ideal with the infinite value of open-loop gain  $A(f)$  (as it is quite often assumed in many textbooks

and active filter ‘cookbooks’). However, in possible application in active metamaterials, one wants to achieve maximal frequency of operation that is in RF range. Therefore, one must account for all the imperfections.

Using a commercial circuit-theory simulator [63], we simulated all four types of NICs using a simple one-pole model of OPAMP. We used typical parameters of realistic high-speed OPAMP:

- $A=80$  dB
- $f_{\text{pole}}=0.1$  MHz
- $\text{GWB}=1$  GHz
- $R_{\text{in diff}}=1$  M $\Omega$
- $R_{\text{in com}}=1$  M $\Omega$
- $R_{\text{out}}=1$   $\Omega$
- Slew rate  $=10^{12}$  V/s

The test cases were negative capacitor circuits (Figure 5-14, Figure 5-15, Figure 5-16, Figure 5-17). Simulated input resistance and input capacitance are shown in Figure 5-18 and Figure 5-19, respectively.

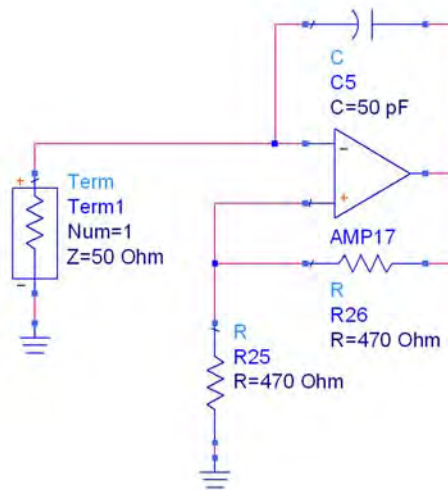


**Figure 5-14** Negative capacitor circuit based on A1 type of NIC

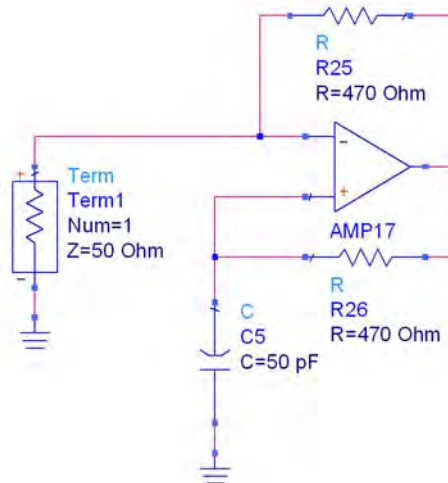


**Figure 5-15** Negative capacitor circuit based on A2 type of NIC

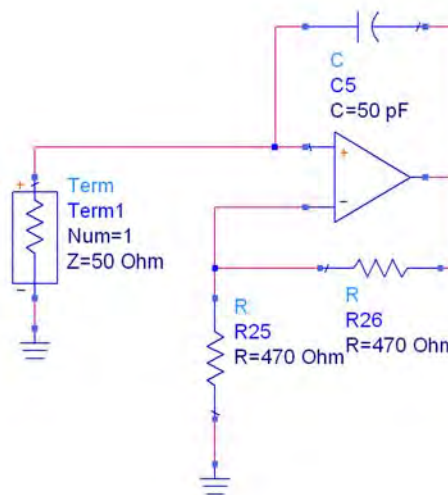


**Figure 5-16** Negative capacitor circuit based on B1 type of NIC

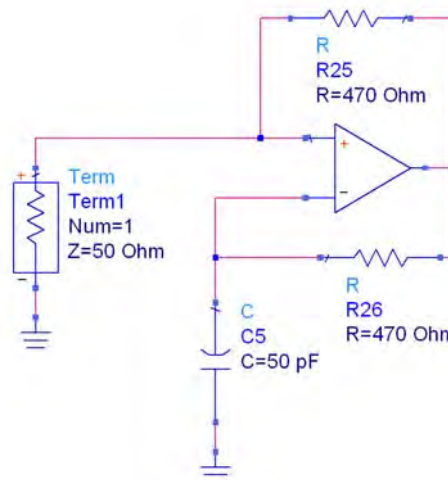


**Figure 5-17** Negative capacitor circuit based on B2 type of NIC

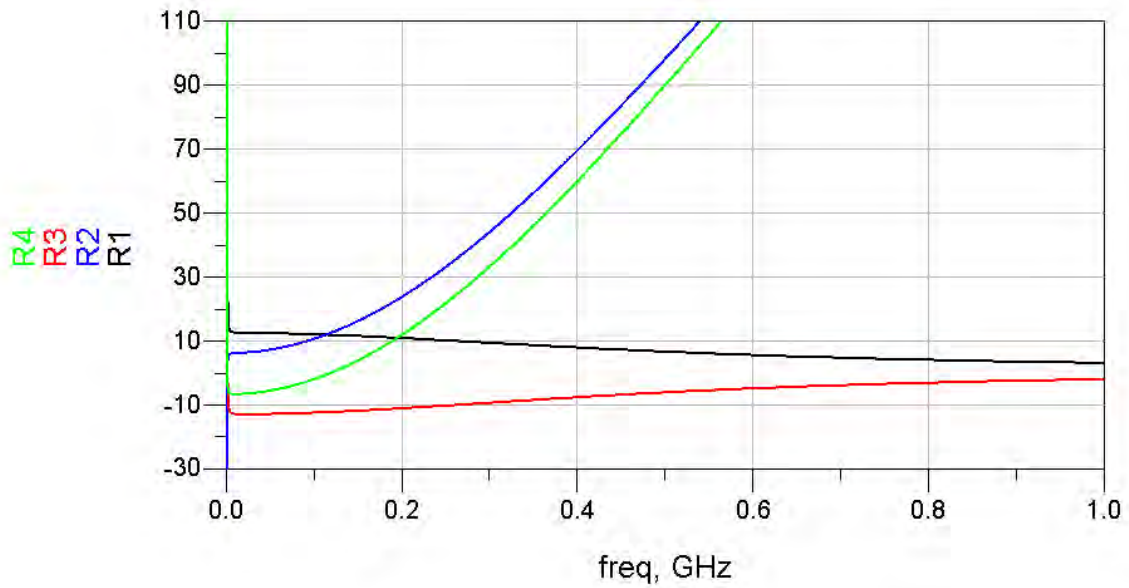


**Figure 5-18** Input resistance of negative capacitor OPAMP-based NICs,  $R_1$  (green) -type A1,  $R_2$  (red)-type A2,  $R_3$  (blue)-type B1,  $R_4$  (black)-type B2,

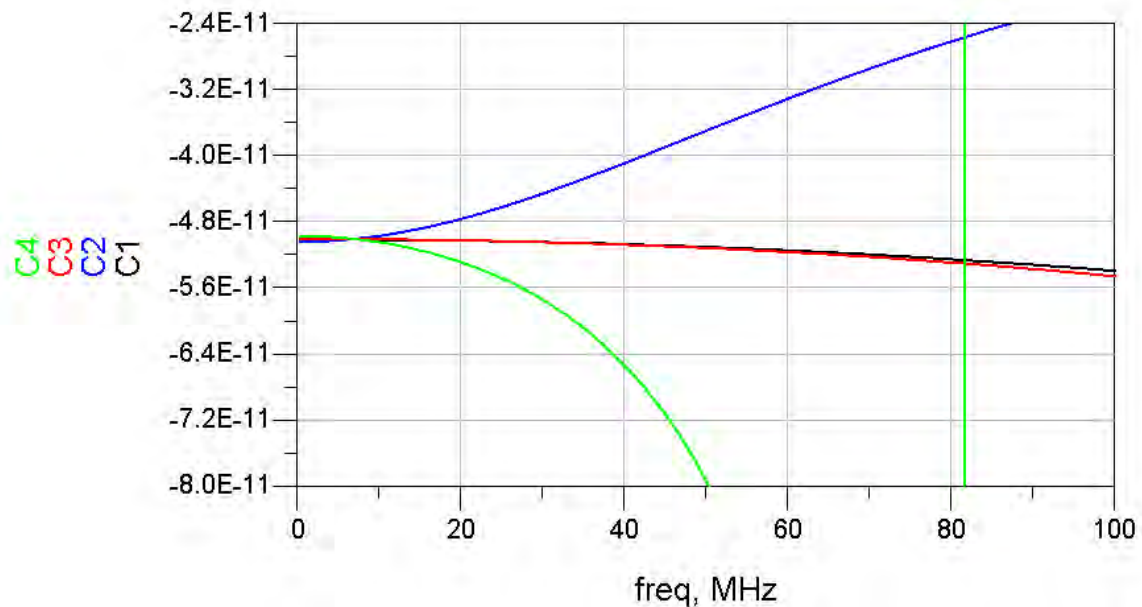


**Figure 5-19** Input capacitance of negative capacitor OPAMP-based NICs,  $C_1$  (black)-type A1,  $C_2$  (blue)-type A2,  $C_3$  (red) -type B1,  $C_4$  (green) -type B2,

All four types of NIC behave well from DC up to approximately 10 MHz: generated negative capacitance is almost constant ( $\sim 50$  pF) and the input resistance is smaller than  $15 \Omega$  (it has positive sign for types A1 and A2 and negative sign for types B1 and B2). Types A1 and A2 maintain almost 'flat' dispersion curve of generated capacitance up to 100 MHz. On the contrary, the generated capacitance varies rather significantly above 20 MHz for types B1 and B2. The input resistance does not change significantly up to 1 GHz for types A1 and B1, while the change of input resistance is rather pronounced for types A2 and B2.



The simulations were performed with OPAMP model, a gain-bandwidth product (GBW) of which was 1 GHz while some of the best state of the-art devices have this figure higher than 3 GHz. Even by taking these best performance figures into account, it seems that the highest operating frequency of OPAMP-based NIC circuits is still limited to approximately 100 MHz. Nevertheless, the OPAMP-based NIC circuits are very simple, so they can be very useful for proof-of-concept demonstrators of active metamaterials in lower RF range.

#### 5.2.4. Comparison of analyzed technologies of NIC fabrication

All analyzed technologies are briefly compared in Table 5-2.

Technology	Design complexity	Maximal experimentally demonstrated operating frequency		‘hand-craft’ prototyping
		discrete version	integrated version	
BJT	high	~100 MHz [34]	?	very difficult
FET	medium	~2GHz [this report]	5 GHz [37]	difficult
OPAMP	low	~ 50 MHz [this report]	?	simple

**Table 5-2** Comparison of analyzed technologies of NIC fabrication

It should be noted that the reported maximal frequencies are those available in public. Recently, there have been several conference reports with maximal achieved frequencies of 400 MHz using BJT technology and more than 10 GHz using integrated CMOS FET technology. However, design details of these efforts are not available in public and they cannot be cross-checked. Therefore, these results are not included in Table 5-2.

### 5.3. EXPERIMENTAL RF (50-100 MHz, 1-2 GHz) 2D UNIT CELLS OF ACTIVE ENZ MTM

After the theoretical investigation discussed in the previous chapters, it was decided to verify the basic principles of proposed novel active broadband metamaterials experimentally. A concept of active ENZ metamaterial (chapter 4.2.1) was chosen for this verification. The reason is the inherent simple equivalent circuit of an ENZ cell (right part of Figure 4-1). This circuit requires only one grounded negative capacitor (on the contrary, an MNZ unit cell requires a floating negative inductor). In the previous discussion it was highlighted that parasitic capacitances and inductances may significantly influence operation of practical non-Foster elements (due to the inherent positive feedback, which is very sensitive to an additional phase shift). Effective way of minimizing this influence is miniaturization, i.e. use of the microelectronic technology. Since this technology was not at our disposal (all reported prototypes were ‘hand-crafted’), it was decided to initially limit the operating frequency to 2 GHz.

The first attempts were focused on building a stable grounded negative capacitor in RF range. We performed a numerical analysis of all designs presented in chapter 5.2 using ADS<sup>TM</sup> circuit simulator [63] and SPICE models of commercially available BJTs and FETs. As the most important result, it was found that the transit frequency ( $f_T$ ) of the active element should be significantly higher than the required highest operating frequency of the negative capacitor. As the rule of thumb, one could say that the transit frequency should be at least ten

times higher than the maximal operating frequency. This comes from a very simple fact that the operation of all NIC circuits is based on either voltage or current inversion. The inversion requires a phase shift of exactly 180 degrees between the input and the output of the active device. This phase shift can be achieved only at very low frequencies, for which the transit time across the active device can be neglected. The drawback of the high transit frequency is that it makes the circuit more prone to unwanted oscillations due to unavoidable parasitic capacitances and parasitic inductances within the circuit. This problem can be relaxed by the addition of a frequency-dependent negative feedback to each active element. Such a feedback contains resistive loading that actually decreases the transit frequency, and at the same time maintains the required 180 degrees phase shift at the operating frequency.

The lower cut-off frequency of the negative capacitor circuit is associated with the coupling capacitors between the active elements. At first sight, it would appear beneficial to decrease the lower cut-off frequency (and therefore increase the operating bandwidth) by choosing high values of coupling capacitors. However, it was found that this method very often introduces low frequency instabilities due to higher gain of the active element at lower frequencies. As mentioned before, we have found that classical stability analysis that uses the Rollet stability factor (also implemented in ADS<sup>TM</sup> [63]) is inconvenient and unreliable for the prediction of stability of negative capacitances. Therefore, we implemented an approach that adds an ideal circulator to the circuit [49] and evaluates stability using the Nyquist criterion.

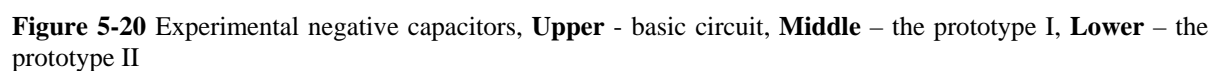
The next important issue is the trade-off between BJT and FET technology. All the circuits discussed in chapter 5.2 are ‘true-type’ NICs. It means that the input impedance is scaled load impedance with the negative sign ( $Z_{in} \sim -Z_{load}$ , with  $Z_{in}$  and  $Z_{load}$  being input and output impedances, respectively). Practically speaking, for obtaining negative capacitance one would need a simple capacitive loading of the NIC circuit. Conversely, the FET-based circuit presented in [41,59] actually produces the reciprocal of the load impedance ( $Z_{in} \sim 1/Z_{load}$ ). Thus, for obtaining negative capacitance one would need the inductive loading. As highlighted in chapter 5.2, this may be impractical.

The last important issue deals with the losses of the negative capacitance. Generally speaking, FET-based circuits have lower losses due to the inherent reactive behavior of the input impedance [41] (locus of parameter  $S_{11}$  is close to the edge of the Smith chart).

It can be seen that the design of stable negative capacitance for an active ENZ metamaterial is a rather complex and challenging task. After performing a lot of simulations and comparing pros and cons of different designs, it was decided to use the FET-based Meunier’s circuit (Figure 5-10, [41,59]).

### 5.3.1 Development and testing of FET-based negative capacitors

Meunier’s circuit (Upper part of Figure 5-20) is extremely simple and its only drawback is the use of a lumped inductance. Two prototypes in FET technology intended for operation in the RF band (50 MHz – 100 MHz) and the lower microwave band (1 GHz - 2 GHz) were manufactured and measured [65,66,67,68]. The RF circuit (prototype I) employs four BF999 Si MOS FETs while the microwave circuit (prototype II) is based on two MGF1412 GaAs FETs. As the load impedance, high quality chip inductors (CoilCraft<sup>TM</sup>) were used. As it can be seen in the middle part of Figure 5-20, the actual realization of RF prototype is more complex than a basic circuit. At first, during the prototyping it was found that simple passive DC bias networks are not convenient since their finite reactance caused instabilities (oscillations).



Therefore, active DC bias with two additional FETs (BF999) was used. In addition, it was found necessary to add and optimize several additional elements ( $R_{31}$  and  $C_{32}$ ) to compensate for negative input resistance and input inductance caused by imperfections of used FETs.

The biasing problem was even more pronounced in the case of the prototype II. It was found impossible to construct a passive network that would assure stable operation. On the other hand, the active network based on the same FETs (MGF1412) showed instabilities. This is not surprising since  $f_T$  of used transistors is rather high (26 GHz). At the same time, the length of the shortest track on the bias part of PCB was a significant fraction of the wavelength (approximately 3mm). This was inevitable, due to lack of space limited by the dimensions of other SMD components. Therefore, two external professional miniature K microwave bias tees (intended originally for network analyzer measurements of active planar devices in frequency range 1 MHz -40 GHz) were used for connecting the DC bias ( $V_1=9V$ ,  $V_2=12V$ ). This 'ad hoc' method assured stable operation (obviously, the final fabrication of prototype II should use microelectronic technology that avoids experienced biasing problems). The circuits were assembled on a double-clad substrate (the 1,6 mm thick FR4 substrate with  $\epsilon_r=4.3$  for prototype I and the 0.6 mm thick Taconic<sup>TM</sup> substrate with  $\epsilon_r=2.2$  for prototype II). The footprint of the layout was roughly 25 mm x 20mm for both prototypes. The photographs of the prototypes are shown in Figure 5-21.

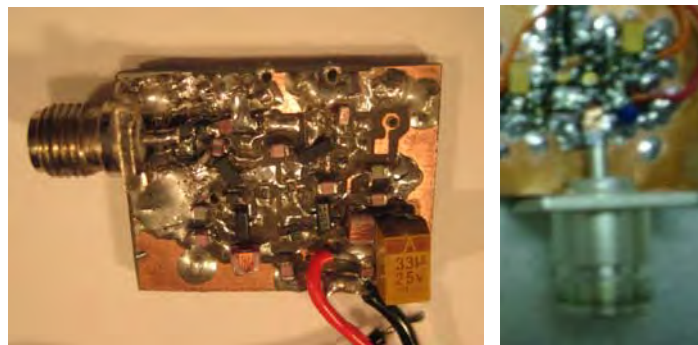


**Figure 5-21** Photos of experimental negative capacitors, **Left** – the prototype I, **Right** – the prototype II

Direct measurement of the equivalent negative capacity is a rather difficult problem, due to the inherent instability of the ideal negative capacitor. In order to avoid this difficulty, one may use a simple approach based on a parallel combination of an ordinary (positive) capacitor and a NIC-based negative capacitor [32,34,59]. Since the overall capacitance is positive, the circuit is stable and the input reflection coefficient (and the input impedance) can be measured using standard techniques. After this is done, one simply subtracts the value of the positive capacitance from the overall capacitance. Following this approach, the input impedance of the prototyped negative capacitors was measured with the help of ZVA 40 Rohde Schwartz network analyzer, and the obtained results are shown in the Smith chart in Figure 5-22. It can be seen that both prototypes clearly show non-Foster behavior (locus of input impedance rotates counter-clockwise with frequency) within a very broad band (more than two octaves). It can also be seen that the impedance loci of both circuits are located very close to the edge of the Smith chart at lower frequencies. However, the loci move toward the centre of the chart with increasing frequency, indicating an increase in the losses. So, we have set (completely arbitrarily) the maximal imaginary part of the input impedance to 25 ohm ( $Z_0/2$ ,  $Z_0$  being the system characteristic impedance) as the bound of operating bandwidth. By

accepting this, one finds that prototype I generates capacitance between -10 pF and -15 pF for frequencies between 50 MHz and 120 MHz, while prototype II generates capacitance between -15 pF and -20 pF within the band 1 GHz to 2.5 GHz. So, the dispersion bandwidth (DBW) of at least one octave is clearly feasible.

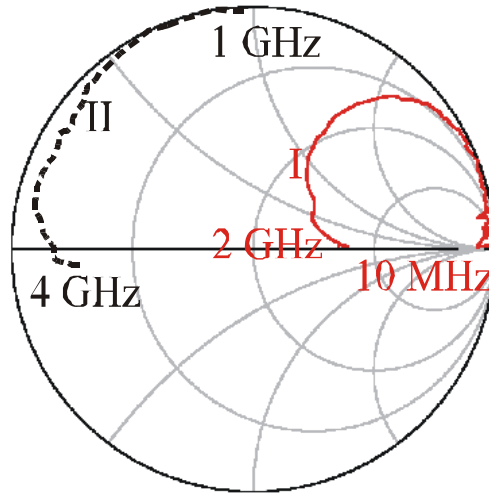


**Figure 5-22** Measured input impedance of experimental negative capacitors (solid - the prototype I, dashed- the prototype II)

### 5.3.2 Development and testing of 2D unit cell of ENZ metamaterial

In the next step, two different 2D unit cells of active ENZ metamaterials were assembled. Each cell comprised two mutually perpendicular electrically short microstrip lines ( $< \lambda/20$ ,  $\lambda$  being the guiding wavelength) (Figure 5-23) forming a cross on a 25mm x 25 mm substrate.

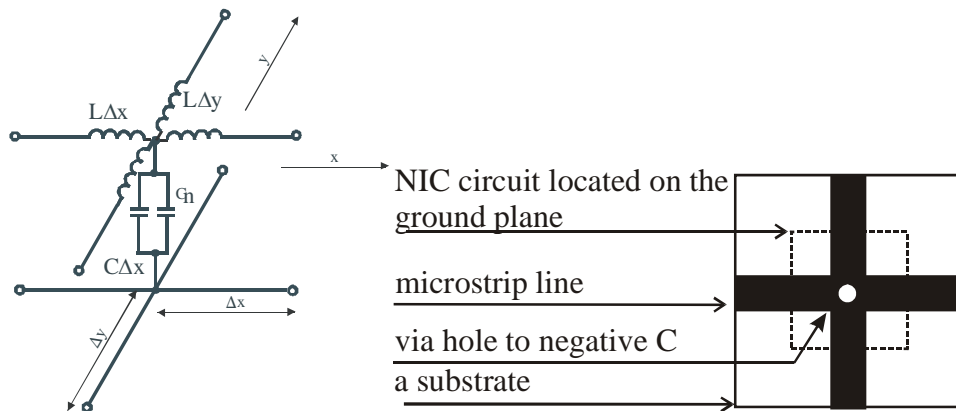


**Figure 5-23** 2D unit cell of an active ENZ metamaterial, **Left** – equivalent circuit, **Right** - A sketch of realized unit cell

The prototyped active capacitance circuit was back-to-back mounted on the ground plane and connected to the junction of the microstrip lines through a via hole. Following (4.5), the parameters of the microstrip lines were chosen in such a way that the generated negative capacitance partially cancelled the distributed line capacitance. So, one expects to

obtain the equivalent permittivity of the unit cell smaller than one. The equivalent permittivities of these unit cells, extracted from the measured results, are shown in Figure 5-24.

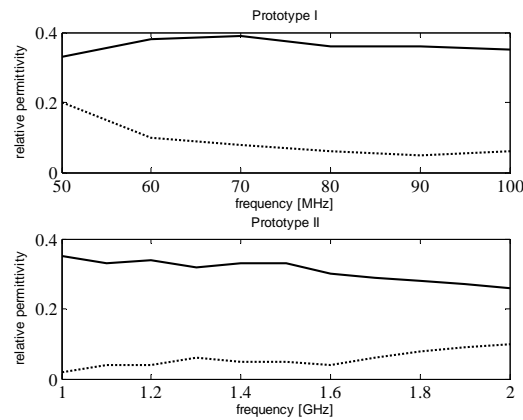


**Figure 5-24** Measured relative permittivity of unit cells (solid –real part, dashed – imaginary part)

It can be seen that in both cases, the permittivity is fairly constant within one octave (50 MHz – 100 MHz for prototype I and 1GHz - 2GHz for prototype II ).

### 5.3.3 Demonstration of possible application in broadband plasmonic cloaking

The next step should be the prototyping of an entire 2D active plasmonic cloak. However, a simple calculation reveals that such a cloak (the active version of the original passive cloak from [12]) would have approximately 350 unit cells within the plasmonic coating. The prototyping of this cloak would be an extremely difficult, costly and time-consuming process. Therefore, a different way of verification of the broadband cloaking was chosen. The ADS<sup>TM</sup> [63] model of a cloak (Figure 5-25) was developed.

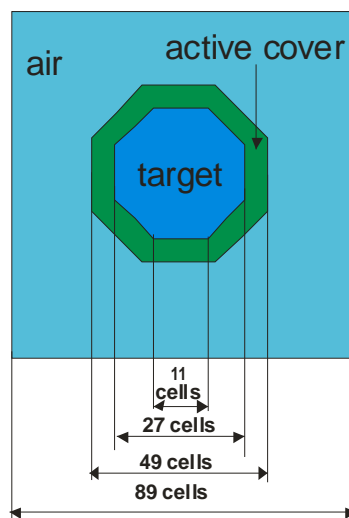


**Figure 5-25** A sketch of ADS<sup>TM</sup> model of active cloak

The model uses ordinary circuit theory approach, widely used in metamaterial community [3]. It comprises a grid of 89 x 89 unit cells, terminated along all four sides with matching resistors (Bloch impedances). Air was simulated using ordinary 2D transmission lines. The object (target) in the original passive plasmonic cloak [1] may be a dielectric cylinder or a PEC cylinder. Here, the results for the dielectric cylinder, parameters of which (the ratio between radii of a cloak and a target of 1.8 and the relative permittivity of the target of 2) have been taken from numerical example in [69]. The cylinder was approximated with a polygon, the width of which is 27 cells, and it was simulated as a grid of 2D transmission lines. The parameters of the transmission lines were chosen in order to achieve the permittivity of the target presented in [69]. The active cover was 11 cells thick and the parameters of each unit cell were derived from the measurement results of the prototyped active unit cell II at the given frequency. The cloak was illuminated with a small dipole, simulated as a simple voltage source. Of course, one must be aware that this approach completely neglects possible EM coupling between different active unit cells, which might take place in a real situation. Once the model was set, the distribution of node voltages (corresponding to the distribution of the electric field) was calculated across the entire model. This procedure was repeated for 10 discrete frequency points in the band from 1GHz to 2 GHz. A sample of the obtained results, showing the distribution of the magnitudes of the node voltages for a bare target and a target with a cloak, at the central frequency of 1.5 GHz, is shown in Figure 5-26.

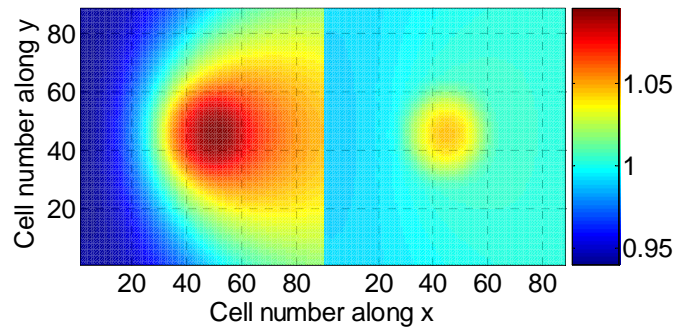


**Figure 5-26** Computed normalized voltage distributions of all unit cell nodes in the ADS TM model of a bare target (**left**) and a target with an active cover (**right**).

It can be seen that an active cover reduces scattered field to almost negligible value, which clearly proves the cloaking mechanism. Very similar results were obtained across the whole band from 1 GHz to 2 GHz.

As an additional test of broadband cloaking, the point source was replaced with an equivalent plane wave excitation (a vertical column of 89 coherent voltage generators at the left-hand side of the computational space). Node voltages along the second vertical column with 89 cells located three unit cells behind the cloak were recorded and a ‘blockage coefficient’ was calculated as:

$$B = |1 - T| = \left| 1 - \frac{\sum_{j=1}^{89} V_{cloak,j}^2}{\sum_{j=1}^{89} V_{0,j}^2} \right| \quad (5.30)$$

Here,  $V_{cloak,j}$  stands for node voltage with the cloaked target (total field) and  $V_0$  is node voltage without the cloaked target (incident field). The coefficient  $T$  can be thought of a ‘transmission coefficient’, but, as defined in (5.30), it can be both higher and smaller than one due to the diffraction and lensing effects. Due to this problem, the normalized coefficient  $B$  ( $0 < B < 1$ ) that clearly describes ‘blockage’ i.e. the efficiency of the cloaking was introduced.



This coefficient was calculated for a bare target, target with a passive cover (modeled as ordinary TL-based Drude metamaterial) and a target with an active cover (Figure 5-27)

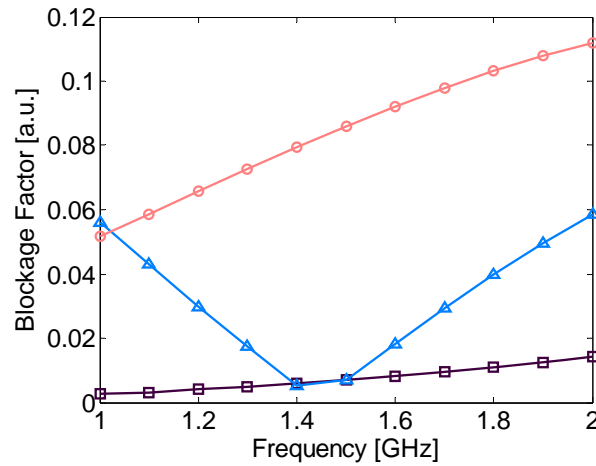


**Figure 5-27** Calculated blockage coefficient of a bare dielectric target (**circles, red**), passive cloak (**triangles, blue**) and an active cloak (**squares, magenta**)

At first, one notices that ordinary passive plasmonic cloaking (a curve with triangles) is rather narrowband (this curve is quantitatively similar to the associated curve in numerical example in [69]). However, the bandwidth of active cloaking (a curve with squares) is significantly higher (one octave). The slight increase of the blockage with frequency occurs due to change of electrical size of the cloak (this effect is also visible in a basic analysis shown in Figure 3-2). Finally, one should not forget that this cloak is an active system, so the broadband ‘inversion’ of the polarizability vector [1] is solely maintained by a power source that supplies energy to the negative capacitors.

## 5.4. EXPERIMENTAL RF (2MHz-40MHz) SUPERLUMINAL 1D ACTIVE ENZ MTM

After successful realization of active unit cells it was attempted to build a whole 1D active ENZ metamaterial (active ENZ transmission line). Unfortunately, it was found that the negative capacitors described in the previous paragraph are very sensitive to parasitic phase shifts caused by finite track lengths in the prototypes. As stressed before, both the prototype I and prototype II were ‘hand-crafted’ and it is not surprising that the effective permittivity varied slightly among the different samples. This unwanted property is not an obstacle for verification of the basic idea, but it might be a problem in a design of an active line that comprises many identical unit cells. In order to improve the repeatability, it was decided to build several negative capacitors using high-speed operational amplifiers operating in very low RF band (< 100 MHz), in which the parasitic phase shifts can be neglected.

### 5.4.1 Development and testing of OPAMP-based negative capacitors

We designed the grounded NIC circuit based on AD8099, the ultra-fast voltage feedback operational amplifier (Figure 5-28). The circuit generates a negative capacitance,



value of which can be adjusted (by varying a capacitance of  $C_1$ ) to an arbitrary value in the range -20 pF to -100pF, in the frequency band from 2 MHz to 40 MHz.

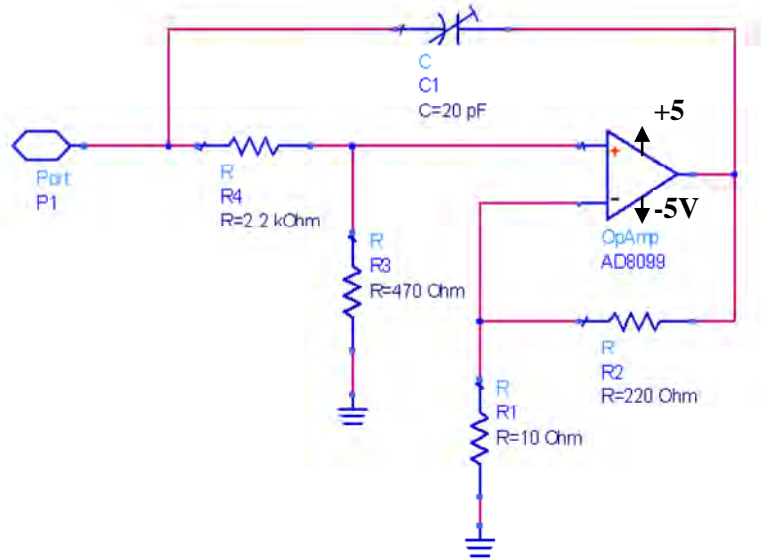


**Figure 5-28** Schematic diagram of developed OP-amp based negative capacitor

As it can be seen, this circuit is slightly modified B1 type of NIC (Figure 5-13). Additional input attenuator ( $R_4$ ,  $R_3$ ) was added to prevent the stability problems of the internal frequency compensation network of OPAMP. Actually, it was found that any amplifier based on AD8089 with closed loop gain lower than five ( $A < 5$ ) is unstable. On the other hand, the negative capacitor circuit requires  $A=2$  (assuming the conversion factor  $k=2$ ). Therefore a higher gain value that assures stable operation ( $A=23$ ) was chosen. The input signal is attenuated by the additional elements ( $R_4$ ,  $R_3$ ) and the proper operating conditions of the negative capacitor are achieved. Of course, this approach increases the noise figure, but it is not important for the demonstration of basic principles of active ENZ metamaterial.

We manufactured three negative capacitors. Each circuit was prototyped on a small (approximately  $\lambda/200 \times \lambda/200$ ,  $\lambda$  being the free-space wavelength at maximal operating frequency) printed circuit board (PCB) using standard surface mount technology (SMT) components (0603 size) (Figure 5-29).



**Figure 5-29** Photo of developed OPAMP-based negative capacitor

As in the case of BJT and FET-based negative capacitors, an additional stabilizing positive capacitor ( $C_p=68\text{pF}$ ) was used during the measurements. It was connected in parallel with port P1 of NIC assuring that the overall capacitance is positive. The input reflection coefficient of this circuit was measured using R&S ZVA 8 network analyzer and the input

impedance was calculated. After that, the influence of the stabilizing capacitor was ‘removed’ analytically. The real and the imaginary part of (de-embedded) input impedance ( $Z_{in}$ ) describe the losses (or gain) and capacitance of developed negative capacitor:

$$Z_{in} = \text{Re}\{Z_{in}\} + i \cdot \text{Im}\{Z_{in}\} = R - j \frac{1}{\omega \cdot C_N}. \quad (5.31)$$

Here,  $R$  and  $C_N$  stand for the resistance and capacitance generated by the NIC circuit while  $\omega$  is the angular frequency. The values of  $R$  and  $C_N$ , extracted from the measured reflection coefficient (with  $C_1=18\text{pF}$ ) and those obtained from ADS<sup>TM</sup> [63] circuit simulations with SPICE model of the OPAMP, are shown in Figure 5-30 and Figure 5-31, respectively.

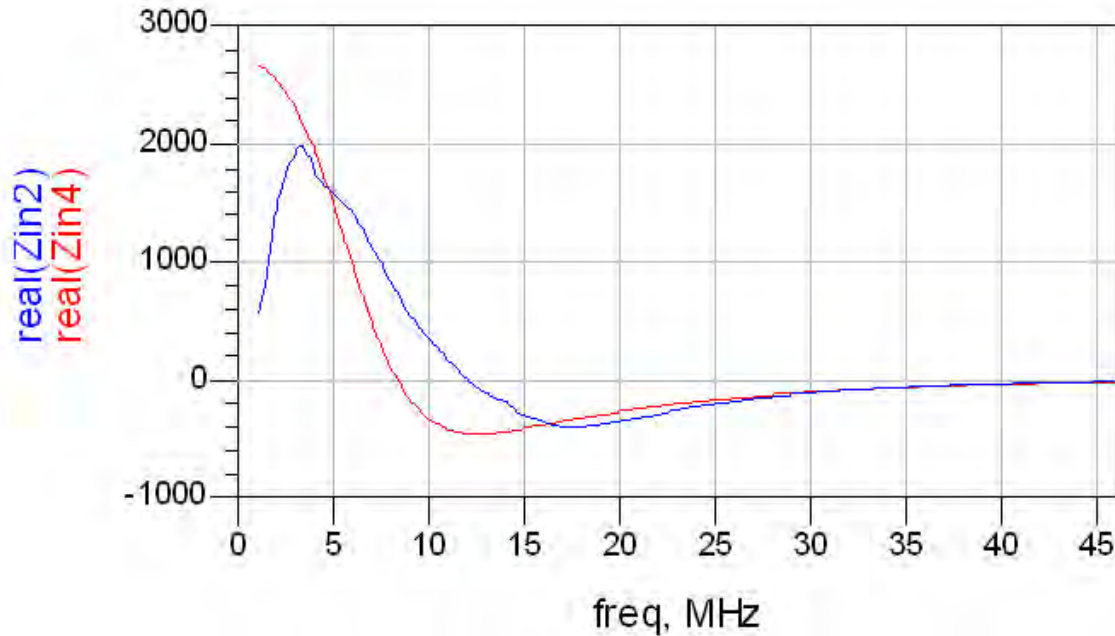


**Figure 5-30** Comparison between simulated and measured input resistance ( $\Omega$ ), **Red** – simulations, **Blue** - measurements

It can be seen (Figure 5-30) that the input resistance  $R$  is positive for the frequencies lower than 12 MHz and it is negative for the frequencies above 12MHz.

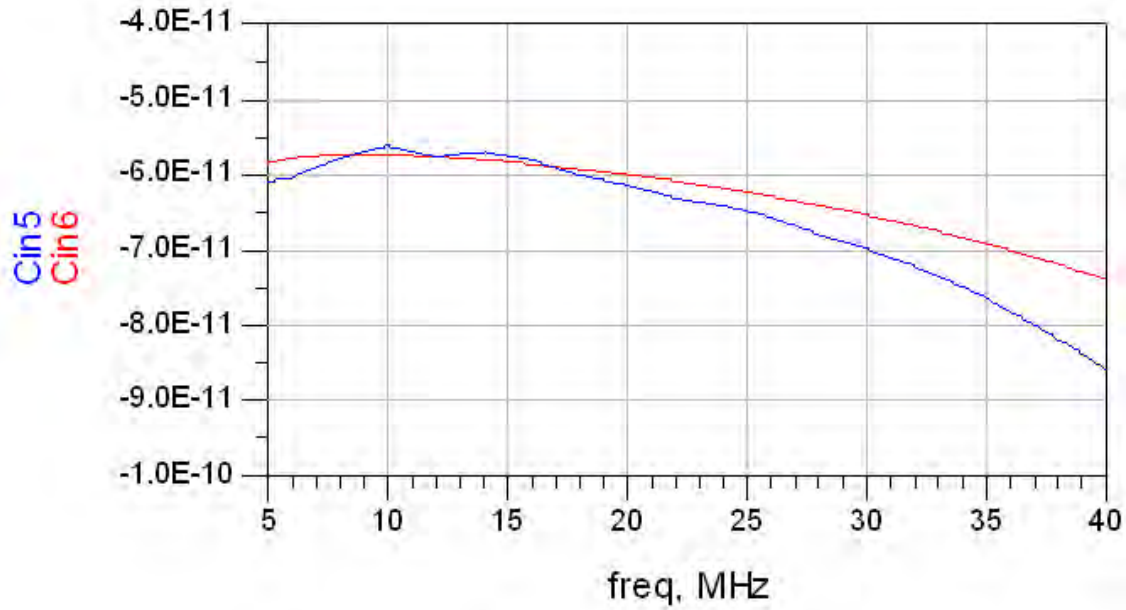


**Figure 5-31** Comparison between simulated and measured input capacitance (F) , **Red** – simulations, **Blue** - measurements

The input capacitance (Figure 5-31) varies from -60 pF to -85 pF in the frequency range 2 MHz to 40 MHz (thus, in a bandwidth of more than four octaves). This is an excellent result, which appears to be very convenient for application in active ENZ metamaterial.

Of course, both the input resistance and the input capacitance are function of the adjusted value of  $C_1$ . Thus, each NIC circuit was tuned separately (by adjusting a value of  $C_1$ ). It was found possible to adjust the capacitance in such a way that the worst-case difference between the prototypes was smaller than 2%, which is again an excellent result.

#### 5.4.2 Development and testing of ultra-broadband ENZ RF transmission line (1D MTM)

In the next step we manufactured a simple active 1D ENZ metamaterial. A simple, air transmission line was manufactured and periodically loaded with three negative capacitors (Figure 5-32). The distance  $d$  between elements was much shorter than the wavelength (approximately  $\lambda/20$  at the highest frequency,  $\lambda$  being the free-space wavelength). Thus, the theory of effective medium is valid here and the structure behaves as an 1D ENZ metamaterial. The (bare) transmission line was designed to have a characteristic impedance of  $31.5 \Omega$ , which corresponds to the distributed capacitance of 106 pF/m. These values were chosen in a way that the loading with developed negative capacitors would decrease the distributed capacitance down to 45 pF/m, corresponding to an equivalent permittivity of 0.3 and a characteristic impedance of  $50 \Omega$ .

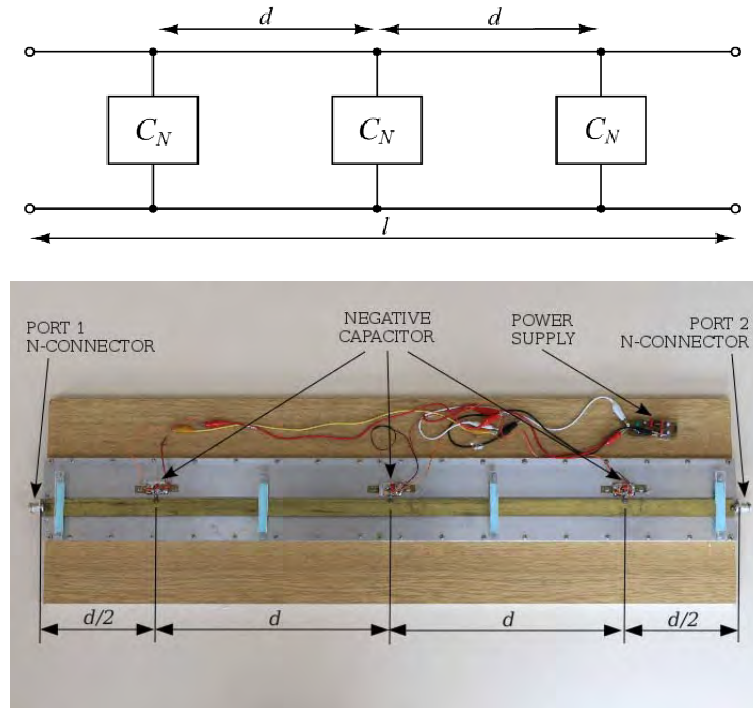


**Figure 5-32** Experimental active RF 1D ENZ metamaterial, **Upper** –A sketch of transmission line loaded with three negative capacitors the, **Lower** –practical realization ( $l=1\text{m}$ ,  $d=33\text{ cm}$ ,  $h=3\text{ mm}$ ,  $w=25\text{ mm}$ )

The 1D ENZ metamaterial was tested by the measurement of its full  $2 \times 2$  scattering matrix using the network analyzer. The measurements were done both for the bare transmission line and for the line with negative capacitors attached and powered from a DC source.

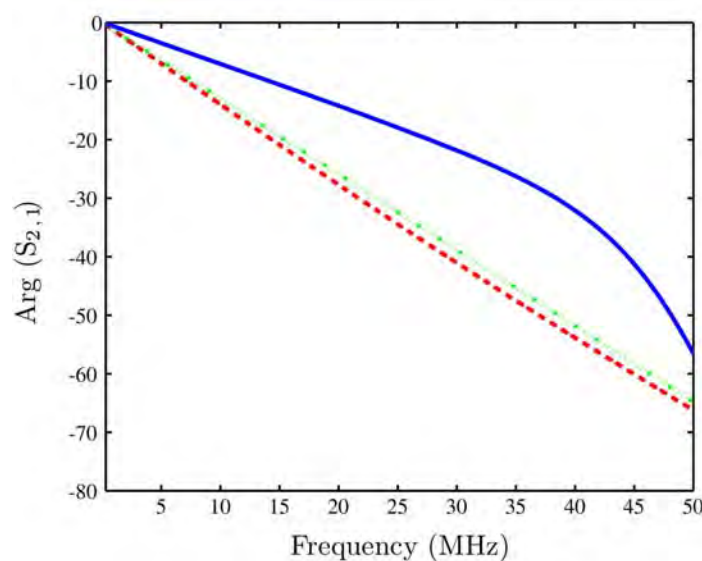


**Figure 5-33** Measured argument of transmission coefficient  $S_{2,1}$  (degrees). **Solid (blue)** – TL with NICs, **Dashed (red)** – TL without NICs, **Dotted (green)** –the light line

The measured inserted phase shift (an argument of the transmission coefficient  $S_{21}$ ) is depicted in Figure 5-33. It can be seen that the behavior of the bare transmission line is nearly identical to the behavior of the free-space (the light line), as expected. Inclusion of the negative capacitors causes the ENZ behavior with the propagation of the fast waves in a very broad frequency range (up to 40 MHz). It is important to point out that the inserted phase shift shows nearly linear (dispersionless) behavior, which is the unique property of proposed novel 1D non-Foster ENZ metamaterial.

Effective complex permittivity ( $\epsilon_r = \epsilon_r' - j\epsilon_r''$ , with  $e^{j\omega t}$  assumed time dependence) can also be extracted from measured 2x2 scattering matrix. Using the standard S-parameter description of a transmission line [17] one derives the characteristic impedance ( $Z_{0m}$ ):

$$Z_{0m} = \pm Z_c \sqrt{\frac{(1 + S_{11})^2 - S_{21}^2}{(1 - S_{11})^2 - S_{21}^2}} \quad (5.32)$$

Here,  $Z_c$  is the characteristic impedance of the measurement system (50  $\Omega$ ) and  $S_{ij}$  are measured scattering coefficients of the measured transmission line. In the first step, the scattering parameters were measured both for the bare transmission line and the active transmission line with negative capacitors. Using this data, the characteristic impedances of the bare transmission line (5.32) and the active transmission line with negative capacitors ( $Z_{0l}$ ) were calculated using (5.32). In the second step, the real and imaginary parts of the effective permittivity of the active transmission line were calculated using the following expressions:

$$\epsilon_r' = \text{Re} \left\{ \frac{Z_0^2}{Z_{0l}^2 \cdot \epsilon_{rh}} \right\}, \quad (5.33)$$

$$\epsilon_r'' = -\text{Im} \left\{ \frac{Z_0^2}{Z_{0l}^2 \cdot \epsilon_{rh}} \right\}. \quad (5.34)$$

Here,  $\epsilon_{rh}$  is permittivity of the host line (here, the host line is an air line, thus  $\epsilon_{rh} = 1$ ). Extracted complex effective permittivity is presented in Figure 5-34. The real part of the effective permittivity ( $\epsilon_r'$ ) was found to be rather constant (it varies from 0.27 to 0.37 in the frequency range of more than four octaves (2 MHz to 40 MHz)). The obtained bandwidth is considerably wider than the bandwidth of all passive ENZ metamaterials available at present, and it clearly proves the correctness of the proposed novel concept. The change of the imaginary part ( $\epsilon_r''$ ) is more pronounced (it varies from +0.8 to -0.5). At low frequencies (up to 11 MHz), the structure has losses, while in the range from 11 MHz to 40 MHz it exhibits gain.

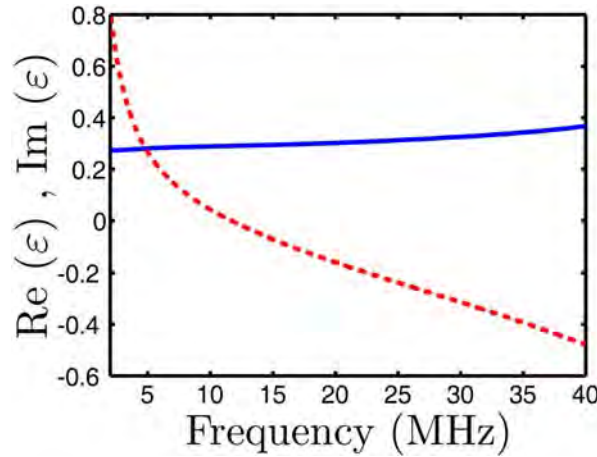


**Figure 5-34** Extracted effective permittivity of active 1D ENZ metamaterial, **Solid**–real part, **Dashed** – imaginary part

It should be stressed that the frequency dependence of the imaginary part is due to technological limitations only (it is primarily caused by the low transit frequency of the operational amplifier used) and not by underlying physical concepts. We performed detailed simulations that show that the use of a better active component (with a higher transit frequency) would decrease the value of the imaginary part of effective permittivity, and it would also have an almost dispersionless behavior similar to the real part.

#### 5.4.3 Demonstration of broadband superluminal effects

In this paragraph we investigate the phase velocity ( $v_p$ ) and the group velocity ( $v_g$ ) of active 1D ENZ metamaterial, defined by well known basic equations:

$$v_p = \frac{\omega}{\beta}, \quad v_g = \frac{\partial \omega}{\partial \beta}. \quad (5.35)$$

Here,  $\beta$  stands for phase factor ( $2\pi/\lambda$ ). Values of  $v_p$  and  $v_g$ , calculated from the measured permittivity are shown in Figure 5-35.

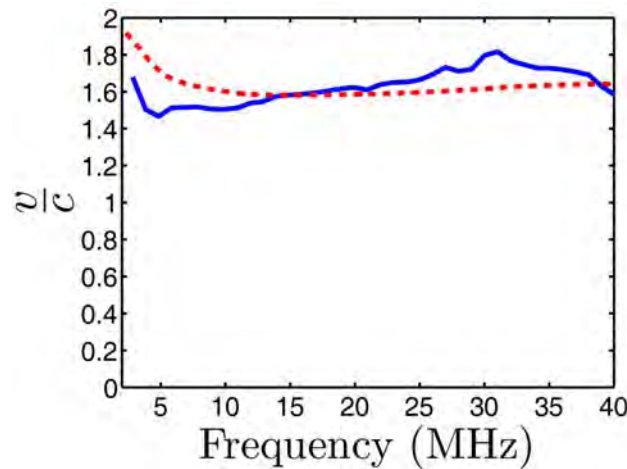


**Figure 5-35** Extracted velocities of active 1D ENZ MTM , **Dashed** - phase velocity **Solid** – group velocity

Since the equivalent permittivity is smaller than one, it is not surprising that the structure supports broadband superluminal phase velocity ( $v_p$  varies from  $1.6c$  to  $1.9c$ ,  $c$  being the speed of light; dashed line in Figure 5-35). However, it is interesting that this structure also supports counter-intuitive broadband superluminal group velocity ( $v_g$ ) from  $1.5c$  to  $1.8c$  (solid line in Figure 5-35). To the best of our knowledge, this is the first experimental demonstration of broadband superluminal group velocity. It is important to notice that the underlying physics of this superluminal propagation is different from the anomalous dispersion-based experiments widely reported in physics community [70,71,72]. The concept of anomalous dispersion is inherently narrowband and it occurs in the vicinity of the absorption (or gain) line. On the contrary, the method proposed here is based on ‘non – resonant’  $CC_N$  circuit and assures ultra-broadband superluminal behavior. Of course, this superluminal behavior is causal.

It is due to the fact that the bandwidth of any realistic negative capacitor (however broad it is) cannot be infinite. Thus, only the frequency components of the signal that lie within the operating band of the non-Foster element travel with superluminal velocity. Even if all spectral components of the signal fall within the operating band in the steady state condition, this will never be the case during the transient state. In the transient state, there is always a fraction of energy (however small it is) that lies outside the operating band and it travels with the speed of light, preserving the causality. Thus, the signal front (Brillouin’s forerunner) [70] always travels with the speed of light and the group velocity cannot be interpreted as energy velocity.

In order to verify this issue, the time-domain measurements with pulse excitation were performed. The arbitrary waveform generator was used as the source and the output signal was monitored using a high-speed digital storage oscilloscope. The screen snapshot is presented in Figure 5-36.

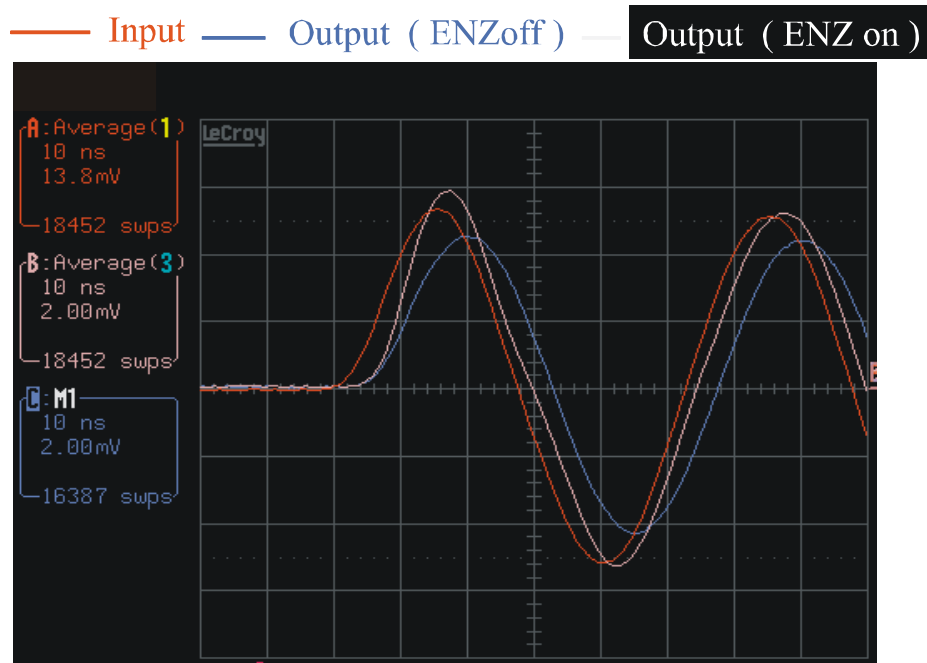


**Figure 5-36** Results of time-domain measurements of superluminal effects in active broadband 1D ENZ transmission line



The generator was adjusted to produce one period of well-behaved smooth burst signal with fundamental frequency of approximately 20 MHz (red curve in Figure 5-36). When the active ENZ line is switched off, the output signal (blue curve in Figure 5-36) arrives with the delay of about 3.4 ns. This result matches well the propagation with speed of light. When the active ENZ line is in 'on' state (magenta curve in Figure 5-36) it can be seen that the second peak at the output terminal comes 3 ns earlier than the peak in off 'state'. Thus, the superluminal behavior is clearly visible. However, it can also be seen that the leading edges both in 'off' and in 'on' states travel with  $c$ , as expected.

## 5.5. SUMMARY

Technological issues and experimental investigation of novel active broadband metamaterial based on negative non-Foster reactance have been presented in this chapter. This discussion is briefly summarized below:

- Active non-Foster elements (a negative capacitor and a negative inductor) can be achieved by NIC circuits. Due to the internal construction with positive feedback, all NIC circuits are extremely sensitive to unwanted phase shifts and parasitic capacitances and inductances. There are only a few circuits, successful realizations of which have been reported so far: Linvill- Yanagisawa design in BJT technology and Meunier-Kolev design in FET technology. The studies available in public reported maximal operating frequency of these NIC circuits of approximately 100 MHz in discrete technology and approximately 2 GHz in integrated technology.
- The OPAMP-based NICs can operate up to approximately 100 MHz, but their designs are very simple without complicated DC bias networks. In addition, the repeatability of manufactured circuits (even in the case of simple 'hand-crafting') is excellent. The only drawback is worse noise performances comparing to BJT and FET technology. Therefore, we believe that OPAMP technology is very convenient for constructing proof-of-concept demonstrators of broadband active metamaterials.
- We successfully designed, manufactured and measured several negative capacitors: the prototypes in 2MHz – 40 MHz (using OPAMP technology), the prototypes in 50 MHz – 100 MHz (using FET technology) and the prototypes in 1GHz -2 GHz range, (also using FET technology). All the prototypes showed stable operation with almost dispersionless negative capacitance. This is a significant success, particularly taking into account that all the prototypes were assembled manually.
- We successfully designed, manufactured and measured two 2D unit cells of novel ENZ metamaterial in FET technology. The measurements revealed the bandwidth of one octave (50 MHz – 100 MHz and 1GHz -2 GHz) with (almost) dispersionless ENZ behavior. Furthermore, feeding back measured results into a numerical model of plasmonic model cloak revealed that the proposed active metamaterial would enable broadband cloaking (a bandwidth of at least one octave is feasible).
- We successfully designed, manufactured and measured three-cell active ENZ transmission line (1D MTM) operating in lower RF range. Measurements revealed (almost) dispersionless behavior in the frequency range of more than four octaves (2 MHz to 40 MHz). The obtained bandwidth is considerably wider than the bandwidth of all passive ENZ metamaterials available at present, and it clearly proves the correctness of the proposed novel concept. In addition, the developed active transmission line showed counter-intuitive superluminal both phase and group velocities.



## Chapter 6 CONCLUSIONS AND FUTURE WORK

## Conclusions and future work

This study reports 12-month research effort undertaken to understand, and eventually overcome, one of the most serious drawbacks of all passive metamaterials: *the inherent narrowband operation*. We found that this narrowband operation is limited by basic physics (by the energy-dispersion constraints) and not by imperfections of available technology. However, we also found possible to go around this drawback by the incorporation of *active non-Foster elements* in the metamaterial structure.

It is known that, under some circumstances, all active elements (including the non-Foster elements) may cause stability problems. We thoroughly analyzed this issue and found that commonly used frequency-domain methods of stability prediction are not applicable in the case of non-Foster elements. Therefore, we developed a simple circuit-theory approach of accessing stability of non-Foster elements in time domain. Using developed method, we have proved that is indeed possible to build stable ENZ and MNZ metamaterials with multi-octave bandwidth and almost flat dispersion curve. This theoretical and numerical investigation has been complemented with the development of experimental proof-of-concept prototypes, in RF (up to 100 MHz) and lower microwave range (up to 2 GHz). Developed prototypes comprise: the negative capacitors, the unit cells of active 2D ENZ metamaterials, and the active ENZ transmission line. All the prototypes were ‘hand-crafted’ using standard FET and OPAMP SMD components. The measurements revealed multi-octave bandwidth, which is significantly better than the bandwidth of all passive metamaterials reported so far.

All achieved results clearly show that the novel proposed concept of non-Foster-element-based active metamaterial is correct. Finally, we have shown that this can enable ultra-broadband operation of the previously reported narrowband plasmonic and transformation-electromagnetic cloaks.

As a short summary, the realized outcomes of the project are:

- We have analyzed the basic energy-dispersion constraints in the case of passive metamaterials. We have found that these fundamental constraints inevitably lead to *resonant behavior* in all passive metamaterials *regardless* of their technological realization (SRR-based, wire-based, transmission-line-based e.t.c.). This is in contrast to the usually accepted opinion that the transmission-line metamaterials are of non-resonant nature. We have found that the operating bandwidth of the transmission-line-based metamaterials is wider than the bandwidth of volumetric inclusion-based metamaterials (e.g. SRR-based) only due to different kind of dispersion (Drude model instead of Lorentz model).
- We have proposed several novel topologies of the transmission-line-based broadband ENZ and MNZ metamaterials. They are based on 1D or 2D transmission line

periodically loaded with either shunt lumped negative capacitors (in the ENZ case) or series lumped negative inductors (in the MNZ case). Briefly, the absolute value of negative capacitance (or inductance) is chosen to be slightly lower than distributed capacitance (or distributed inductance) of the transmission line. Therefore, the net distributed capacitance (or inductance) will be positive, assuring both stable operation and almost flat dispersion curve.

- We have made a detailed investigation of stability properties of the networks that contain negative non-Foster elements. Surprisingly, we have found that commonly used frequency domain approaches for stability analysis such as Rollet stability factor completely fail here giving wrong predictions. This happens due to the fact that the negative capacitors and negative inductors always have zeroes either on the imaginary axis or in RHS of complex plane. Practically speaking, both negative capacitors and negative inductors always make use of positive feedback. Actually, we have found that the stability criteria depend not only of the negative elements but also on the topology of the remaining passive part of the network. We have developed a simple method of predicting stability for any network topology and found the design that assures stable operation of any ENZ or MNZ metamaterial. However, the stable operation does not seem to be possible in the case of ENG, MNG or DNG behavior (at least for simple one-port non-Foster networks).
- We have analyzed available designs of negative capacitors and successfully developed several prototypes using BJT, FET and OPAMP technology. Specifically, we have developed negative capacitors in 2 MHz-40 MHz RF range, in 50-100 MHz RF range and in 1-2 GHz microwave range. We have developed appropriate 1D and 2D ENZ unit cells, extracted effective permittivity and verified broadband operation. Finally, we have developed an entire three-cell 1D active ENZ metamaterial that has fractional dispersion bandwidth of 200% (more than four octaves). This is significantly better than a bandwidth of any passive metamaterial available at present. We have also found that this broadband behavior is accompanied with counter-intuitive superluminal phase and group velocities.

Finally, one might argue that all reported prototypes operate either in low RF range (up to 100 MHz) or in low microwave range (up to 2 GHz), and that the feasibility of extension of this concept into the microwave region is not clear for the time being. Our preliminary numerical study showed that using standard 180 nm CMOS technology it should be possible to increase the highest operating frequency above 5 GHz. Due to this, we believe that the future research efforts should be focused towards miniaturization of the unit cell of active ENZ or MNZ metamaterial with the help of microelectronic technology. It should be complemented with full-wave simulations of a whole system based on integration of active metamaterials with other cloaking technologies such as anisotropic, plasmonic and parallel-plate based cloaks. We believe that the proposed concepts might also find applications in antenna arrays and broadband phase shifters in communication technology.

Chapter 7 BIBLIOGRAPHY

## Bibliography

1. Smith, D., Willie J. et. al., 'A Composite Medium with Simultaneously Negative Permeability and Permittivity', *Physical Rev. Lett.*, Vol. 84 , No. 18, pp. 4184-4187, May 2000
2. Engheta, N., Ziolkowsky, R., (ed.), 'Metamaterials: Physics and Engineering Explorations', Wiley 2006
3. Eleftheriades, G. V., Balman, K.G , (ed.), 'Negative Refraction Metamaterials: Fundamental Principles and Applications', Wiley 2005
4. Caloz, C., Itoh, T., 'Electromagnetic Metamaterials: Transmission Line Theory and Microwave Applications', Wiley 2006
5. Hrabar, S., 'Application of Wire Media in Antenna Technology', a chapter in 'Metamaterials and Plasmonics, Fundamentals, Modeling, Applications', (ed. S. Souhdi, A. Sihvola, A.P. Vinogradov), NATO Science for peace and security, Springer, 2009
6. Hrabar, S., Bartolic, J., et al', 'Experimental Investigation of Subwavelength Resonator based on Backward-wave Meta-material', *Proc. on. IEEE Antenna and Propagation & URSI Symposium 2004*, pp. 2568-2571, Monterey 2004
7. Hrabar, S. Bartolic, J. et al., 'Waveguide Miniaturization Using Uniaxial Negative Permeability Metamaterial', *IEEE Tran. on Ant. Prop.*, Vol. 53, No. 1. , pp. 110-119, January 2005
8. Hrabar, S., Bartolic, J., Sipus, Z., 'Reply to "Comments on `Waveguide Miniaturization Using Uniaxial Negative Permeability Metamaterial"', *IEEE Tran. on Antennas and Propagation*, **55**, pp. 1017-1018, May 2007
9. Hrabar, S., Zaluski D., 'Subwavelength Guiding of Electromagnetic Energy in Waveguide Filled with Anisotropic Mu-Negative Metamaterial', *Electromagnetics*, Vol. 28, No. 7. pp. 494-512, October 2008
10. Pendry, J. B.. 'Negative Refraction Makes a Perfect Lens', *Physics Review Letters*, Vol. 85, pp. 3966-1 - 3966-4, 2000
11. Grbic, A., Eleftheriades, J., 'Overcoming the Diffraction Limit with a Planar left-Handed Transmission-line lens', *Physical Review Letters*, Vol. 92, No.11, pp.117403-1 – 117403-4, November 2004
12. Alu, A., Engheta, N. Achieving Transparency with Metamaterial and Plasmonic Coatings, *Physical Review E*, Volume 72, No. 1, pp. 16623-1 - 16623-3, July 2005
13. Schurig, D., Mock, J., et. al., 'Metamaterial Electromagnetic Cloak at Microwave Frequencies', *Science*, pp. 977 -980, November 2006

14. Ivsic, B., Sipus, Z., et. al. , 'Analysis of Uniaxial Multilayer Cylinders Used for Invisible Cloak Realization', IEEE Tran. on Antennas and Prop., Vol 57, No. 5, pp. 1521-1527, April 2009
15. Freire, M. J. ,Marques, R, and Jelinek, L. 'Experimental demonstration of a  $\mu = -1$  metamaterial lens for magnetic resonance imaging', Applied Physics Letters, Vo 93, pp. 231108-1 - 231108-3, December 2008
16. Landau, L.D., Lifthsitz, E.M. , Pitaevskii, L.P. , 'Electrodynamics of Continuous Media', Buttterwoth Heinmann , 2002
17. Pozar, D.M. , 'Microwave Engineering', Third Edition. J. Wiley & Sons, 2005
18. Ravel B. et al., 'Synthesis of Broadband Negative Group Delay Active Circuits,' IEEE Int. Microwave Symp. 2007, pp. 2177-2180, Honolulu 2007
19. Gharavi, S., Mojahedi, M., 'Theory and Application of Gain-Assited Periodically Loaded Transmission Lines with Negative or Superluminal Group Delays', Proc. on IEEE AP-S 2007, pp. 2373-2380, Honolulu 2007
20. Hrabar, S., Bonefacic, D., Muha, D., 'Numerical and Experimental Investigation Of Basic Properties Of Wire Medium-Based Shortened Horn Antennas ', Microwave and Optical Technology Letters, Vol. 51, No. 11, pp. 2748-2753, November 2009
21. Tretyakov, S., 'An Analytical Model of Metamaterials Based on Loaded Wire Dipoles', IEEE Tran. on Antennas and Prop., Vol 51, No. 10, pp. 2652-2658, October 2003
22. Auzanneau, F. ,Ziolkowski, R.W., 'Theoretical Study of Synthetic Bianisotropic Materials', Journal of Electromagnetic Waves and Applications, Vol 12, No 3., pp. 353-370, Jan. 1998
23. Ziolkowski, R.W., 'The Design of Maxwellian Absorbers for Numerical Boundary Conditions and for Practical Applications using Engineered Artificial Materials', IEEE Trans. Antennas Prop., Vol. 45, pp. 656-671, No 4, April 1997
24. Tretyakov S., Kharina, T., ' The Perfectly Matched Layer as a Synthetic Material With Active Inclusions', Electromagnetics, Vol 20, No.2, pp. 155-166, February 2000
25. Tretyakov, S., 'Meta-Materials With Wideband Negative Permittivity And Permeability', Microwave Opt. Technol. Lett. No 3, pp. 163-165, November 2001
26. Tretyakov S., Maslovski S, 'Veselago Materials: What is Possible and Impossible about the Dispersion of the Constitutive Parameters', IEEE Antenna and Prop. Magazine, Vol 49, No. 1, pp. 37-43, February 2007
27. Rajab, K., Yang. H., Di. B., Parini C., Vasquez, J., Philippakis, M., 'Stability of Active Magnetoinductive Metamaterials', J. Appl. Phys. Vol. 108, pp. 054904-054910, September 2010
28. Popa, B. I. and Cummer, S.A. 'An Architecture for Active Metamaterial Particles and Experimental Validation at RF,' Microwave Opt. Technology Lett. No. 49, pp. 2574-2577, October 2007
29. Hrabar, S., Krois, I., Matvijev, M., ' Is It Possible to Overcome Basic Dispersion Constraints and Achieve Broadband Cloaking?' , Proc. on. 3rd International Congress

- on Advanced Electromagnetic -Materials in Microwaves and Optics, pp. 408-410, London 2009
30. Linvill, J. G., 'Transistor Negative Impedance Converters' Proc. IRE, Vol. 41, pp. 725-729, June 1953
  31. Skahill, G., Ruish R.M. , et.al. 'Electrically Small, Efficient, Wide-Band, Low-Noise Antenna Elements', Proc. on the 1998 Antenna Applications Symposium, ( in AFRL-SN-RS-TR-1999-86 Final Technical Report), UMAS 1998, pp. 214- 213, UMAS 1998
  32. Aberle, J., Lomak, R., 'Antennas with non-Foster Matching Networks', Morgan & Claypool, 2007
  33. Sussman-Fort, S.E, 'Matching Network Design Using Non-Foster Impedances', Presentation slides, [http://www.ieee.li/pdf/viewgraphs/matching\\_network\\_design\\_non\\_foster\\_impedances.pdf](http://www.ieee.li/pdf/viewgraphs/matching_network_design_non_foster_impedances.pdf)
  34. Sussman-Fort, S.E, 'Non-Foster Impedance Matching of Electrically-Small Antennas', IEEE Trans. Antennas and Propagation, Vol. 57, No. 8, pp. 2230-2241, August 2009
  35. Sussman-Fort, S.E, 'Matching Network Design Using Non-Foster Impedances', International Journal RF and Microwave CAE, Vol 16, No. 2, pp. 135-142. March 2006
  36. Perry, A.K, 'Broadband Antenna Systems Realized from Active Circuit Conjugate Impedance Matching', Naval Postgraduate School, Monterey, September 1973
  37. Leifso, C.R, 'Design and Analysis of Novel RF Active Impedance Synthesizing Circuits', Ph.D. thesis, Department of Electrical and Computer Engineering, University of Calgary, April 2000
  38. Leifso C, Hasett, J.W, 'Active Tunable Inductor', United States Patent, Patent No: US 6,211,753 B1, April 2001
  39. Bit-Babik Di Nallo, G. C., Svigelj, J., Faraone , A., 'Small Wideband Antenna with Non-Foster Loading Elements'. Proc. on Int. Conf. on Electromagnetics in Advanced Applications, pp. 105-107, Torino 2007
  40. Sussman-Fort, S. E., Rudish, R.M., 'Non Foster Impedance Matching for Transmit Applications'. Proc.on Int. Conf. On Antenna Technology Small Antennas and Novel Metamaterials, pp. 53-56, March 2006
  41. Sussman-Fort S.E, 'Gyrator-Based Biquad Filters and Negative Impedance Converters for Microwaves', International Journal RF and Microwave CAE, pp. March 1998
  42. Hirvonen, M., Hujanen, A., Holmberg, J, Sten, J.C.E. , 'Bandwidth Limitations of Dipoles Matched with Non-Foster Impedances'. Proc. on Int. Conf. on Antennas and Propagation, pp. 1-5, EuCAP 2007, Edinburgh 2007
  43. Kaja, A. 'High Gain Rectangular Broad Band Microstrip Antenna with Embedded Negative Capacitor and Chip Resistor', PIER, Vol. 78, pp. 421–436, January 2008
  44. Song, K, Rojas, R. 'Electrically Small Wire Monopole Antenna With Non-Foster Impedance Element', Proc on EuCap 2010, pp. 1-4, Barcelona 2010
  45. Hu, Z. , Kelly, J, Song, C, Hall, P, Gardner, P., 'Novel Wide Tunable Dual-band Reconfigurable Chassis-antenna for Future Mobile Terminals', Proceedings of the Fourth European Conference on 2010, pp. 1-5, Barcelona 2010

46. Ugarte-Munoz, E, Hrabar, S, Segovia-Vargas, D., 'Investigation of Stability of Negative Impedances in Active Metamaterials and Antennas', Proc. on Eucap 2011, pp.2059-2063, Rome 2011
47. Sedra A.S, Roberts G.W, Gohh F, 'The Current Conveyor: History, Progress and New Results', IEE Proc. Vol. 137, Pt. G, No. 2, pp. 78-87, April 1990
48. Eyllier, D, 'Outils de Synthèse Originaux pour la Conception de Dispositifs Actifs Microonde Intégrés - Application au Filtrage et à l'Amplification Faible Bruit', Ph.D. thesis, Université de Limoges, May 2006
49. Jackson, R.W, 'Criteria for the Onset of Oscillation In Microwave Circuits', IEEE Transactions on Microwave Theory and Techniques, Vol. 40, No. 3, pp. 566-569, March 1992
50. -----'The FET Constant-Current Source/Limiter', Application Note AN103, Vishay Siliconix, March 1997
51. Cuthbert T.H, 'History of broadband impedance matching', IEEE Global History Network, August 2009
52. [http://www.ieeeeghn.org/wiki/index.php/History\\_of\\_Broadband\\_Impedance\\_Matching](http://www.ieeeeghn.org/wiki/index.php/History_of_Broadband_Impedance_Matching), November 2009
53. Qadir, A, 'Realization And Study of Current-Mode Filters and Oscillators for Integrated Circuit Implementation', Ph.D. thesis, NED University of Engineering and Technology, Karachi, Pakistan, 2003
54. Kolli K, 'CMOS Current Amplifiers: Speed versus Nonlinearity', Ph.D. thesis, Department of Electrical and Communications Engineering, Helsinki University of Technology, November 2000
55. Eloranta, P. 'Current Conveyors', Postgraduate Course in Electronic Circuit Design II, Helsinki University of Technology, 2004
56. Dolling, G., Enkrich C., Wegener, M., Soukoulis, C. M., Linden, S., 'Simultaneous Negative Phase and Group Velocity of Light in a Metamaterial', Science, Vol. 312 no. 5775 pp. 892-894, May 2006
57. Bonic, I., 'Design of RF Negative Capacitor based on non-Foster Circuit with Operational Amplifier', Master Thesis, University of Zagreb, 2010
58. Cristal, E.G., Podell, A., Cohn, S.B, 'Microwave Active Network Synthesis', Technical Report ECOM-0044-F, ECOM and Stanford Research Institute, February 1972
59. Kolev, S., Delacressonniere, B., Gautier, J, 'Using a Negative Capacitance to Increase the Tuning Range of a Varactor Diode in MMIC Technology', IEEE Transactions on Microwave Theory and Techniques, Vol. 49, No. 12, pp 2425-2430, December 2001
60. Park, H., Lee, S, Lee, J, Sangwook, N, 'A 0.1-1 GHz CMOS Variable Gain Amplifier Using Wideband Negative Capacitance', IECE Trans. Electron., Vol. E92-C, No.10, pp. 1311-1314, October 2009
61. Kwisung, Y., Mohammed M. et al., 'Negative Impedance Circuit and Its Application to Inductorless Resonant Oscillators', in Proc. Int. SOC Conference 2007, pp.13-16, Seoul 2007
62. Merril, J.R., 'Theory of Negative Impedance Converter', Bell System Technical Journal, pp. 88-109, January 1951



63. ----- Advance Design System , [www.home.agilent.com](http://www.home.agilent.com)
64. Bahr, A.,J., 'Active Network Techniques for Improving Antenna Performance', Technical report P-13058-EL, Stanford Research Institute, May 1977
65. Hrabar, S., 'Active Dispersionless Metamaterials – a Path towards Broadband Cloaking ', Proc. on 2009 REME Workshop , pp. 108-130, Madrid 2009
66. Hrabar, S. , Krois, I., Kirichenko, A., 'Towards Active Dispersionless ENZ Metamaterial for Cloaking Applications' , Metamaterials, Vol. 4 No. 2-3, pp. 89-97. August-September 2010
67. Hrabar, S., Krois, I., Bonic, I., Kirichenko, A., 'Experimental Investigation of Active Broadband ENZ Transmission line', Metamaterial Congress 2010, pp. 15-17, Karlsruhe 2010
68. Hrabar, S., Krois, I., Bonic, I., Kirichenko, A, 'Basic Concepts of Active Dispersionless Metamaterial based on Non-Foster Elements', Proc. on ICECOM 2010, Dubrovnik, Croatia, pp. S03P05-1-S03P05-4, 2010
69. Bilotti, F. , Tricarico, S. , Vegni, L., 'Plasmonic Metamaterial Cloaking at Optical Frequencies', IEEE Trans. on Nanotechnology' Vol. 9, No. 1, pp. 55–61, Jan. 2010
70. Withayachumnankul, W., Fischer, B.M, Ferguson, B. , Davis, B.R. , Abbott, D. , 'A Systemized View of Superluminal Wave Propagation', Proc. of IEEE, Vol 98, No. 10, pp. 1775-1786, October 2010
71. Siddiqui, O.F , Mojahedi, M., Eleftheriades, G.V,' Periodically loaded transmission line with effective negative refractive index and negative group velocity', IEEE Trans. on Antennas and Propagation, Vol. 51, No.10, pp. 2619-2615, October 2003
72. Erickson, S.J. Khaja, Mojahedi, M., 'Time- and Frequency-domain Measurements for an Active Negative Group Delay Circuit', Proc. on IEEE AP-S 2005, pp. 790-793, Washington DC, July 2005